DNA/polysome phase separation and cell width confinement couple nucleoid segregation to cell growth in *Escherichia coli*

Alexandros Papagiannakis[1,2,3], Qiwei Yu[5], Sander K. Govers[1,&], Wei-Hsiang Lin[1,2,#], Ned S. Wingreen[5,6], and Christine Jacobs-Wagner[1,2,3,4]

[1]Howard Hughes Medical Institute, Stanford University, Stanford, CA 94305, USA

[2]Sarafan Chemistry, Engineering, and Medicine for Human Health Institute, Stanford University, Stanford, CA 94305, USA

[3]Department of Biology, Stanford University, Stanford, CA 94305, USA

[4]Department of Microbiology and Immunology, School of Medicine, Stanford, CA 94305, USA

[5]Lewis-Sigler Institute for Integrative Genomics, Princeton University, Princeton NJ 08544, USA

[6]Department of Molecular Biology, Princeton University, Princeton NJ 08544, USA

[&]Current address: Department of Biology, KU Leuven, Leuven, Belgium

[#]Current address: Institute of Molecular Biology, Academia Sinica, Taipei, Taiwan

*Corresponding author: email: jacobs-wagner@stanford.edu

ABSTRACT

Chromosome segregation is essential for cellular proliferation. Unlike eukaryotes, bacteria lack cytoskeleton-based machinery to segregate their chromosomal DNA (nucleoid). The bacterial ParABS system segregates the duplicated chromosomal regions near the origin of replication. However, this function does not explain how bacterial cells partition the rest (bulk) of the chromosomal material. Furthermore, some bacteria, including *Escherichia coli*, lack a ParABS system. Yet, *E. coli* faithfully segregates nucleoids across various growth rates. Here, we provide theoretical and experimental evidence that polysome production during chromosomal gene expression helps compact, split, segregate, and position nucleoids in *E. coli* through phase separation, inherently coupling these processes to biomass growth across nutritional conditions. Halting polysome formation immediately stops sister nucleoid migration while ensuing polysome depletion gradually reverses nucleoid segregation. Redirecting gene expression away from the chromosome and toward plasmids arrests nucleoid segregation and causes ectopic polysome accumulations that drive aberrant nucleoid dynamics. Cell width perturbations show that radial confinement of polysomes and nucleoids spatially controls their phase separation to ensure that nucleoids split along the cell width and segregate along the cell length. Our findings suggest a built-in mechanism for coupling chromosome segregation to cell growth and highlight the importance of cell width regulation in nucleoid segregation.

INTRODUCTION

All cells must segregate their replicated chromosomes to propagate genetic information to daughter cells at division. Remarkably, this essential process is far less understood in bacteria than eukaryotes. Eukaryotic cells use the mitotic spindle, a sophisticated cytoskeleton-based machine. No equivalent structure has been identified in bacteria, which fold their chromosomal material into a membrane-less organelle called the nucleoid. Many bacterial species use a ParABS system to segregate a specific DNA region proximal to the chromosomal origin of replication (*oriC*) (Figge et al., 2003; Ireton et al., 1994; Jalal and Le, 2020; Lim et al., 2014; Livny et al., 2007; Mohl and Gober, 1997). However, this initial step does not explain how the rest of the replicated megabase-long chromosomes partition. Furthermore, molecular dynamics simulations suggest that the segregation of the duplicated *oriC* regions is dispensable for the segregation of the entire chromosome (Harju et al., 2024). Consistent with this idea, the chromosomally encoded *parA* and/or *parB* gene are often not essential for cell viability (Bartosik et al., 2009; Charaka and Misra, 2012; Donczew et al., 2016; Donovan et al., 2010; Du et al., 2016; Ireton et al., 1994; Jakimowicz et al., 2007a, 2007b; Jecz et al., 2015; Kadoya et al., 2011; Kawalek et al., 2020; Kim et al., 2000; Lagage et al., 2016; Lee and Grossman, 2006; Lewis et al., 2002; Li, 2019; Li et al., 2015; Minnen et al., 2011; Santi and McKinney, 2015; Takacs et al., 2022; Yamaichi et al., 2007; Yu et al., 2010). In fact, some bacteria do not even encode a ParABS system for *oriC* partitioning (Livny et al., 2007), with *Escherichia coli* being a prime example. Yet, *E. coli* segregates its duplicated nucleoids faithfully. *E. coli* mutants in which the *mukB* gene is deleted exhibit moderate nucleoid segregation defects linked to the organization and condensation of the nucleoid (Danilova et al., 2007; Mäkelä et al., 2021; Sawitzke and Austin, 2000). However, even in these mutants, most cells successfully segregate and partition their nucleoids between the daughter cells. Furthermore, topoisomerase I mutations or *seqA* deletion suppress the chromosome segregation defects associated with the *mukB* deletion (Danilova et al., 2007; Sawitzke and Austin, 2000; Weitao et al., 1999), suggesting that at least one other mechanism is at play.

Nucleoid segregation must somehow be coordinated with cell growth to accommodate the various growth rates that *E. coli* can display depending on the environmental conditions. In the presence of a poor-quality carbon source, *E coli* initiates nucleoid segregation late in the cell division cycle. As the quality of the carbon source improves and the growth rate increases, nucleoid segregation occurs at an increasingly earlier stage of the cell division cycle until it initiates in the preceding cycle to accommodate faster division times (Bates and Kleckner, 2005; Govers et al., 2024; Tiruvadi-Krishnan et al., 2022). Over the years, multiple mechanisms have been proposed to explain nucleoid segregation in *E. coli*. In 1963, Jacob et al. hypothesized that sister chromosomes migrate from mid-cell to quarter-cell positions through membrane attachment of the sister chromosomes and zonal growth of the cell envelope between the attachment points (Jacob et al., 1963). This early model was largely abandoned following the discovery that *E. coli* cells elongate via a dispersed mode of cell wall growth along the cell length up to the final stage of the division cycle (Cooper and Hsieh, 1988; Navarro et al., 2022; Wientjes and Nanninga, 1989; Woldringh et al., 1987).

Moreover, the segregation of chromosomal loci is faster than the rate of cell elongation (Kuwada et al., 2013). DNA replication has also been proposed to facilitate chromosome partitioning though a DNA polymerase-dependent extrusion mechanism (Lemon and Grossman, 2000). Simulations of coarse-grained polymer models have also suggested that the conformational entropy of confined circular nucleoid chains could provide an unmixing force that separates two mixed DNA polymers (Jun and Mulder, 2006; Jun and Wright, 2010; Pande et al., 2023). While these proposed mechanisms likely contribute to the nucleoid splitting into two objects, they cannot explain how separated sister nucleoids move away from each other. Additionally, the DNA-demixing models consider the DNA polymers in an empty cylinder, ignoring any potential effects from crowders. Furthermore, recent modeling work has argued that entropic forces generated from excluded volume interactions between partially replicated chromosomes inhibit (rather than promote) their segregation (Harju et al., 2023). This argues for the existence of one or more additional segregation mechanisms, which could involve mechanical stress between overlapping sister nucleoids (Fisher et al., 2013), DNA loop extrusion (Harju et al., 2023), or excluded volume effects between the DNA meshwork and cytoplasmic crowders (Miangolarra et al., 2021; Wu et al., 2019b). While it is likely that multiple factors contribute to nucleoid segregation and positioning inside the *E. coli* cell, the dominant mechanism underlying the diffusional bias must be tightly coupled to cellular metabolism to explain how the timing of nucleoid segregation changes with growth rate. How this is achieved remains unknown.

In contrast to eukaryotes, bacteria do not insulate their DNA in membrane-bound compartments. As a result, the chromosomal meshwork can freely interact with the macromolecules present in the cytoplasm, which exhibits a high level of polydispersity and crowding (McGuffee and Elcock, 2010; Zimmerman and Trach, 1991). Experiments and modeling have suggested that macromolecular crowders exert compaction forces on the compressible nucleoids through steric (i.e., excluded-volume) interactions (Pelletier et al., 2012; Wu et al., 2019b; Yang et al., 2020; Zhang et al., 2009). In this context, polysomes, which consist of mRNAs loaded with translating ribosomes, constitute a sizeable and abundant cytoplasmic crowder (McGuffee and Elcock, 2010). The proteome fraction allocated to ribosomes increases with growth rate across nutrient conditions (Chure and Cremer, 2023; Dai et al., 2017; Dourado and Lercher, 2020; Hu et al., 2020; Molenaar et al., 2009; Scott et al., 2014; Si et al., 2017), reaching up to 20% of the cell mass during fast growth (Chure and Cremer, 2023). The proportion of ribosomes engaged in translation also increases with improving nutrient quality, attaining 70-80% under fast growth (Dai et al., 2017; Forchhammer and Lindahl, 1971; Mohapatra and Weisshaar, 2018; Sanamrad et al., 2014; Varricchio and Monier, 1971). These polysomes form structures (Brandt et al., 2009) of comparable or larger size than the average ~50 nm mesh size of the nucleoid (Xiang et al., 2021). Consistent with a steric clash between polysomes and the nucleoid meshwork, fluorescently-labeled ribosomes accumulate in DNA-free regions such as the cell poles and between segregated nucleoids (Azam et al., 2000; Bakshi et al., 2015, 2012; Chai et al., 2014; Gray et al., 2019; Lewis et al., 2000; Mohapatra and Weisshaar, 2018; Robinow and Kellenberger, 1994; Sanamrad et al., 2014; Xiang et al., 2021).

Interestingly, theoretical work suggests that excluded-volume effects alone may be sufficient for the DNA to spontaneously phase separate from polysomes and compact into its observed nucleoid form (Mondal et al., 2011). Furthermore, a recent nonequilibrium statistical physics model proposes that nucleoid positioning and segregation could potentially be explained by considering the steric interaction (i.e., repulsion) between polysomes and DNA and the nonequilibrium effects associated with mRNA synthesis and degradation (Miangolarra et al., 2021). In this theoretical model, polysome accumulation in the middle of the nucleoid emerges due to polysomes born in the middle of the nucleoid taking longer to diffuse out of the nucleoid than those born closer to the nucleoid edges. Polysome accumulation beyond a certain concentration threshold drives phase separation between the DNA and polysomes at the mid-nucleoid location, resulting in nucleoid splitting. However, we lack experimental validation of this model. Furthermore, the coupling between nucleoid segregation and growth rate has not been addressed either experimentally or theoretically.

Here, we quantitatively characterize the temporal and spatial dynamics of nucleoids and polysomes in *E. coli* under different conditions and perturbations. In this work, we refer to nucleoid segregation as a series of events observable by microscopy (Figure 1A): (i) the initiation of nucleoid splitting, marked by the depletion of a DNA marker near the mid position of the nucleoid, (ii) the end of nucleoid splitting, which results in the generation of two separable nucleoid objects, and (iii) the migration of the sister nucleoids away from each other, marked by the increasing distance between the centroid of the nucleoids. This sequence of events can initiate in the preceding cell division cycle under nutrient-rich (fast-growth) conditions. Our experimental findings, combined with modeling, provide evidence that out-of-equilibrium and asymmetric polysome rearrangements in the cell result in both DNA compaction and the choreography of the nucleoid segregation cycle during growth across cells and nutrient conditions. The dual involvement of polysomes in protein synthesis and nucleoid dynamics ensures self-regulating coordination between cell growth and chromosome segregation across a wide range of growth rates, even under conditions where *E. coli* divides faster than it can replicate its chromosome. We also show that cell width plays a critical role in the directional patterning of nucleoid segregation by spatially regulating the phase separation between polysomes and chromosomes.

RESULTS

The rate of polysome accumulation correlates with the rate of nucleoid segregation across cells.

While the negative correlation between ribosomes and DNA has been well established from snapshot images (Azam et al., 2000; Bakshi et al., 2015, 2012; Chai et al., 2014; Gray et al., 2019; Lewis et al., 2000; Mohapatra and Weisshaar, 2018; Robinow and Kellenberger, 1994; Sanamrad et al., 2014; Xiang et al., 2021), the relative dynamics of these two macromolecules have not been quantified. To examine these dynamics with high temporal resolution (every 1 or 3 min, Figure 1 – figure supplement 1A-E), we ran time-

148 lapse microfluidic experiments using an *E. coli* strain carrying the 50S ribosomal protein RplA fused to GFP
149 and the nucleoid-associated protein HupA tagged with mCherry (Xiang et al., 2021). Cells were grown at
150 30˚C in M9 buffer supplemented with glucose, casamino acids and thiamine (M9gluCAAT). While the
151 ribosome signal displayed the expected polar and inter-nucleoid enrichments, the accrual of ribosome
152 signal in the middle of the cells was particularly strong compared to the polar regions, as shown by
153 representative individual cells (Figure 1B and Movie S1) and average kymographs (Figure 1C, n = 4122
154 cell division cycles). Cell constriction contributed to the apparent depletion of ribosomal signal from the mid-
155 cell region at the end of the cell division cycle (Figure 1B-C and Movie S1). In predivisional cells, the
156 ribosomal signal accumulated in the middle of the segregated nucleoids near the ¼ and ¾ cell positions,
157 as shown in average one-dimensional (1D) and two-dimensional (2D) fluorescence profiles (n = 1907
158 predivisional cells, Figure 1D). As expected (Bakshi et al., 2012; Sanamrad et al., 2014), the RplA-GFP
159 signal became homogeneous within cells following their treatment with rifampicin (Figure 1 – figure
160 supplement 1F), a transcription inhibitor that causes polysome depletion over time (Blundell and Wild, 1971;
161 Campbell et al., 2001; Hartmann et al., 1967). This indicates that all ribosomal enrichments consist of
162 polysomes and therefore will be referred to as polysome accumulations hereafter.
163
164 Under our relatively nutrient-rich growth conditions (M9gluCAAT), nucleoid splitting occurred early in the
165 division cycle and even sometimes initiated in the segregated nucleoids from the preceding division cycle
166 (Movie S1 and Figure 1B). Given the variability in nucleoid segregation timing across cells (Figure 1 – figure
167 supplement 2A), we developed a computational method to track nucleoid dynamics independently of the
168 cell division cycle (see Methods and Figure 1 – figure supplement 2B-C). Specifically, we focused on the
169 nucleoid cycle—defined as the period between the ends of two nucleoid splitting events (Figure 1 – figure
170 supplement 2D)—instead of the division cycle. By tracking the accumulation of RplA-GFP and the depletion
171 of HupA-mCherry in the middle of nucleoids, we found that polysome accumulation and nucleoid splitting
172 correlated in time (Figure 1E). Furthermore, the rate of polysome accumulation at mid-nucleoid ($\Delta RplA_{mid-}$
173 $_{nuc}/\Delta T$) correlated with the rate of DNA depletion in the same region ($\Delta HupA_{mid-cell}/\Delta T$) at the single-cell level
174 (Figure 1F). This indicates that cells that accumulated polysomes faster also split their nucleoids faster.
175 Importantly, the fitted linear regression had an intercept close to zero for both axes (Figure 1F), indicating
176 that when the rate of polysome accumulation approached zero, so did the rate of nucleoid splitting.
177
178 To examine what happens when sister nucleoids move away from each other, we divided the time between
179 the end of nucleoid splitting and cell division into four bins. We found that right after nucleoid splitting (0-
180 25% bin), most (~70%) cells continued to accumulate polysomes at mid-cell, i.e., between the sister
181 nucleoids (Figure 1G). For these cells, the rate of polysome accumulation ($\Delta RplA_{mid-cell}/\Delta T$) positively
182 correlated with the rate of nucleoid migration ($\Delta Distance_{nuc}/\Delta T$) (Figure 1H). Thus, the faster that cells
183 accumulated polysomes at mid-cell, the faster the sister nucleoids migrated apart (and vice versa).
184

185

186 ***Cell elongation may also contribute to sister nucleoid migration near the end of the division cycle.***
187 We noted that there was a substantial percentage (~30%) of cells with decreasing RplA-GFP signal at mid-
188 cell right after nucleoid splitting ($\Delta RplA_{mid\text{-}cell}/\Delta T \leq 0$, Figure 1H). Interestingly, in these cells, nucleoid
189 migration did not stop; instead, its average rate was similar to the average rate of cell elongation
190 ($\Delta Length_{cell}/\Delta T$) (Figure 1H). In fact, when the cell elongation rate was subtracted from the nucleoid
191 migration rate for each single cell (Figure 1- figure supplement 3A), the positive correlation between
192 polysome accumulation and nucleoid migration rates remained, but now the average rate of nucleoid
193 migration was near zero in cells with no polysome accumulation ($\Delta RplA_{mid\text{-}cell}/\Delta T \leq 0$). This finding may
194 suggest a mixed contribution between polysome accumulation and cell elongation to nucleoid migration.
195 This was interesting considering that polysomes became less enriched at mid-cell but more enriched in the
196 middle of sister nucleoids in predivisional cells (Figure 1B-D), with the average ribosome concentration
197 remaining constant during the cell division cycle (Figure 1 – figure supplement 1E). The spatial change in
198 polysome enrichments was accompanied with a steady decline in the percentage of cells that continued to
199 accumulate polysomes at mid-cell between the end of nucleoid splitting and cell division (Figure 1G).
200 Concurrent with this decline, the migration rate of sister nucleoids became less correlated with the rate of
201 polysome accumulation and more correlated with the rate of cell elongation (Figure 1 – figure supplement
202 3B). To examine the relative correlation of polysome accumulation and cell elongation with nucleoid
203 migration over time, we used a linear mixed-effects model to analyze each relative nucleoid migration
204 interval (see Methods). The coefficients of the fitted mixed linear regressions suggest the following
205 hypothesis: Early during nucleoid migration (0-25% between the completion of nucleoid splitting and cell
206 division), polysome accumulation contributes most to the measured variance in the displacement of the
207 sister nucleoids (Figure 1I). This contribution progressively decreases over time while that of cell elongation
208 increases (Figure 1I). Such a switch in relative contribution would be consistent with the spatiotemporal
209 dynamics of polysome accumulation and cell wall synthesis, as described in the Discussion.
210

211 ***Polysome accumulation at mid-cell correlates with the relative timing of nucleoid segregation***
212 ***across nutrient conditions and growth rates.***
213 If polysome production plays a role in nucleoid segregation, it predicts that the timing and amount of
214 polysome accumulation at mid-cell will correlate with the timing of nucleoid segregation across nutrient
215 conditions. To test this prediction, we analyzed images of fluorescently labeled ribosomes and nucleoids in
216 cells grown under 30 different carbon source conditions (Table S1) that vary the doubling times (~40 min
217 to ~4 h) and average cell areas (~1.9 to ~3 μm^2) of *E. coli*. This dataset included both previously published
218 (Gray et al., 2019) and new microscopy snapshots from our laboratory. Demographs generated from these
219 images revealed that the polysome accumulation at mid-cell was reproducible across all conditions and
220 strains, irrespective of the ribosomal subunit protein (RplA or RpsB) or the fluorescent tag (msfGFP, mEos2
221 or GFP) used to mark ribosomes (Figure 2A and Figure 2 – figure supplement 1). In these experiments,

222 nucleoids were typically imaged using DAPI (rather than a fluorescent fusion to HupA), indicating that
223 polysome accumulation at mid-nucleoid was independent of the DNA labeling method. Importantly, and
224 consistent with our prediction, the richer the growth conditions (i.e., the larger the average cell area), the
225 earlier the polysome accumulation and the nucleoid splitting occurred in the division cycle based on relative
226 cell lengths (Figure 2A and Figure 2 – figure supplement 1). In addition, the polysome accumulation at mid-
227 cell was more pronounced in nutrient-rich media (e.g., M9malaCAAT) compared to nutrient-poor ones (e.g.,
228 M9mann) where the nucleoid segregated later in the division cycle (Figure 2A and Figure 2 – figure
229 supplement 1).
230
231 To quantify these phenotypes across strains and nutrient conditions, we extracted and correlated
232 population-level polysome and nucleoid statistics. We found a strong correlation (Spearman correlation ρ
233 = -0.85) between the amplitude of the average ribosomal signal accumulation and the average nucleoid
234 signal depletion at mid-cell (Figure 2B). Since the average cell area (colormap in Figure 2B) correlated with
235 the growth rate of the population (Schaechter et al., 1958), this plot also confirmed that faster growing
236 populations displayed stronger polysome accumulation and greater DNA depletion at mid-cell on average
237 (Figure 2B).
238
239 We wondered whether the correlation between polysome and nucleoid dynamics could also be seen across
240 cells growing in the exact same nutritional condition but at different growth rates due to cell-to-cell variability.
241 To examine this possibility, we divided our timelapse microfluidics data into growth rate bins (Figure 2C)
242 and compared their temporal polysome and nucleoid patterns. We found that, compared to the slowest
243 growing subpopulation (bin 1 with a mean growth rate = 0.28 h^{-1}), the fastest growing subpopulation (bin
244 13 with = 0.74 h^{-1}) displayed a more pronounced and earlier accumulation of polysomes that was associated
245 with earlier nucleoid segregation (Figure 2D). The subpopulation with an intermediate growth rate (bin 7
246 with = 0.51 h^{-1}) also displayed an intermediate pattern of polysome accumulation and nucleoid segregation.
247 In fact, when we calculated the average polysome accumulation and nucleoid depletion at mid-cell for each
248 growth rate bin, we found that the two statistics correlated (Figure 2E). Faster growing cells accumulated
249 more polysomes at mid-cell and split their nucleoids earlier during the cell division cycle compared to slower
250 growing cells.
251
252 Both the average proteome fraction dedicated to ribosomes and the average fraction of ribosomes engaged
253 in translation are known to correlate with growth rate across nutrient conditions (Chure and Cremer, 2023;
254 Dai et al., 2017; Dourado and Lercher, 2020; Hu et al., 2020; Molenaar et al., 2009; Scott et al., 2014; Si et
255 al., 2017). Thus, a role for polysome production in nucleoid segregation may provide a mechanistic link
256 between growth rate and the relative timing of nucleoid splitting both across cells in a given nutrient
257 condition as well as across populations in different nutrient conditions.
258

Spatial polysome asymmetry correlates with nucleoid positioning.

A surprising result was the apparent higher polysome accumulation at mid-cell relative to the cell pole regions (Figures 1B-C and 2A), which was not artificially created by the smaller cytoplasmic volumes at the cell poles or constriction sites due to membrane curvature (Figure 2 – figure supplement 2). This uneven distribution of polysomes suggested limited diffusion-driven equilibration of polysome concentration between the DNA-free regions. At division, such a disequilibrium could lead to a higher concentration of polysomes at the new cell pole relative to the old pole in daughter cells through inheritance. To examine this possibility, we turned back to the microfluidic experiments in which we traced cell lineages from mother to daughter cells (Figure 1 – figure supplement 1A), determined the pole identity (new vs. old) of each tracked cell (Figure 1 – figure supplement 2B), and compared the polysome accumulations between the new and old poles (see Methods and Figure 3 – figure supplement 1A-D). Old mother cells (located at the end of the microfluidic channels) and their daughters were excluded from our analysis to avoid cell aging effects (Chao et al., 2023; Coquel et al., 2013; Koleva and Hellweger, 2015; Łapińska et al., 2019; Lindner et al., 2008; Proenca et al., 2019). Consistent with the absence of rapid equilibration of polysome concentration between DNA-free regions through diffusion, we found that newborn cells had more polysomes at the new pole compared to the old one on average (Figure 3A).

Across cells, the polysome distribution asymmetry between cell poles negatively correlated with the position of the nucleoid in newborn daughter cells (Figure 3B, cells always oriented with the new pole to the right). The *x* and *y* intercepts of a fitted linear regression to the data were not zero, indicating that a nucleoid positioned precisely at the cell center did not equate with an even distribution of polysomes between poles. Instead, newborn cells with centrally located nucleoids tended to have more polysomes at the new pole compared to the old pole (example #1 in Figure 3B-C) whereas cells born with symmetric polysome enrichments between poles tended to display an off-center nucleoid closer to the new pole (example #2 in Figure 3B-C).

Spatial polysome asymmetry correlates with asymmetric nucleoid compaction in newborn cells.

Construction of average 2D cell projections of the RplA-GFP signal in cells sorted based on their relative timing to cell division confirmed the polysome asymmetry between poles in newborn cells (Figure 3D and Movie S2). Strikingly, the corresponding 2D projections of the HupA-mCherry signal revealed another spatial asymmetry, this time, in the average DNA mass distribution along the nucleoid length (axial asymmetry). The average HupA-mCherry signal concentration was higher toward the new pole right after birth or, correspondingly, toward the middle of the cell (future new pole) in the period prior to division (Figure 3D and Movie S2). Quantification of this axial asymmetry in newborn cells revealed that the HupA-mCherry concentration is ~20% higher toward the new pole on average (Figure 3E), suggesting that the DNA density is uneven along the nucleoid length. This nucleoid mass asymmetry emerged late in the nucleoid migration cycle, typically before cell division such that it was inherited by newborn cells (Figure 3D).

To examine if features of polysome accumulations (e.g., position, amplitude, or fraction of cell length covered) correlate with the asymmetric nucleoid density and its variability among cells, we used a linear mixed-effects model (see Methods). We found that in newborn cells, the positions of polysome enrichments in the old-pole and mid-cell regions significantly correlated with the HupA-mCherry density asymmetry (Figure 3 – figure supplement 1E-G). Guided by this finding, we hypothesized that the positions of the accumulating polysomes along the cell length determine the space available for the chromosome to occupy, and thereby dictate the DNA density distribution along the nucleoid. To examine this hypothesis, we combined the correlated polysome accumulation characteristics into a compound statistic that describes the relative polysome-free space between two cell halves (see Methods). Compared to other polysome statistics, the relative availability of cell space depleted of polysomes (RplA-GFP signal) correlated most strongly with the asymmetric distribution of DNA (HupA-mCherry signal) in newborn cells (Figure 3F). In other words, the DNA concentration was higher in cell regions with more space available between polysome enrichments. In most (~60%) cells, the distance between polysome enrichments, and thus the DNA concentration along the nucleoid, was greater between mid-cell and the new pole (i.e., x and y values >1, example #1 in Figure 3F-G). The opposite pattern was true for a small fraction (~14%) of cells, where the larger distance between polysome enrichments was located between mid-cell and the old pole (x and y values < 1, example #2 in Figure 3F-G). The correlated variability in polysome and nucleoid patterning across cells suggests that the size of the polysome-depleted spaces helps determine where the chromosomal DNA is most concentrated along the cell length. This patterning is likely reinforced through the displacement of the polysomes away from the DNA dense region.

A minimal reaction-diffusion model generates experimentally observed cellular asymmetries and growth rate-dependent nucleoid segregation.

Our single-cell studies provided experimental support that phase separation between polysomes and DNA contributes to nucleoid segregation. However, it remained unclear whether the same mechanism could also explain the growth rate-dependent trends and cellular asymmetries that we observed (Figures 2 and 3). Therefore, we built a minimal reaction-diffusion model (see Methods) to describe the dynamics of polysomes and DNA during the cell cycle based on previous findings (Miangolarra et al., 2021). The model takes into account two ingredients important for nucleoid segregation: steric effects (repulsion) between DNA and polysomes (described by Cahn-Hilliard theory) and the nonequilibrium processes of polysome synthesis and degradation (described by linear reaction kinetics). The model is based on realistic parameters of polysome diffusion, production, and degradation (see Methods). We assume polysome production (i.e., transcription) to be uniform within the nucleoid and polysome degradation (i.e., mRNA decay) to be uniform across the entire cell (from pole to pole). These assumptions consider the most trivial cases (see Discussion for other cases). We also assume that the cell grows exponentially and that the nucleoid expands in size proportionally to the cell during growth, which has been experimentally verified

333 (Campos et al., 2014; Govers et al., 2024). Since *E. coli* grows along its long axis and polysomes do not
334 readily go around the nucleoid to equilibrate (Figure 3A-D and Figure 2 – figure supplement 2), we reduced
335 the problem to one dimension, the cell length. Importantly, the system is driven out of equilibrium by the
336 continuous production and degradation of polysomes. It operates at a nonequilibrium steady state even at
337 fixed cell length.
338
339 Initialized from the steady state of a single compacted nucleoid in the middle of the cell with symmetric
340 polysome distributions at the poles, our model shows that polysomes accumulate in the middle of the
341 nucleoid during growth (Figure 4A and Movie S3, left panel). This is followed by division of the nucleoid into
342 two entities, which then move apart from each other as polysomes accumulated between them. The model
343 provides a minimal mechanism for nucleoid segregation: At any given point, polysomes that form in the
344 middle of the nucleoid have a lower probability of escaping the nucleoid through diffusion compared to
345 polysomes born at the edge of the nucleoid (Figure 4B). Thus, the polysome concentration rises
346 monotonically towards the center of the nucleoid, its peak increasing with nucleoid length (quadratically in
347 the quasi-steady-state limit). Nucleoid elongation during cell growth promotes polysome accumulation in
348 the middle of the nucleoid. Phase separation driven by the steric repulsion between DNA and polysomes
349 results in the nucleoid splits in two (Figure 4A and Movie S3, left panel).
350
351 We wondered if this simple reaction-diffusion mechanism could also explain the correlation between growth
352 rate and the relative timing of nucleoid segregation. Therefore, we performed simulations for different
353 growth rates, matching the cell and nucleoid length at birth with population-level measurements (Figure 4
354 – figure supplement 1A). To initialize each simulation in a realistic fashion, we used the last time point (i.e.,
355 half of the predivisional cell) of the previous simulation as initial conditions, capturing the new/old pole
356 identity as well as any cellular asymmetries inherited between generations. The relative timing of nucleoid
357 splitting was measured as nucleoid depletion at mid-cell beyond a threshold of 0.1 arbitrary units (Figure
358 4A and Figure 4 – figure supplement 1B). We found that our model successfully captures the negative trend
359 between the growth rate and the relative timing of nucleoid splitting. Simulated cells that grew faster also
360 split their nucleoids earlier from birth to division (Figure 4C and Movie S3), in agreement with population-
361 level data (Figure 2 – figure supplement 1).
362
363 To examine a potential origin for the asymmetries in polysome distribution and nucleoid compaction that
364 we observed (Figure 3), we examined the effect of the nucleoid diffusion coefficient D_{n}, which is a model
365 parameter describing how fast the nucleoid relaxes towards its equilibrium configuration. Large D_{n}
366 represents the quasi-steady-state limit where the nucleoid relaxation time scale is much shorter than the
367 cell doubling time, and the nucleoid always assumes its (symmetric) equilibrium state. Conversely, small
368 D_{n} (i.e., slower relaxation time) can lead to asymmetric concentration profiles that will be inherited by the
369 daughter cells. Consistent with this expectation, we found that during relatively fast growth (~40 min

370 doubling time), a lower nucleoid diffusion coefficient results in a larger deviation from the equilibrium
371 concentration profiles for the nucleoid and polysomes (dotted curves vs. solid curves, Figure 4D). In fact,
372 at diffusion coefficients below 0.001 $\mu m^2/s$, the model (Figure 4D) reproduced the experimentally observed
373 asymmetries, including the nucleoid position offset towards the new pole at birth, the higher polysome
374 concentration at the new pole compared to the old one, and the asymmetric nucleoid compaction (Figure
375 3). Our minimal model thus suggests that the material properties of the nucleoid (e.g., stiffness) may
376 contribute to the observed nucleoid and polysome asymmetries in *E. coli* (see Discussion).
377
378 ***Polysomes accumulate at mid-nucleoid in DNA regions inaccessible to freely diffusing particles of***
379 ***similar sizes.***
380 In the model, the early polysome accumulation in the middle of nucleoid is caused by the nonequilibrium
381 processes of polysomes being born within the nucleoid while being degraded uniformly across the cell (due
382 to mRNA turnover). It predicts that the early mid-nucleoid enrichment of polysome signal observed in our
383 experiments is the product of such nonequilibrium processes rather than of polysomes simply diffusing into
384 undetected DNA-free space. If this is correct, freely diffusing objects of similar sizes to polysomes should
385 accumulate at mid-cell after polysomes accumulate there, i.e., after free DNA-space has been generated
386 through nucleoid splitting. To test this expectation, we compared the average distribution of RplA-msfGFP
387 with that of freely diffusing mCherry-labeled μNS particles from snapshot images of DAPI-stained cells
388 (Figure 4E). These μNS particles consist of a fragment of a mammalian reovirus protein (Broering et al.,
389 2005, 2002) that self-assembles into a particle, typically one per cell, when produced orthogonally in *E. coli*
390 (Parry et al., 2014). They have sizes between 50 and 200 nm (Parry et al., 2014; Xiang et al., 2021) similar
391 to polysomes (Brandt et al., 2009; Slayter et al., 1968) and are therefore largely excluded by the nucleoid
392 mesh (Xiang et al., 2021). After sorting cells by length into four bins, the positions of mCherry-labeled μNS
393 particles from approximately 2580 cells per bin were superimposed using the relative cellular coordinates
394 to construct particle density maps. Cells were randomly oriented in this analysis (meaning that asymmetries
395 between poles cannot be observed), as the pole identity cannot be assigned from snapshot images.
396
397 We found that in the shortest (i.e., newborn) cells, RplA-msfGFP-labeled polysomes had already
398 accumulated within the nucleoid (Figure 4F, bin 1). In contrast, mCherry-μNS particles were restricted to
399 the cell poles and were not able to access the mid-cell region until after nucleoid splitting was clearly visible
400 (Figure 4F, bins 2-4). This was also shown in the corresponding 1D average concentration and particle
401 density profiles (Figure 4G). These observations support the notion that the early mid-nucleoid
402 accumulation of RplA-msfGFP is caused by nonequilibrium effects associated with polysome synthesis and
403 degradation rather than polysome diffusion into DNA-free space.
404
405

406 ***Arrest of polysome production immediately stops nucleoid segregation while polysome depletion***
407 ***gradually reverses it.***
408 Our correlative analyses and model (Figures 1-4) support the hypothesis that the interactions and ensuing
409 phase separation between polysomes and nucleoid promote nucleoid segregation and macromolecular
410 asymmetries along the cell length. To probe causality, we first aimed to disrupt the proposed mechanism
411 using rifampicin. Rifampicin treatment is known to homogenize ribosome distribution and expand the
412 nucleoid over time through polysome depletion (Bakshi et al., 2014; Dworsky and Schaechter, 1973; Koch
413 and Gross, 1979; Pettijohn and Hecht, 1974; Xiang et al., 2021). However, our hypothesis predicts a faster
414 effect on nucleoid segregation. Blocking transcription should instantly reduce the rate of polysome
415 production to zero, causing an immediate arrest of nucleoid segregation. Then, gradual depletion of the
416 existing polysomes due to mRNA decay should cause, on a slower time scale, a dissipation of the phase
417 separation.
418
419 To test these predictions, we subjected cells growing in M9gluCAAT in microfluidic channels to two rounds
420 of rifampicin treatment (Figure 5A and Movie S4). Rifampicin resulted in growth rate inhibition (Figure 5A)
421 and changes in the nucleoid area and nucleoid-to-cell area (NC) ratio (Figure 5 – figure supplement 1), as
422 previously described (Bakshi et al., 2014; Dworsky and Schaechter, 1973; Koch and Gross, 1979; Pettijohn
423 and Hecht, 1974; Xiang et al., 2021). In cells that completed their division cycle before antibiotic addition
424 (squares and fitted blue curve in Figure 5B), the distance between the intensity peak of each sister nucleoid
425 increased monotonically between birth and division, displaying the dynamics of normal, unperturbed
426 nucleoid segregation. Cells born 22 min to 12 min before the treatment (circles in Figure 5B) experienced
427 the same nucleoid segregation dynamics up to the time of rifampicin addition. Exposure to rifampicin lead
428 to the near-immediate arrest of nucleoid segregation (Figure 5B), consistent with our prediction.
429
430 Interestingly, the distance between the sister nucleoids remained the same for close to 30 min into
431 rifampicin treatment, after which it started to decrease (Figure 5B). Average 1D and 2D cell projections of
432 the scaled (divided by the whole cell average) RplA-GFP and HupA-mCherry concentration suggest that
433 the time delay between the arrest in nucleoid segregation and its reversal is likely due to the compressible
434 nature of the nucleoid, which has been demonstrated in vitro (Pelletier et al., 2012). As the polysomes in
435 the middle of the cells started to visibly deplete (> 6 min after rifampicin addition), the DNA signal expanded
436 to fill the emerging available space without affecting the distance between the peaks of the sister nucleoids
437 (white crosses, Figure 5C). This is consistent with the removal of a compaction force exerted by the
438 accumulating polysomes on the soft nucleoid. About 30 min after rifampicin addition and further polysome
439 depletion, the peak signals of the sister nucleoids (white crosses, Figure 5C) started migrating closer to
440 each other. Eventually, after 1 h of rifampicin treatment, when the RplA-GFP fluorescence was
441 homogeneous and there were no polysome accumulations detected, the two nucleoid objects fused into
442 one (Figure 5C), consistent with the dissipation of phase separation.

These results support the notion that in untreated cells, polysome accumulation effectively exerts a force on the compressible nucleoid, which translates into its observed compaction and translocation (hence, segregation). Gradual polysome depletion through rifampicin treatment progressively decreased this effect, reversing the process. This reversal became obvious when we plotted the correlation between the relative polysome accumulation and nucleoid depletion at mid-cell for two cell lineages that experienced rifampicin at different times after birth (Figure 5D). Irrespective of their birth time (12 or 3 min before the addition of rifampicin), the negative correlation between the two variables was reversed ~9 min after the addition of the antibiotic, following the same path as for the untreated cells but in the opposite direction (Figure 5D). Polysome depletion during rifampicin treatment also resulted in correlated loss of asymmetric nucleoid compaction in newborn cells (Figure 5E). Altogether, these results support the notion that the asymmetric accumulation of polysomes results in an anisotropic force that asymmetrically compacts and segregates nucleoids.

Ectopic polysome production redirects nucleoid dynamics.

Our second approach to test causality experimentally was to redirect polysome formation away from the chromosome by over-expressing a useless protein (mTagBFP2) for the cell from a T7 promoter on a multi-copy pET28 plasmid (Figure 6A). The resulting CJW7798 strain also carried the ribosome (RplA-msfGFP) and DNA (HupA-mCherry) markers. We reasoned that high expression of BFP2 from the plasmid may slow polysome production within the nucleoid and create polysome accumulations at ectopic cellular locations through recruitment of ribosomes to plasmid transcripts. This, in turn, should affect nucleoid dynamics if our proposed mechanism is correct.

Plasmid expression of mTagBFP2 was induced by addition of 100 μM IPTG and expression of a chromosomally encoded T7 RNA polymerase (Figure 6A-B). The gradual increase of mTagBFP2 fluorescence in the cells was associated with a concomitant decrease in cell growth rate (Figure 6C), consistent with reduced gene expression from the chromosome. These cells displayed various patterns of polysome accumulations (Movie S5), presumably due to stochastic clustering of plasmids in DNA-free regions as previously reported for other multi-copy plasmids devoid of DNA partitioning genes (Hsu and Chang, 2019; Reyes-Lamothe et al., 2014; Yao et al., 2007). Importantly, the ectopic accumulations of polysomes had a drastic effect on nucleoid dynamics. In some cells, polysomes accumulated at one pole instead of the middle of the nucleoid, preventing the nucleoid from splitting (Figure 6D). Expansion of the polysome accumulation at a pole effectively pushed the nucleoid toward the opposite pole of the cell. In other cells, polysome accumulation occurred between sister nucleoids, but did not relocate to the segregated nucleoids at the ¼ and ¾ cell positions. Rather, polysome accumulation persisted and expanded between the sister nucleoids, effectively further pushing them apart (Figure 6E). Often, cells filamented and showcased correlated polysome and nucleoid dynamics that changed in time (Figure 6F),

480 resulting in transient events of nucleoid fusion, splitting, or changes in migration direction depending on
481 where polysomes accumulated. Movie S5 shows additional examples of such dependency.
482
483 All cells displayed diffuse mTagBFP2 fluorescence (Figure 6B). We also observed the formation of inclusion
484 bodies (bright phase contrast) that typically remained at a pole or sometimes moved along the edge of a
485 growing polysome accumulation (Figure 6F). After a long of period of IPTG induction (> 8 h), polysome
486 accumulation eventually decreased, leading to nucleoid decompaction (Figure 6 – figure supplement 1).
487 Altogether, these results support the notion that ectopic polysome accumulation drives nucleoid dynamics.
488
489 ***Radial confinement prevents nucleoid splitting along the cell width and fusion of polysome***
490 ***accumulations from distinct DNA-free regions.***
491 In the model (Figure 4), phase separation between polysomes and nucleoid occurs when the cell and
492 nucleoid elongate. As *E. coli* cells grow by increasing their length and not their width, we reasoned that
493 radial confinement forces nucleoids to grow along the cell length, thereby promoting nucleoid segregation
494 along this cellular dimension. Keeping nucleoids close to the membrane across the cell width may act as a
495 diffusion barrier for polysomes from distinct DNA-free regions, preventing polysome accumulations to fuse
496 into larger phase condensates.
497
498 To test these ideas, we first treated cultures with A22 to inhibit cell width control through the inactivation of
499 MreB (Bean et al., 2009; Iwai et al., 2002). This resulted in cells with a polysome phase at the cell center
500 surrounded by a nucleoid phase around the cell periphery (Figure 7 – figure supplement 1, top). To further
501 increase the cell width (> 2.5-fold), we exposed cells to the cell division inhibitor cephalexin in addition to
502 A22 (Figure 7A and Figure 7 – figure supplement 1, bottom). As a control, we showed that cephalexin
503 treatment alone resulted in filamentous cells (of constant cell width) with multiple nucleoids separated by
504 polysome accumulations (Figure 7B), consistent with previous reports (Chai et al., 2014; Gray et al., 2019;
505 Thappeta et al., 2024). In cells treated with both drugs, we observed two types of subcellular
506 rearrangements. In smaller cells, which started with a single nucleoid, drug treatment resulted in a single
507 large polysome accumulation at the cell center, displacing the nucleoid into a toroidal shape at the cell
508 periphery (Figure 7C and Movie S6). In longer cells with two segregated nucleoids, the nucleoids expanded
509 and often aberrantly segregated along the cell width concomitant with polysome accumulation at the site of
510 nucleoid splitting (white arrowheads, Figure 7D). Consequently, a polysome "bridge" was formed between
511 the polysome accumulations flanking the nucleoid. These polysome bridges resulted in a characteristic
512 cross-like polysome pattern, marking the two axes (longitudinal and radial) of nucleoid segregation (Figure
513 7E). The loss of radial confinement led to coalescence of polysome accumulations toward the cell center
514 and fusion of nucleoids around the cell periphery (Figure 7C-E and Figure 7 – figure supplement 1). As a
515 result, the nucleoids and polysome accumulations decreased in number while increasing in size in
516 cephalexin/A22-treated cells compared to cephalexin-treated cells with the same cell area distribution but

517 normal cell width (Figure 7F). These results suggest a critical role for cell width regulation in limiting the
518 diffusion of polysomes around the nucleoid and thereby spatially controlling the phase separation between
519 polysomes and nucleoids to promote longitudinal nucleoid segregation.
520
521 **DISCUSSION**
522 ***The flow of genetic information intrinsically couples nucleoid segregation to cell growth.***
523 Polysomes, a term in which we include monosomes for simplicity, are made of mRNAs in complex with
524 ribosomes. This study provides experimental and theoretical evidence (Figures 1-7) that polysome
525 production within the nucleoid—an inherent product of chromosomal gene expression—contributes to
526 nucleoid segregation and positioning in *E. coli* cells. This may also be true in other bacteria, as reduced or
527 abrogated transcription via gene deletion or antibiotic treatment causes chromosome segregation defects
528 in *Streptococcus pneumoniae* (Kjos and Veening, 2014) and *Bacillus subtilis* (Dworkin and Losick, 2002).
529
530 Due to their anabolic footprint (Belliveau et al., 2021; Chure and Cremer, 2023; Dai et al., 2017; Dourado
531 and Lercher, 2020; Hu et al., 2020; Molenaar et al., 2009; Scott et al., 2014; Si et al., 2017), polysomes
532 integrate the rate of nucleoid segregation with that of gene expression and cell growth. The concentration
533 of polysomes and their rate of accumulation in the cell are a direct reflection of transcriptional and
534 translational activities in the cell (Balakrishnan et al., 2022). The higher the concentration of polysomes, the
535 faster is the growth rate. Thus, in our proposed model, an increase in polysome concentration not only
536 leads to more protein synthesis and faster cell growth, but also results in faster nucleoid segregation. The
537 reverse is true for a decrease in polysome concentration, inherently coupling these processes without the
538 help of a dedicated regulatory system. Such coupling was seen across isogenic cells with variable growth
539 rates in the same nutrient condition (Figures 1F, 1H and 2C-E) as well as across nutrient conditions that
540 led to a wide range of growth rates (Figure 2A-B and Figure 2 – figure supplement 1).
541
542 ***Directional nucleoid splitting requires phase separation and radial confinement.***
543 A key aspect of our proposed mechanism for nucleoid segregation is that polysomes form within nucleoids
544 due to chromosomal gene expression, which, together with polysome turnover due to mRNA decay, creates
545 an out-of-equilibrium system (Figure 4) (Miangolarra et al., 2021). Redirecting polysome formation to
546 plasmid gene expression led to ectopic polysome accumulations that dramatically affected nucleoid
547 dynamics (Figure 6 and Movie S5).
548
549 In normal cells, the effective force that segregates nucleoids appears to be linked to the propensity of the
550 chromosomal meshwork and polysomes to phase separate. Mutual exclusion is, at least in part, caused by
551 the steric repulsion between the two macromolecules. While ribosomes or ribosomal subunits freely diffuse
552 across the cell unobstructed by the presence of the nucleoid (Bakshi et al., 2012; Sanamrad et al., 2014),
553 the larger polysomes are impeded by the chromosomal mesh based on size considerations alone (Xiang

554 et al., 2021). Modeling studies have suggested that such steric hinderance between large crowders
555 (polysomes) and a polymeric meshwork (chromosome) can result in phase separation and polymer
556 compaction (Bakshi et al., 2014; Castellana et al., 2016; Miangolarra et al., 2021; Mondal et al., 2011; Wu
557 et al., 2019b). It is also possible that phase separation between nucleoids and polysomes involves non-
558 steric interactions such as electrostatic repulsion between the negatively charged DNA and RNA (mRNA
559 and rRNA), as previously hypothesized (Joyeux, 2015). Such steric and non-steric interactions may
560 contribute to the effective poor solvent quality of the polysome-rich cytoplasm for the chromosome (Xiang
561 et al., 2021). Future research will be necessary to elucidate the precise nature of the interaction between
562 chromosomes and mRNAs, whether individually or in complex with ribosomes.
563
564 We found that the width of the cell controls the dynamics of phase separation between polysomes and
565 nucleoids by radially confining the nucleoid and directing its growth and segregation along a single cellular
566 dimension, cell length (Figure 7). Radial confinement effectively prevents the diffusion and fusion of
567 polysome accumulations from distinct DNA-free regions, which leads to alternating enrichments of
568 polysomes and DNA along the length of elongating cells (Figure 7B). This radial confinement explains why
569 differences in RplA-GFP signal between DNA-free regions (Figure 3A-B and Figure 2 – figure supplement
570 2) do not equilibrate rapidly, validating our use of a 1D model. Diffusion restriction around nucleoids is
571 consistent with our previous report that polysomes diffuse much faster over short distances (within DNA-
572 free domains) than long distances (across DNA-free domains) (Gray et al., 2019). Loss of radial
573 confinement results in apparent fusion of polysome accumulations near the cell center and displacement
574 of nucleoids toward the cell periphery (Figure 7C-E). This phase separation between the polysomes and
575 the nucleoid likely contributes to the torus topology of nucleoids previously observed in A22-treated *E. coli*
576 (Wu et al., 2019a). Our findings highlight the importance of cell width regulation and suggests that nucleoid
577 segregation may have imposed an evolutionary constraint on cell morphology.
578
579 ***Nucleoid segregation likely involves multiple factors.***
580 Our models show that the most trivial case of uniform production of polysomes (i.e., uniform mRNA
581 synthesis) within the nucleoid is sufficient to cause an enrichment of polysomes at mid-nucleoid (Figure 4)
582 (Miangolarra et al., 2021). Inside cells, this polysome enrichment at mid-nucleoid may be enhanced by a
583 bias in mRNA synthesis across the nucleoid. For instance, the chromosomal region close to the origin of
584 replication has been shown to be more highly expressed per gene copy than other regions on the
585 chromosome (Scholz et al., 2019) and this region is located in the middle of the nucleoid prior to DNA
586 replication (Bates and Kleckner, 2005; Cass et al., 2016; Fisher et al., 2013; Kuwada et al., 2013, 2013;
587 Mäkelä et al., 2021; Sadhir and Murray, 2023; Wang et al., 2006). In addition, this highly expressed
588 chromosomal region is the first one to replicate, which should lead to further local increase in mRNA
589 expression due to a doubling in gene dosage (Pountain et al., 2022). However, it is important to reiterate

590 that such localized mRNA synthesis is not expected to be a prerequisite for polysome-based nucleoid
591 segregation since it is not included in our reaction-diffusion model (Figure 4).
592
593 Other factors are likely involved in nucleoid segregation. In fact, our data revives the abandoned sixty-year-
594 old hypothesis by Jacob et al. (1963) that cell growth and surface expansion separate the sister nucleoids,
595 but with two notable differences. First, the contribution of cell growth to nucleoid splitting would be partial
596 (Figure 1I and Figure 1 – figure supplement 3). Second, cell growth would contribute predominantly near
597 the end of the division cycle (Figure 1I). This late timing makes sense for two reasons. First, it corresponds
598 to the time when polysomes stop accumulating between the separated sister nucleoids and polysome
599 accumulations emerge at the middle of these nucleoids (i.e., at the ¼ and ¾ cell positions) to start the next
600 round of segregation (Figure 1D and Movie S2). Second, this is also when *E. coli* switches its cell wall
601 growth pattern from dispersed along the cell body to zonal and divisome-dependent at mid-cell (Cooper
602 and Hsieh, 1988; Gray et al., 2015; Navarro et al., 2022; Wientjes and Nanninga, 1989; Woldringh et al.,
603 1987). Indeed, zonal cell growth between the sister nucleoids was a key assumption of the original 1963
604 model (Jacob et al., 1963). Altogether, we propose a working model in which gene expression, which results
605 in polysome production within the nucleoid, promotes nucleoid splitting and accelerates the migration of the
606 resulting sister nucleoids apart, with cell elongation facilitating this latter function near the end of the cell
607 division cycle. DNA replication and processes that contribute to chromosome condensation and
608 organization (such as DNA loop extrusion, supercoiling, and preferential loading of DNA remodeling
609 complexes) are also likely to be important for robust chromosome segregation across all cells (Danilova et
610 al., 2007; Harju et al., 2023; Hofmann et al., 2019; Holmes and Cozzarelli, 2000; Lemon and Grossman,
611 2000; Mäkelä et al., 2021; Minnen et al., 2011; Sawitzke and Austin, 2000; Weitao et al., 1999).
612
613 We note that in our time-lapse experiments, the accumulation of polysome signal appeared to slightly
614 precede the depletion of DNA signal that marked the initiation of nucleoid splitting (Figure 1E). Polysome
615 enrichment in the middle of unconstricted nucleoids was also occasionally observed in snapshot images of
616 cells growing on glycerol, a slow growth condition that results in a single nucleoid segregation event late
617 during the cell division cycle (Figure 1 – figure supplement 4A-D). This is not seen in our model in which
618 polysome accumulation and nucleoid splitting occur at the same time (Figure 4A and Movie S3). This small
619 discrepancy may reflect a limitation of our experimental or modeling approach. For example, it is possible
620 that the point spread function of our fluorescent DNA marker slightly delays the moment at which we can
621 detect signal depletion at mid-nucleoid and thereby the initiation of nucleoid splitting. Alternatively, the small
622 difference in timing may be associated with a model simplification. In our model, the nucleoid is effectively
623 a solution of DNA fragments. In reality, the nucleoid consists of a circular polymer, crosslinked by nucleoid-
624 associated proteins. These DNA crosslinks may cause a small resistance that marginally delays the
625 initiation of nucleoid splitting relative to the polysome enrichment at mid-nucleoid.
626

627 ***E. coli is an asymmetric organism.***
628 The spatial macromolecular asymmetries uncovered in our study contrast with the common perception of
629 *E. coli* as a symmetric organism. Under our experimental conditions, the distribution of polysomes at the
630 new pole in newborn cells was, on average, higher than at the old pole through inheritance of the large mid-
631 cell accumulation of polysomes from their mother cells (Figure 3A and D). We also observed an asymmetric
632 distribution in DNA density within nucleoids, which correlated with the availability of polysome-free space
633 along the cell length and width (Figure 3E-G). This asymmetry emerged before cell division (Figure 3D and
634 Movie S2). Simulations of our reaction-diffusion model suggest that slower diffusing/relaxing nucleoids are
635 more likely to reproduce these nucleoid position and compaction asymmetries during the finite course of
636 the cell division cycle (Figure 4D). A reduction in the apparent nucleoid diffusivity has been linked to
637 nucleoid-associated proteins, which bridge and thus stiffen the DNA polymer (Subramanian and Murray,
638 2023). The physiological significance for these dynamic cellular asymmetries is not clear at this time, though
639 it is conceivable that a difference in DNA compaction within the nucleoid may affect gene expression.
640 Regardless, our study illustrates how spatial and temporal asymmetries in the cytoplasm can emerge from
641 the interactions between two of the most important macromolecules.
642
643 **METHODS**
644
645 **Strains and constructs**
646 Strains and plasmids used for this study are listed in Tables S2 and S3, respectively, while the sequences
647 of the oligonucleotides used to make constructs can be found in Table S4.
648
649 To measure the concentration and spatial heterogeneity of ribosomes inside *E. coli*, we used strains in
650 which the RplA 50S ribosome subunit protein (strains CJW7323, CJW6768, CJW7020 and CJW7651) or
651 the RpsB 30S ribosome subunit protein (strains CJW6769 and CJW7021) are fused with mEos2 (strains
652 CJW6768 and CJW6769), msfGFP (strains CJW7020, CJW7021, CJW7651, and CJW7798) or GFP
653 (CJW7323) (Gray et al., 2019; Xiang et al., 2021). Nucleoid characteristics were measured using strains in
654 which HupA, a nucleoid-associated protein, is fused with mCherry (strains CJW7323, CJW6723 and
655 CJW7798) (Xiang et al., 2021). Alternatively, DAPI was used to stain the DNA (strains CJW6768,
656 CJW6769, CJW7020, CJW7021, and CJW7651).
657
658 The mCherry-μNS (CJW7651) particles were chromosomally expressed from the native Lac promoter after
659 induction with 150 μM IPTG (for 3 h for agarose pad experiments, or continuously for microfluidics
660 experiments). Strain CJW7651 was constructed as follows. The *gfp* coding sequence in the pER12
661 (pBAD322A-gfp-μNS) plasmid (kind gift from Dr. A. Janakiraman, City College of New York) was swapped
662 with the mCherry-coding sequence using megaprimer whole plasmid (MEGAWHOP) cloning (Bryksin and
663 Matsumura, 2010) and the primer pair ER12-MCR-fwd/ER12-MCR-rev2 to generate plasmid pER12-
664 mCherry. The mCherry-μNS coding sequence and the *rrnB* transcriptional terminator were amplified from

665 the pER12-mCherry plasmid (primer pair μNSmCherry fwd/rev) and assembled with the *frt* site flanked with
666 a kanamycin resistance cassette (amplified from pKD13 (Datsenko and Wanner, 2000) using the primer
667 pair FRT_KanR fwd/rev) and the ColE1 origin of replication (PCR amplified from the pBAD22A plasmid
668 (Guzman et al., 1995) using the primer pair ColE1 fwd/rev) using Gibson DNA assembly (Gibson et al.,
669 2009) to form the pAPG1 plasmid. The pAPG1 plasmid also included two 50 bp sites homologous to the
670 *attB* region of the *E. coli* chromosome, introduced as overhangs in the primers used for Gibson DNA
671 assembly. The *attB* homologous regions allowed for the integration of the arabinose inducible mCherry-
672 μNS expression cassette into the respective site, though this was not used in this study. The pAPG1
673 plasmid was verified by sequencing using the pAPG1 seq1-5 primers. The mCherry-μNS coding sequence
674 was then PCR amplified from the pAPG1 plasmid using primer pair lacZYA_redμNS fwd/rev, which includes
675 50-bp overhangs homologous to the region upstream and downstream of the *lacZYA* operon, and
676 integrated downstream of the *lac* promoter in the MG1655 strain (Guyer et al., 1981; Jensen, 1993) using
677 lambda red recombination and the pKD46 plasmid (Datsenko and Wanner, 2000) for the construction of
678 the CJW7144 strain. Correct insertion of the mCherry-μNS coding sequence to substitute the *lacZYA*
679 operon coding sequences was confirmed by colony PCR using primer pairs LacI_fwd/CynX_rev and
680 LacI_fwd/mCherry_rev. Transduction with a P1 phage lysate of the CJW7144 strain was used to transfer
681 the mCherry-μNS expression cassette into the CJW7020 strain using kanamycin as a selection marker. As
682 a result, the CJW7145 strain was constructed, which was verified using colony PCR and the primer pairs
683 LacI_fwd/CynX_rev and LacI_fwd/mCherry_rev, KanR_fwd/CynX_rev. The CJW7145 strain was then
684 transformed using the pCP20 plasmid (Datsenko and Wanner, 2000), which encodes the FLP recombinase
685 (Cherepanov and Wackernagel, 1995) to remove the kanamycin resistance cassette, yielding the CJW7651
686 strain.
687
688 The CJW7798 strain was derived from the MG1655 (DE3) strain (Tseng et al., 2010a), which carries the
689 T7 RNA polymerase-encoding gene under *lacUV5* control. Transduction with a P1 phage lysate of the
690 CJW5158 strain (Gray et al., 2019) was used to transfer the gene encoding the HupA-mCherry fusion into
691 the MG1655 (DE3) strain using kanamycin as a selection marker. The pCP20 plasmid (Datsenko and
692 Wanner, 2000), which encodes the FLP recombinase (Cherepanov and Wackernagel, 1995), was used to
693 remove the kanamycin resistance cassette, yielding the CJW7466 strain. Transduction with a P1 phage
694 lysate of the CJW7019 strain, a kanamycin-resistant intermediate of strain CJW7020 (Gray et al., 2019),
695 was used to transfer the gene encoding the RplA-msfGFP fusion into the CJW7466 strain using kanamycin
696 as a selection marker. The resulting strain (CJW7766) was grown in the presence of kanamycin since the
697 cells tend to lose msfGFP fluorescence in the absence of the antibiotic. The sequence of the CJW7766
698 strain was confirmed by whole genome sequencing.
699
700 The pET28:mTagBFP2 plasmid variant was derived from the pET28:GFP plasmid (Shis and Bennett,
701 2013), which was a gift from Mathew Bennett (Addgene plasmid # 60733 ; http://n2t.net/addgene:60733;

RRID:Addgene_60733). First, the GFP coding sequence was substituted with the mTagBFP2 coding sequence from the pBAD-mTagBFP2 plasmid (Subach et al., 2011), a gift from Vladislav Verkhusha (plasmid # 34632; http://n2t.net/addgene:34632; RRID:Addgene_34632). Specifically, the mTagBFP2 coding sequence was amplified using the primer pair mTagBFP2 fwd/rev and assembled (Gibson DNA assembly) with the pET28 backbone, which was amplified in two pieces using the pET28_one fwd/rev and the pET28_two fwd/rev primer pairs to derive the pET28:mTagBFP2 plasmid. Then, the kanamycin resistance cassette that was originally present in the pET28 backbone was substituted with the chloramphenicol resistance cassette from the pSB3C5-proA-B0032-E0051 plasmid (Davis et al., 2011) which was a gift from Joseph Davis and Robert Sauer (Addgene plasmid # 107244; http://n2t.net/addgene:107244; RRID:Addgene_107244). Specifically, the backbone of the pET28:mTagBFP2 plasmid excluding the kanamycin resistance cassette was amplified using the pET28mTagBFP2 fwd/rev primers and assembled (Gibson DNA assembly) with the coding sequence of the chloramphenicol resistance cassette that was amplified using the cmR fwd/rev primer pair. As a result, the pET28:mTagBFP2-CmR plasmid was created. The proper assembly of the pET28:mTagBFP2 and pET28:mTagBFP2-CmR plasmids were confirmed by sequencing.

The pET28:mTagBFP2-CmR plasmid was introduced into CJW7766 by electroporation to create the CJW7798 strain, which was used to redirect the ribosomes away from the nucleoid onto the plasmid-expressed mTagBFP2 mRNAs after inducing the expression of T7 RNA polymerase with IPTG.

Growth conditions

Strains CJW6769, CJW7020 and CJW7021 used in Figure 2 and Figure 2 – figure supplement 1 were grown as previously described (Gray et al., 2019) using a basic M9 medium formulation without trace elements and supplemented with 0.2% (w/v) carbon source and when specified with 0.1% (w/v) casamino acids (CAA) and 1 µg/mL thiamine (T). The strain CJW6768 (used in Figure 2 and and Figure 2 – figure supplement 1) was grown using the same medium formulation. The abbreviations of the medium growth conditions presented in Figure 2A and Figure 2 – figure supplement 1 are defined in Table S1. For the rest of our experiments on agarose pads or in a microfluidic device, strains CJW7323, CJW7651 and 7798 were grown in M9 salts (final concentrations: 33.7 mM Na_2HPO_4, 22 mM KH_2PO_4, 8.55 mM NaCl, 9.35 mM NH_4Cl, 1 mM $MgSO_4$, 0.3 mM $CaCl_2$) supplemented with trace elements (Fe, Zn, Cu, Co, B, Mn), 0.1% (w/v) thiamine, and, when specified, 0.4% (w/v) casamino acids. The pH of the 10x M9 salts was adjusted to 7.2 with NaOH. The trace elements were added at a final concentration of 13.4 mM ethylene-diamine-tetra-acetic-acid, 3.1 mM of $FeCl_3$-$6H_2O$, 0.62 mM of $ZnCl_2$, 76 µM of $CuCl_2$-$2H_2O$, 42 µM of $CoCl_2$-$2H_2O$, 162 µM of HBO_3-$2H_2O$, 8.1 µM of $MnCl_2$-$4H_2O$.

To achieve steady-state exponential growth prior to imaging, a stationary phase liquid culture in the appropriate growth medium was diluted at least 10,000 times and grown to an optical density at 600 nm (OD_{600}) between 0.1 and 0.3. These cells were either loaded in a mother-machine-type microfluidics device

740 (Lin and Jacobs-Wagner, 2022; Wang et al., 2010) where they were grown under the constant flow of
741 medium (~0.5 μL/sec), or spotted on 1% agarose pads prepared with the same growth medium. In the
742 microfluidic device, cells were grown for at least 3 h prior to image acquisition. All precultures and
743 experiments were performed at 30ºC.
744
745 The mCherry-μNS particles (CJW7651 strain) were imaged on agarose pads after inducing exponentially
746 growing cells with 150 μM IPTG for 3 h (Figure 4E-G). Before spotting on the 1% agarose pad, the induced
747 cells were stained with DAPI (1 μg/mL) for 5 min. In both experiments, the cells were growing in
748 M9gluCAAT.
749
750 To redirect ribosomes to plasmid-expressed, T7 promoter-driven mTagBFP2 mRNAs, exponentially
751 growing CJW7798 cells grown in M9glyCAAT to an OD ~ 0.2 were spotted on a 1% agarose pad containing
752 M9glyCAAT and 100 μM IPTG, the latter to induce the expression of the T7 RNA polymerase.
753
754 **Rifampicin treatment**
755 The antibiotic rifampicin (see Table S5) was used to block transcription, deplete mRNAs, and release the
756 mRNA-bound ribosomes (polysomes). Rifampicin treatment was performed either in batch culture (Figure
757 1 – figure supplement 1F) or in microfluidics (Figure 5 and Movie S4).
758
759 For the microfluidic experiment, two rounds of rifampicin treatment were performed by switching between
760 M9gluCAAT containing antibiotic (100μg/mL) and antibiotic-free medium at 30ºC. For the medium switches,
761 solenoid valves were used in a custom-built pressurized perfusion system, achieving fast (within 1 min)
762 changes in the cellular environment. The first switch to rifampicin occurred 2 h after normal growth in
763 antibiotic-free medium (Figure 5A and Movie S4). Rifampicin treatment lasted 2 h until the system switched
764 back to antibiotic-free medium, where cells were left to recover for 8 h. Twelve hours into the experiment,
765 the system switched again to rifampicin-containing medium.
766
767 **A22 and cephalexin treatment**
768 Cephalexin (50 μg/mL) and A22 (4 μg/mL) (see Table S5) were added to exponentially growing CJW7323
769 cell cultures (OD_{600} ~ 0.1) in M9gluCAAT just prior to spotting on a 1% agarose pad, which was made with
770 the same growth medium and contained the same antibiotic concentrations. The radial expansion of the
771 cells and the polysome and nucleoid signals were tracked over time in a time-lapse experiment. The
772 selected concentration of A22 has previously been shown to not affect cell growth (Takacs et al., 2010). All
773 precultures and time-lapse imaging experiments were performed at 30ºC.
774
775
776

777 **Ectopic polysome accumulation experiment**
778 Exponentially growing CJW7798 cells in M9glyCAAT supplemented with kanamycin (50 µg/mL) and
779 chloramphenicol (35 µg/mL) were washed one time with M9glyCAAT minimal medium lacking antibiotics
780 but supplemented with 100 µM IPTG (see Table S5). The washed cells were spotted on a 1% agarose pad
781 prepared with M9glyCAAT also supplemented with IPTG (100 µM) for time-lapse imaging. All pre-cultures
782 and time-lapse imaging experiments were performed at 30ºC. Since chloramphenicol affects protein
783 synthesis and thus polysome formation, the agarose pads lacked chloramphenicol, resulting in a fraction
784 that loss the plasmids based on the absence of blue fluorescence. Therefore, only cells that expressed blue
785 fluorescence (and thus carried the pET28:mTagBFP2-CmR plasmid) were analyzed.
786
787 **Microscopy**
788 Strains CJW6769, CJW7020, and CJW7021 used in Figure 2A-B and Figure 2 – figure supplement 1, were
789 imaged on agarose pads using the same microscopy set-up and optical configurations as previously
790 described (Gray et al., 2019). Snapshots of the CJW6768 strain (used in Figure 2A-B and Figure 2 – figure
791 supplement 1) were taken using a Nikon Ti-E microscope equipped with a 100x Plan Apo 1.45NA Ph3 oil
792 objective, a Hamamatsu Orca-Flash4.0 V2 CMOS camera (16-bit, Slow Scan sensor mode) and a
793 Lumencor Spectra X LED (Light Emitting Diode) engine. The 395/25nm LED was used to excite DAPI and
794 the 470/24nm LED was used to excite GFP. DAPI fluorescence was acquired using an ET350/50x
795 (excitation filter), RT400lp (dichroic mirror), ET460/50m (emission filter) filter cube from Chroma. The
796 ET470/40x (excitation filter), T495lpxr (dichroic mirror), ET525/50m (emission filter) configuration from
797 Chroma was used for GFP fluorescence acquisition. The microscope was controlled using the NIS
798 Elements software by Nikon and the ND acquisition module.
799
800 For the time-lapse observation of cells (strain CJW7323) treated with A22 and/or cephalexin, images were
801 taken using a Nikon Ti-E microscope, equipped with a 100x Plan Apo 1.45NA Ph3 oil objective, a
802 Hamamatsu Orca-Flash4.0 V2 CMOS camera (16-bit, Slow Scan sensor mode), and a Sola solid state
803 white light source (Lumencor), in a temperature-controlled enclosure (Okolabs). The AT470/40x excitation
804 filter, combined with a T495LPXR beam-splitter and an ET525/50m emission filter, was used for GFP. For
805 mCherry visualization, the ET560/40x excitation filter, combined with a T585lp beam-splitter and a
806 ET630/75m emission filter, was used. A neutral density filter (32x) was applied in the excitation path to
807 reduce phototoxicity and photobleaching. Images were taken every 2.5 min in the brightfield channel (phase
808 contrast) and every 5 min in the fluorescence channels (RplA-GFP and HupA-mCherry).
809
810 For the rest of the brightfield and epi-fluorescence wide-field microscopy experiments (strains CJW7323,
811 CJW7651, and CJW7798), snapshots or time-lapse images were taken using a Nikon Ti2-E inverted
812 microscope, equipped with a 100x Plan Apo 1.45NA Ph3 oil objective, a Photometrics Prime BSI back-
813 illuminated sCMOS camera (2048x2048 pixels sensor with a pixel size of 6.5 µm), and a Lumencor Spectra

814 III LED (Light Emitting Diode) engine, in a temperature-controlled enclosure (Okolabs). The HDR 16-bit
815 sensor mode was used to acquire images. The microscope was controlled using the NIS Elements software
816 by Nikon, and the JOBS or the ND acquisition module were used to acquire snapshots or time-lapse
817 images. The Perfect Focus System (by Nikon) was used to maintain focus in microfluidics experiments.
818 The auto-focus function in NIS Elements was used to locate the optimal z-position in agarose pad
819 experiments (snapshots or time-lapse). For the DAPI, BFP, GFP, or mCherry channels, a polychroic mirror
820 (FF-409/493/596-Di02 by Shemrock) combined with a triple-pass emitter (FF-1-432/523/702-25 by
821 Shemrock) was used. For DAPI, BFP, and GFP imaging, additional emission filters were applied in the
822 optical path (FF01-432-36 by Shemrock, FF01-432-36 by Shemrock and ET525/50M by Chroma,
823 respectively). DAPI, BFP, GFP, and mCherry were excited using a 390/22nm, 390/22nm, 475/28nm and
824 575/25nm LED, respectively.
825
826 For the microfluidic experiments (strain CJW7323), the excitation light intensity was reduced to 20% for the
827 1-min interval and 30% for the 3-min interval imaging of the RplA-GFP and HupA-mCherry. An exposure
828 time of 120-ms was used for both markers. In all time-lapse experiments, a neutral density filter (absorptive
829 ND filter, OD:1.3 / 5% transmission, NE13B by Thorlabs) was also applied to reduce the LED power and
830 minimize phototoxicity and photobleaching. The LED powers (factored by the neutral density filters) were
831 calibrated using a microscope slide power meter with an 18x18 mm sensor size (S170C by Thorlabs). The
832 light intensity was measured for each excitation wavelength (475/28nm and 575/25nm) at the end of the
833 objective (without immersion oil) for different LED intensities (% of maximum intensity). From the generated
834 calibration curves, the RplA-GFP excitation light power was estimated to be 524 μW and 629 μW for the 1-
835 min and 3-min fluorescence interval imaging, respectively. HupA-mCherry was excited with 109 μW light
836 power for the 1-min and 191 μW for the 3-min fluorescence interval imaging.
837
838 The type N immersion oil (by Nikon) was used in all experiments except for the time-lapse observation of
839 A22+cephalexin-treated cells where the type F immersion oil (by Nikon) was used. All imaging (time-lapse
840 and snapshots) was done at 30ºC.
841
842 **Analysis software and code availability**
843 Cropping and alignment of the microfluidic channels were performed with MATLAB (www.mathworks.com)
844 using a previously published pipeline from our lab (Lin and Jacobs-Wagner, 2022). Supervised classification
845 and curation of the Oufti cell meshes was also implemented in MATLAB (Campos et al., 2018; Govers et
846 al., 2024; Gray et al., 2019). For the T7 experiments, segmentation and tracking of the CJW7798 cells was
847 performed using the Omnipose deep neural network architecture (Cutler et al., 2022), using a previously
848 trained model (Thappeta et al., 2024) and the SuperSegger MATLAB-based package (Stylianidou et al.,
849 2016). The remaining analyses were performed using Python 3.9 (www.python.org), that included the
850 *numpy* (Harris et al., 2020), *scipy* (Virtanen et al., 2020), *pandas* (McKinney, 2010), *scikit-mage* (Van Der

Walt et al., 2014), *scikit-learn* (Pedregosa et al., 2012), *shapely* (Gillies, Sean et al., 2023), *statsmodels* (Seabold and Perktold, 2010) and *pytorch* (Paszke et al., 2019) libraries. The *matplotlib* (Hunter, 2007) and *seaborn* (Waskom, 2021) libraries were used for plotting. The analysis pipeline and functions (summarized in Table S6) are available in the Jacobs-Wagner lab GitHub repository: www.github.com/JacobsWagnerLab/published/tree/master/Papagiannakis_2024.

Cell segmentation and tracking

For the CJW6768, CJW6769, CJW7020, and CJW7021 strains used in Figure 2 and Figure 2 – figure supplement 1, Oufti (Paintdakhi et al., 2016) was used to draw cell meshes on the phase contrast snapshots and a MATLAB-based support vector machine model was used to remove the badly segmented cells as previously described (Campos et al., 2018; Govers et al., 2024; Gray et al., 2019).

The Omnipose deep neural network architecture (Cutler et al., 2022) with a previously trained model (Thappeta et al., 2024) was used to segment the CJW7798 cells during T7 RNA polymerase induction on an agarose pad. The segmented cells were then tracked using SuperSegger (Stylianidou et al., 2016). A custom class (*omnipose_to_python_ghv.py*) was developed to transfer the SuperSegger segmentation and tracking data into Python for post-processing.

Due to the unusual and variable morphology of the A22/cephalexin-treated cells, a custom Python class was developed for their segmentation and tracking. The *Otsu_phase_segmentation_ghv.py* class segments the cells by applying an Otsu-threshold (Otsu, 1979) on the inverted phase images, followed by binary dilation (*scikit-image.morphology.binary_dilation* Python function) hole filling (*scipy.ndimage.binary_fill_holes* Python function), and binary closing (*scikit-image.morphology.binary_closing Python function*). The segmentation masks were tracked between subsequent timepoints, using cell distance as well as cell area constraints, and linked into cell growth trajectories. Cell morphology criteria such as the maximum pixel distance from the medial axis and the medial axis sinuosity were used to remove bad segmentations. The remaining segmentation masks were manually curated.

For the other experiments on agarose pads, a neural network (Wiktor et al., 2021; Zhou et al., 2020) with a previously designed and trained U-net architecture (Mäkelä et al., 2024) was used to segment single cells based on phase contrast snapshots. The generated segmentation masks were further processed by watershed separation, filling the holes within masks and removing unusually small masks. Finally, a graphical interface was used to manually remove the badly curated cells (less than 5% of the segmented cell population).

In contrast to the Oufti software (Paintdakhi et al., 2016) that generated sub-pixel meshes around the cell boundaries, the other applied segmentation algorithms returned pixel-based cell masks. To deal with this discrepancy, the sub-pixel cell meshes from Oufti were converted into pixel-based cell masks by collecting the pixels within the circumscribed single cell area in Python (*oufti_snapshots_GrayGovers* class, included in the *snapshots_analysis_OUFTI_GrayGovers* Python script). After this conversion, the same Phyton-based functions were applied for the analysis of the cell fluorescence and morphology statistics regardless of the segmentation method used.

To segment cells growing in the microfluidic device, a custom library of image analysis functions (*mother_machine_segmentation* class, included in the *microfluidics_segmentation_ghv* Python script) was developed in Python. This algorithm was applied on the cropped, aligned, background-subtracted, and inverted phase contrast images that were produced using a previously published pipeline (Lin and Jacobs-Wagner, 2022) in MATLAB. Cell segmentation was performed in three steps. First, all the cells within the microfluidics channel, which were brighter than the microfluidic channel background in the inverted and background-corrected phase-contrast channel, were segmented using an Otsu intensity threshold (Otsu, 1979). This crude thresholding step, which separated the cell (brighter: 1) from the background (darker: 0) pixels, yielded at least one masked label for the entire row of stacked cells in each microfluidic channel. A watershed segmentation was then applied to define the boundaries between individual cells and split the Otsu-based binary mask(s). The watershed algorithm was guided by the number of cells and their relative positions in the microfluidic channel, which were determined using an adaptive filter combined with the local decrease of the inverted phase intensity between the poles of adjacent cells. Finally, a graphical interface was used to curate the cell masks by manually splitting or merging cell labels.

After segmentation, the curated single-cell masks were tracked over time and linked into trajectories from birth to division using the centroid distance and the relative area difference between cells at consecutive time-points (*mother_machine_tracking* class, included in the *microfluidics_segmentation_ghv* Python script). Examples of cell segmentation and tracking in microfluidics are shown in Movie S1 and Figure 1 – figure supplement 1A. Regardless of the image acquisition time intervals for the fluorescence channels, phase-contrast images were acquired every minute, which allowed for accurate cell tracking.

Fluorescence background correction was different between the microfluidic and agarose-pad experiments. In microfluidics, the average background was measured within two 8-pixel (0.528 μm) wide areas, one on the left side and one the right side of the channel, at least 10 pixels (0.66 μm) away from the channel boundaries from top to bottom. The estimated background was then subtracted along the channel length. The background correction was integrated in the *get_fluorescence_image* function, located in the *microfluidics_analysis_functions*_ghv Python script.

In agarose-pad experiments, an Otsu threshold (Otsu, 1979) was used on the inverted phase-contrast image to segment all cells. A binary dilation was then performed on these crude cell masks before estimating the local average fluorescence of the unmasked pixels (pixels outside the dilated cell masks). The locally-averaged background was then used to fill in the cell areas and reconstruct the background of the entire field of view in the absence of cells. The smoothed (Gaussian smoothing) reconstructed background fluorescence was subtracted from each fluorescence image. This background correction pipeline (*back_sub* function) is integrated in both the *unet_snapshots* class and the *oufti_snapshots_GoversGray* class. For the time-lapse imaging of A22-treated CJW7323 cells (Figure 7) and CJW7798 cells during induction of T7 RNA polymerase expression (Figure 6), the fluorescence background was not subtracted since we did not need to quantify the raw pixel values. The normalized polysome and nucleoid fluorescence normalized by the average whole cell fluorescence is shown instead, marking the relative macromolecular rearrangements.

mCherry-μNS particle localization and tracking

For the localization of the diffraction-limited mCherry-μNS particles (Figure 4E-G), a set of custom functions were developed in Python and implemented in the *particle_positions_snapshots* class, included in the *snapshots_analysis_UNET_ghv* Python script.

The fluorescent particles were segmented in the background corrected mCherry-μNS fluorescence images using a Laplace of Gaussian (LoG) and an adaptive filter combined. The particle masks that had an area larger than a specified threshold (80 pixels for the microfluidics and 90 pixels for the agarose-pad experiments), which usually included two particles from the same or adjacent cells, were further processed by applying a relative fluorescence threshold (90th percentile of masked pixel intensity) to find the local fluorescence maxima and separate the two objects. Additional minimum area and aspect ratio constraints were applied. To accurately estimate the particle position with sub-pixel resolution, a 2D Gaussian function (eq. 1) with rotation (eq. 2) was fitted (least square method: *scipy.optimize.leastsq*) to an area of 7x7 pixels centered at the centroid of the particle mask:

$$g(x,y) = A\exp\left(-\frac{1}{2}\left(\left(\frac{x_0-x_{rot}}{\sigma_x}\right)^2 + \left(\frac{y_0-y_{rot}}{\sigma_y}\right)^2\right)\right) \quad \text{[eq. 1]}$$

and

$$\begin{aligned} x_{rot} &= x\cos(\theta) - y\sin(\theta) \\ y_{rot} &= x\sin(\theta) + y\cos(\theta) \end{aligned} \quad \text{[eq. 2]}$$

where x and y are the coordinates in the 2D imaging plane, A is the amplitude of the fitted Gaussian, σ is the standard deviation in each dimension, and θ is the rotation angle in radians, which was used to rotate the Gaussian distribution (x_{rot},y_{rot}) around the particle center or the Gaussian mean (x_0,y_0).

Two-dimensional cell mapping and alignment

Ribosome and nucleoid fluorescence statistics, as well as particle positions within cells, were mapped in relative 2D cellular coordinates from pole to pole and across the cell width. Such mapping allowed us to project the fluorescence or position statistics in 1 or 2D for specific cell length ranges and cell division cycle intervals. For this analysis, it was necessary to draw the medial axis for each of the segmented cells, which was obtained differently in microfluidic and agarose-pad images.

In the microfluidic experiments, where all the cells were stacked in a vertically oriented channel, the medial axis was drawn by fitting a second-degree polynomial to the most distant coordinates from the cell boundaries, excluding the cell caps at the poles where the medial axis was linearly extrapolated. The length of the cells, which was parallel to the length of the microfluidic channel, was used as the independent variable for the fitting. This medial axis estimation is implemented via the *all_medial_axis* function in the *microfluidics_analysis_functions_ghv* Python script.

However, in the agarose-pad experiments, cells were randomly oriented in the imaging plane. Thus, it was impossible to use one of the coordinates (x or y) as the independent variable as this would bias our medial axis estimation toward the same coordinate for cells that were not diagonally oriented. Instead, we developed an algorithm that scanned through the middle of the cells with a fixed sub-pixel step and directionality constraints to identify nodes at the most distant locations from the cell boundaries. These ordered (from pole to pole) and numbered nodes were used to fit the x and y coordinates of the medial axis separately, using the number of the node as an independent variable and its position coordinates as dependent variables. The degree of the fitted polynomials (*d*) scaled linearly with the total number of nodes (*N*) based on the relation $d = 0.1N - 5$. Similar to the microfluidic experiments, the medial axis was linearly extrapolated at the cell caps. This medial axis estimation is implemented using the *get_medial_axis* function in both the *unet_snapshots* and *oufti_snapshots_GoversGray* classes located in the *snapshots_analysis_UNET_ghv* and *snapshots_analysis_OUFTI_GrayGovers_ghv* Python scripts respectively. The medial axis estimation function is also provided as a separate function in the *Bivariate_medial_axis_estimation.py* Python script.

The medial axis of each cell, with a resolution of 0.1 pixel, was used to map the cell pixels and particle positions along the cell length and width. The projection of each pixel or particle position on the medial axis, defined as the most proximal node on the central line, was used to determine its cell length coordinate. The distance between the pixel or particle position and its medial axis projection was used to determine its absolute cell width coordinate. The sign of the cross product $\overrightarrow{PL} \times \overrightarrow{PC}$ (plus or minus), where *L* was the location of the particle, *P* was its projection on the medial axis, and *C* was the center of mass of the cell mask, was used to determine the position of particles or cell pixels on the sagittal plane.

Cell polarity and ages

In time-lapse experiments, the old and new poles of the cells were determined as follows. The pole of the daughter cell that was closer to the mid-cell position of its predivisional mother cell, where cell constriction occurs, was defined as the new pole. The medial axis coordinates were adjusted based on this polarity. As a result, the relative cell length extended from -1 to 1, with -1 corresponding to the old pole, 1 to the new pole, and zero to the cell center (see Figure 3 – figure supplement 1B, D and E). The implementation of this method is included in the *get_polarity* function in the *microfluidics_analysis_functions_ghv* Python script.

Cell lineages and ages relative to the oldest mother cells (first lineage) at the closed end of the microfluidic channel were determined using the orientation of the cell poles. The daughter cells that had the same polarity as the oldest mother cells were assigned the same age and lineage as their mothers. The daughter cells with the opposite polarity, which inherited the new pole of their mother cells, were considered younger and belonged to the second lineage. The daughter cells of mother cells belonging to the second lineage were classified as lineages three and four depending on their polarity. Cells from the third lineage had opposite polarity and those from the fourth lineage had the same polarity as their second lineage mother cells. Finally, mother cells from the third lineage, which inherited the new pole of their second-lineage mother cells, divided to yield the fifth and sixth cell lineages. The fifth lineage had the same polarity as its third-lineage mother and its sister lineage (sixth) had the opposite polarity and inherited the new pole from its third-lineage mother cell. The implementation of this method is included in the *get_ages* function in the *microfluidics_analysis_functions*_ghv Python script. For the analysis of the data presented in Figure 3, only the third, fourth, fifth and sixth lineages were considered to avoid age-related effects at the cell poles (Chao et al., 2023; Coquel et al., 2013; Koleva and Hellweger, 2015; Łapińska et al., 2019; Lindner et al., 2008; Proenca et al., 2019).

Construction of intensity profiles, 2D cell projections, demographs, and kymographs

With the ribosome and nucleoid fluorescence pixels as well as the μNS particle positions inside the cells having been mapped, the fluorescence and particle statistics from pole to pole (medial axis projection) and across the cell width (distance from the medial axis) were plotted for different cell division cycle intervals or cell length ranges.

An intensity profile represents the change in a fluorescence statistic along the cell from one pole to the other. Such a fluorescence statistic can be the average fluorescence intensity (as in Figures 1D, 3G, 4G, and Figure 3- figure supplement 1B), which corresponds to the concentration of the reported protein per cell area (sum of pixels divided by the number of pixels). In other analysis (as in Figure 5C and Figure 1 – figure supplement 4C), the protein concentration along the cell length was divided by the whole cell average. This scaled statistic is expressed as a percentage change relative to average concentration (mean

1036 %). A value above 100 indicates increase above the average, whereas a value below 100 corresponds to
1037 a decrease below the average concentration. This scaled statistic is insensitive to the RplA and HupA
1038 concentration variability between cells, or to the maturation of the GFP or mCherry fluorophores. As a result,
1039 the scaled concentrations showcase rearrangements of the tagged proteins and do not imply changes in
1040 protein synthesis relative to cell growth.
1041
1042 Intensity profiles were plotted for single cells (Figure 3 – figure supplement 1B and Figure 1 – figure
1043 supplement 4A) or populations (as in Figures 1D, 3G, 4G, 5C, 5E). In the second instance, the intensity
1044 profiles represent the average 1D projection of the fluorescence statistic for a specific cell division cycle
1045 interval, cell length range, growth rate range, polysome and nucleoid asymmetry group, or time range (e.g.,
1046 during antibiotic treatment). To generate a single-cell intensity profile, the medial axis length and its
1047 projected pixels were binned, and the average value of the selected fluorescence statistic was calculated
1048 per bin. If the number of bins was higher than the length of the medial axis in pixels, the missing values
1049 were filled in by linear interpolation. To avoid artefacts from the cell boundaries, the intensity profile was
1050 estimated for a box with a width of six pixels (~0.4 μm) centered on the medial axis (i.e., three pixels on
1051 each side of the medial axis). The intensity profile was occasionally smoothed by a moving average of a
1052 specified cell-length window, without excluding the bins at the edges which were not smoothed.
1053 Alternatively, a univariate spline (*scipy.interpolate.UnivariateSpline*) was fitted to the cell-length-binned data
1054 (as in Figure 4G). The univariate splines were fitted to the binned fluorescence intensity along the cell
1055 length. The number of cell length bins (N_{bin}) linearly scaled with the cell length in μm (l_{cell}) using the first-
1056 order relationship: $N_{bin} = \frac{100}{4.3}\, l_{cell}$ (only the whole part of the decimal was considered). Similar to the
1057 intensity profile where a fluorescence statistic was plotted along the cell length, the density profiles
1058 (histograms of the particle positions along the cell) for the mCherry-μNS (Figure 4G) particles along the cell
1059 were also plotted. Note that the intensity profiles shown in Figures 1D, 3G, 4G, 5C, 5E, Figure 1 – figure
1060 supplement 1D, and Figure 2 – figure supplement 2D are averages of many segmented cells or cell division
1061 cycles. In these averaged profiles, the variability in the timing of nucleoid segregation across cells
1062 attenuates the appearance of polysome accumulation. Furthermore, the point spread function of fluorescent
1063 ribosome markers causes an underestimation of the magnitude of the polysome accumulations in epi-
1064 fluorescence micrographs (Bakshi et al., 2012).
1065
1066 The intensity profiles were also used to construct demographs from agarose-pad experiments (Figure 2A,
1067 Figure 2 – figure supplement 1, and Figure 1 – figure supplement 4B) where cells were sorted by cell length
1068 from the shorter newborn to the longer predivisional cells. Intensity profiles were also used to construct
1069 ensemble kymographs from microfluidic experiments where the cells were sorted by their relative position
1070 in the cell division cycle (Figures 1C and 2D) or single-cell kymographs from agarose pad time-lapse
1071 measurements (Figure 6D-F). Specifically, the average intensity profile was estimated for each cell length
1072 or cell division cycle bin, and the average intensity profiles were stacked from birth to division (left to right)

1073 oriented according to the cell polarity (top to bottom). In the ensemble kymographs, the fluorescence
1074 intensities were projected along the relative cell length (cell length %), whereas in the single-cell
1075 kymographs the length of the projection linearly scales with the cell length. A Gaussian smoothing
1076 (*skimage.filters.gaussian*) was applied to smooth the demographs and ensemble kymographs.
1077
1078 In addition to the intensity or density profiles for a fluorescence statistic or the density of the μNS particles
1079 along the medial axis, 2D projections of the ribosome or nucleoid signal distribution (Figures 1D, 3D, 3G,
1080 4F, 5C, 5E, and Figure 2 – figure supplement 2A) as well as the μNS particle positions (Figure 4F) were
1081 also constructed. These 2D intensity or density maps were constructed by binning the cell pixels or particle
1082 positions not only by cell length, but also by cell width. The average fluorescence statistic or the particle
1083 density was then shown per bin, including data from many single cells within a specified cell division cycle
1084 or cell length range. A Gaussian smoothing (*skimage.filters.gaussian*) was applied to smooth the 2D
1085 projections.
1086
1087 **Extraction of population-level statistics of polysomes and nucleoids**
1088 To quantify the correlation between polysome accumulation and nucleoid segregation at the population
1089 level (Figure 2A-B and Figure 2 – figure supplement 1), the average polysome accumulation at mid-cell
1090 was extracted from cell snapshot images. This statistic was obtained by averaging the scaled (divided by
1091 the whole cell average concentration) RplA-GFP and HupA-mCherry intensity profiles of all the cells in the
1092 population. Therefore, this statistic describes the average "behavior" of the population under a specific
1093 growth condition. We reasoned that if, in a specific nutrient condition, nucleoid segregation happens earlier
1094 during the division cycle, then a higher fraction of the population will have segregated nucleoids. If so, the
1095 scaled HupA-mCherry concentration should exhibit a stronger depletion at mid-cell on average. This
1096 depletion was measured as the relative concentration difference between the HupA-mCherry peaks, which
1097 corresponded to the two lobes of the constricting nucleoid, and the trough at mid-cell, which corresponds
1098 to the point of nucleoid splitting. Similarly, the average polysome accumulation was measured as the RplA-
1099 GFP relative concentration difference between the mid-cell accumulation (peak) and the polysome depleted
1100 regions near the quarter cell positions, or at the centers of the segregating sister nucleoids (troughs). The
1101 same statistics were used to quantify the relative polysome accumulation at mid-cell and the relative
1102 nucleoid depletion in the same region between cell division cycles with different growth rates in the same
1103 nutrient condition (Figure 2C-E).
1104
1105 **Nucleoid segregation cycle tracking**
1106 In this work, the nucleoid segregation cycle was defined as the period from the end of a nucleoid splitting
1107 event (i.e., when a segregating nucleoid is segmented by local thresholding (custom Python function:
1108 *LoG_adaptive_image_filter.py*) as a separate object from its sister nucleoid) until the end of the splitting of

1109 the same nucleoid object (Figure 1 – figure supplement 2D), usually after cell division but sometimes in the
1110 same cell division cycle (Figure 1 – figure supplement 2A).
1111
1112 To track the nucleoid objects through the nucleoid segregation cycle from the mother cells to their
1113 daughters, we used the cell polarity, i.e., based on pole identity (Figure 1 – figure supplement 2B). The
1114 nucleoids of daughter cells that had opposite polarity to their mother cells were inherited from the new pole
1115 of the mother cells (groups 1 and -1 in Figure 1 – figure supplement 2B-C). The nucleoids in the daughter
1116 cells that had the same polarity as their mother cells were inherited from the old pole of the mother cells
1117 (groups 2 and -2 in Figure 1 – figure supplement 2B-C). During a complete nucleoid segregation cycle, the
1118 nucleoid was tracked from the quarter position of the mother cell to the center of its daughter cells (Figure
1119 1 – figure supplement 2C). This method is implemented in the *track_nucleoids* function, included in the
1120 *microfluidics_analysis_functions_ghv* Python script.
1121
1122 To quantify the polysome accumulation and nucleoid splitting during the nucleoid segregation cycle (Figure
1123 1E-F), we measured the RplA-GFP and HupA-mCherry concentration within the cell length region of 2.5
1124 pixels adjacent to the center of the tracked nucleoid object (5 pixels or 0.33 μm in total).
1125
1126 **Quantification and segmentation of polysomes and nucleoids segmentation in cells treated with**
1127 **cephalexin or cephalexin + A22**
1128 The polysome accumulations and nucleoids objects were also segmented in A22 and cephalexin-treated
1129 cells using an adaptive filter (custom Python function: *LoG_adaptive_image_filter.py*) on the masked cell
1130 fluorescence. The number of the detected polysome accumulations or nucleoid objects corresponds to the
1131 number of the segmented labels in the RplA-GFP or HupA-mCherry channel respectively. Similarly, the
1132 average polysome accumulation or nucleoid area corresponds to the average area of all segmented labels
1133 per channel. For a fair comparison between cells treated with A22 + cephalexin and cells treated with
1134 cephalexin alone, cells were randomly sampled without substitution from 12 cell area bins between 10 and
1135 13 μm^2 (bin width = 0.25 μm^2) such that the compared populations in Figure 7F had the same cell area
1136 distributions (same number of cells per cell area bin).
1137
1138 **Linear mixed-effects models to determine the relative contribution of polysome accumulation and**
1139 **cell elongation to the migration of the sister nucleoids**
1140 To estimate the relative contribution of the polysome accumulation at mid-cell and that of cell elongation to
1141 the migration of the separated sister nucleoids (first seen in Figure 1H), linear mixed-effects regressions
1142 were fitted to the scaled single cell data shown in Figure 1 – figure supplement 3B (*statsmodel* package in
1143 Python, *statsmodels.formula.api.mixedlm* function). One model was fitted for each relative time interval
1144 between the end of nucleoid splitting and cell division, describing the rate of distance increase between the
1145 separated sister nucleoids (σ, response variable) as a function of the polysome concentration increase rate

(ρ), the rate of cell elongation (λ), their interaction (ρλ), and noise (ε) (*statsmodels.formula.api.ols*) as follows:

$$\sigma = \beta_0 + \beta_1\rho + \beta_2\lambda + \beta_3(\rho\lambda) + \varepsilon \qquad \text{[eq. 3]}$$

The single cell data were scaled by subtracting the population mean and then dividing by the standard deviation prior to model fitting for each of the four relative time intervals (in Figure 1 – figure supplement 3B). The coefficients of the linear regression model (shown in Figure 1I) provide a measure of the relative effect of the independent variables on the dependent variable. The cell elongation (λ) had a statistically significant effect to the response variable (σ) Prob(>|Z|) < 10^{-9}) across all relative time intervals. The polysome accumulation coefficients (ρ) had a statistically significant effect to the response variable (σ) (Prob(>|Z|) < 10^{-14}) for the first three relative time intervals (0-25%, 25-50% and 50-75%) and a marginally significant one Prob(>|Z|) = 0.02) for the last quartile (75-100%). The interaction term (ρλ) had a marginally significant effect (Prob(>|Z|) = 0.002) for the first quartile (0-25%) yet with a very small coefficient of 0.06 and did not present any significance (Prob(>|Z|) > 0.05) for the remaining time intervals (25-50%, 50-75% and 75-100%). Hence, it is not shown in Figure 1I. The most significant effect on the migration of the sister nucleoids (σ) was presented by the rate of polysome accumulation at mid-cell (ρ), 0-25% from the end of nucleoid splitting to cell division, with a coefficient of 0.46 and Prob(>|Z|) < 10^{-84}.

Calculation of rates

The rates of the polysome accumulation ($\frac{\Delta RplA_{mid-nuc}\ conc.}{\Delta T}$) or nucleoid depletion ($\frac{\Delta HupA_{mid-nuc}\ conc.}{\Delta T}$) in the middle of the nucleoid (2.5 pixels adjacent the nucleoid center) (Figure 1F), correspond to the slope of a linear regression (Python fitting function: *numpy.polyfit*) fitted to the change of the mid-nucleoid RplA-GFP or HupA-mCherry concentration over time, 40-90% into the nucleoid segregation cycle (as in Figure 1E). This nucleoid cycle interval corresponds to the average time from the initiation of nucleoid splitting to just before its completion. Choosing the appropriate range to correlate the two statistics was important since polysomes appeared to accumulate in the middle of the nucleoid before the onset of nucleoid splitting (Figures 1E and Figure 1 – figure supplement 4D).

The rate of RplA-GFP concentration increase at mid-cell ($\frac{\Delta RplA_{mid-cell}\ conc.}{\Delta T}$) was calculated (Figure 1H) within a region covering 10% of the total cell length at the cell center. The same results were obtained when the rates were calculated within a cell region covering 2.5 pixels adjacent to the cell center. The rate of nucleoid migration ($\frac{\Delta Distance_{nuc}}{\Delta T}$) corresponds to the slope of a linear regression that describes the natural log-transformed distance increase between the separated sister nucleoids over time (Figure 1H). Similarly, the rate of cell elongation ($\frac{\Delta Length_{cell}}{\Delta T}$) was calculated considering the natural log-transformed cell length increase over time (Figure 1H). The rate of RplA-GFP concentration increase at mid-cell ($\frac{\Delta RplA_{mid-cell}\ conc.}{\Delta T}$),

the rate of nucleoid migration ($\frac{\Delta Distance_{nuc}}{\Delta T}$), and the rate of cell elongation ($\frac{\Delta Length_{cell}}{\Delta T}$) were calculated within four relative time intervals from the end of nucleoid splitting to cell division (Figure 1G and Figure 1 – figure supplement 3B). Only single nucleoid migration intervals with more than four timepoints were considered to ensure a reliable fitting. The small fraction (~8%) of cells that were born with two separately detected nucleoid objects, which indicates that the end of nucleoid splitting occurred in the previous cell division cycle, were removed from the analysis. The cell division cycles with a negative cell elongation rate (<1%) were also excluded from the analysis.

Reaction-diffusion model

Our theoretical model is an extension of previous work (Miangolarra et al., 2021), which showed that steric effects between the DNA and the transcription-translation machinery (including polysomes) are sufficient to drive nucleoid segregation. To simply describe these interactions, we employed the Flory-Huggins theory for regular solutions (Flory, 1942; Huggins, 1941) and modeled the non-dimensionalized free-energy density f as a function of the local volume fractions of the nucleoid (n) and polysomes (p):

$$f(n,p) = \frac{p}{v_p}\ln p + \frac{n}{v_n}\ln n + (1-p-n)\ln(1-p-n) + \chi_p p(1-p-n) + \chi_n n(1-p-n) + \chi_{np} np - \kappa_p \nabla p \nabla(1-p-n) - \kappa_n \nabla n \nabla(1-p-n) - \kappa_{np}\nabla n \nabla p \,. \qquad \text{[eq. 4]}$$

Here, $(1-n-p)$ is the volume fraction of the cytoplasm not occupied by nucleoid or polysomes, whereas v_n and v_p are proportional to the molecular volumes of the elementary translational degrees of freedom (i.e., of the nucleoid element and single polysome, respectively). χ_p, χ_n and χ_{np} are the Flory-Huggins interaction parameters, and κ_p, κ_n and κ_{np} are the interfacial tensions. We take $\kappa_{ij} = \lambda^2\chi_{ij}$, with λ being a characteristic interface width.

The time evolution of the volume fractions is described by a combination of Cahn-Hilliard theory (Cahn and Hilliard, 1958) and the reactions kinetics of the polysomes. We assume that polysomes are produced inside the nucleoid at a constant rate k_1 and degraded uniformly along the cell at a rate k_{-1}:

$$\frac{\partial p}{\partial t} = \nabla\left(M_p \nabla \mu_p\right) + k_1 n - k_{-1} p \,, \qquad \text{[eq. 5]}$$

$$\frac{\partial n}{\partial t} = \nabla(M_n \nabla \mu_n), \qquad \text{[eq. 6]}$$

where $\mu_p = \frac{\delta F}{\delta p}$ and $\mu_n = \frac{\delta F}{\delta n}$ are the local chemical potentials of polysomes and nucleoid elements respectively, with $F = \int f[n(x), p(x)]dx$ representing the total free energy. $M_p = v_p D_p p$ and $M_n = v_n D_n n$ are the mobility coefficients of the polysomes and the nucleoid, respectively, which depend on the diffusion

coefficients of the polysomes (D_p) and the nucleoid (D_n). This recovers the Fick law of diffusion in the noninteracting limit.

Since *E. coli* grows by elongation while maintaining its cylindrical shape and cell width, we reduce the problem to one dimension, with x representing the position along the long axis of the cell. We assume that the cell length grows exponentially such that the length at time t is $L(t) = L(0)e^{\gamma t}$, with γ being the growth rate and $L(0)$ the initial cell length at birth. Exponential growth dilutes the existing polysomes with rate γ. On the other hand, we assume that the nucleoid is not diluted since DNA replication occurs continuously, and the nucleoid length is known to grow in proportion to cell length (Gray et al., 2019). Letting $\tilde{x} = x/L(t)$ be the relative position along the cell's long axis, the time evolution is given by:

$$\frac{\partial p}{\partial t} = \partial_{\tilde{x}}\left(\widetilde{M}_p \partial_{\tilde{x}} \mu_p\right) + k_1 n - (k_{-1} + \gamma)p, \qquad \text{[eq. 7]}$$

$$\frac{\partial n}{\partial t} = \partial_{\tilde{x}}\left(\widetilde{M}_n \partial_{\tilde{x}} \mu_n\right), \qquad \text{[eq. 8]}$$

where $\partial_{\tilde{x}} = \frac{\partial}{\partial \tilde{x}} = L(t)\frac{\partial}{\partial x}$, and $\widetilde{M}_{n,p} = M_{n,p}L(t)^{-2}$. The chemical potentials are:

$$\mu_p = v_p^{-1} \ln p - \ln(1 - p - n) + \chi_p(1 - 2p - n) + \left(\chi_{np} - \chi_n\right)n$$
$$-\chi_p \tilde{\lambda}^2 \partial_{\tilde{x}}^2 (2p + n) + \left(\chi_{np} - \chi_n\right)\tilde{\lambda}^2 \partial_{\tilde{x}}^2 n, \qquad \text{[eq. 9]}$$

$$\mu_n = v_n^{-1} \ln n - \ln(1 - p - n) + \chi_n(1 - 2n - p) + \left(\chi_{np} - \chi_p\right)p$$
$$-\chi_n \tilde{\lambda}^2 \partial_{\tilde{x}}^2 (2n + p) + \left(\chi_{np} - \chi_p\right)\tilde{\lambda}^2 \partial_{\tilde{x}}^2 p, \qquad \text{[eq. 10]}$$

where $\tilde{\lambda} = \lambda/L(t)$.

We take the non-dimensionalized Flory-Huggins interaction parameters to be $\chi_p = 0.2$, $\chi_n = 0.4$ and $\chi_{np} = 1.2$. The χ_{np} parameter captures the steric repulsion between the nucleoid and the polysomes (Miangolarra et al., 2021). The diffusion coefficient of the polysome was set to $D_p = 0.015 \mu m^2/s$, which lies within the same order of magnitude as was previously measured by single-molecule tracking (Bakshi et al., 2012). Different diffusion coefficients were tested for the nucleoid ($D_n = 0.0003, 0.0005, 0.001 \text{ or } 0.005\ \mu\text{m}^2/\text{s}$) to capture different levels of nucleoid stiffness and hence response time to the local changes in polysome concentration. The polysome degradation rate was set to $k_{-1} = 0.003\text{s}^{-1}$, which corresponds to a half-life of around 5 min (Bernstein et al., 2004). We take the polysome production rate to be $k_1 = k_{1,0}\left(1 + \frac{\gamma}{k_{-1}}\right)$, with $k_{1,0} = 0.002\text{s}^{-1}$, to match the observation that the nucleoid length is proportional to cell length (Gray et al., 2019). The initial cell length $L(0)$ matched the cell length at birth, which has been previously shown to increase exponentially with the growth rate (Govers et al., 2024). Hence, each of the simulated growth

rates ($\gamma = 0.25, 0.4, 0.55, 0.7, 0.85 \text{ or } 1\ \mathrm{h}^{-1}$) was matched to a cell length at birth (Figure 4 – figure supplement 1A) by fitting a linear regression ($L(0) = l_0 e^{\gamma/\gamma_0}$, with fitted parameters $l_0 = 1.61\mu\mathrm{m}$ and $\gamma_0 = 1.84\mathrm{h}^{-1}$) to the experimental data (Govers et al., 2024). Other parameters are chosen as follows: $\lambda = 0.03\mu\mathrm{m}$, $v_n = 10$, $v_p = 5$.

The dynamic equations (eqs. 7-8) were solved numerically in a fixed 1D domain $\tilde{x} \in (0,1)$, with no-flux boundary conditions. Space is discretized into $N = 128$ grid points, and time is discretized to steps of Δt. Time stepping was implemented with an implicit-explicit scheme as previously demonstrated (Mao et al., 2020, 2019). The simulations were initialized from the (symmetric) steady-state solution of the system at the initial cell length $L(0)$ (Figure 4A, dashed curves in Figure 4D, and Movie S3), or using the (asymmetric) macromolecular distribution of the predivisional cell of the former simulation as the initial condition (Figure 4C, solid curves in Figure 4D) which allowed us to capture cell polarity (new versus old pole). The cell length $L(t)$ was updated and recorded at each time step during the simulation. The nucleoid splitting time (shown in Figure 4C) was determined by thresholding the relative decrease of the nucleoid concentration at the cell center (as shown in in Figure 4 – figure supplement 1B). The code for the model is available at https://github.com/qiweiyuu/polysome.

Polysome and nucleoid analysis based on fitted Gaussian functions

Quantification of polysome and nucleoid asymmetries within cells along the cell division cycle was achieved by fitting Gaussian functions (Python least squares optimization: *scipy.optimize.curve_fit*) to the RplA-GFP or the HupA-mCherry intensity profiles of cells growing in M9gluCAAT in the microfluidic device. Three Gaussian functions were fitted to the polysome signal concentration early in the cell division cycle. Two of them captured the nucleoid-excluded polysomes accumulating at the poles and the third captured the polysome accumulation in the middle of nucleoid (Figure 3 – figure supplement 1A-B):

$$Poly(l) = A_{old} \exp\left(-\frac{1}{2}\left(\frac{l_{old}-l}{\sigma_{old}}\right)^2\right) + A_{mid} \exp\left(-\frac{1}{2}\left(\frac{l_{mid}-l}{\sigma_{mid}}\right)^2\right) + A_{new} \exp\left(-\frac{1}{2}\left(\frac{l_{new}-l}{\sigma_{new}}\right)^2\right) \quad \text{[eq. 11]},$$

where A_{old}, A_{new} and A_{mid} are the amplitudes, l_{old}, l_{new} and l_{mid} are the means, and σ_{old}, σ_{new} and σ_{mid} are the standard deviations of the respective fitted functions along the relative cell length (l).

Two Gaussian functions were fitted to the concentration of constricting nucleoids (Figure 3 – figure supplement 1A-B):

$$Nuc(l) = A_{old} \exp\left(-\frac{1}{2}\left(\frac{l_{old}-l}{\sigma_{old}}\right)^2\right) + A_{new} \exp\left(-\frac{1}{2}\left(\frac{l_{new}-l}{\sigma_{new}}\right)^2\right) \quad \text{[eq. 12]}$$

All Gaussian functions were fitted over the cell background fluorescence, which corresponds to the baseline fluorescence within the masked cell boundaries and along the relative cell length coordinates from the old pole (-1) via the cell center (0) to the new pole (1). The Gaussian functions were fitted either to single newborn cells (0-2.5% into the cell division cycle) as shown in Figure 3 – figure supplement 1A-B and as

applied in Figures 3A and 3E, or to the less noisy average intensity profile of the segmented cells within the 0-10% range of their cell division cycle, as shown in Figure 3 – figure supplement 1C-D and used in Figures 3B and 3F. The areas of the Gaussian functions fitted to the polysomes (used in Figure 3A-B) were estimated using the function:

$$Area = A\,\sigma\,\sqrt{2\pi} \qquad \text{[eq. 13]},$$

where *A* is the amplitude and *σ is* the standard deviation.

The Gaussian areas were used to quantify the polysome asymmetries between the poles:

$$Poly_{asym} = log_{10}\left(\frac{Area_{new}}{Area_{old}}\right) \qquad \text{[eq. 14]},$$

where $Area_{new}$ and $Area_{old}$ are the areas of the fitted Gaussians to the nucleoid-excluded polysomes accumulating in the new and the old pole, respectively. The statistic in eq. 14 corresponds to the x-axis in Figure 3B. It is a positive value when the new pole contains more polysomes than the old one, and a negative value when the old pole contains more polysomes than the new one.

The nucleoid Gaussian statistics were used to quantify the nucleoid position asymmetry defined as:

$$Nuc_{pos} = \frac{l_{new} + l_{old}}{2}\,\frac{l_{cell}}{2} \qquad \text{[eq. 15]},$$

and the nucleoid compaction asymmetry was calculated as:

$$Nuc_{comp} = \frac{A_{new}}{A_{old}} \qquad \text{[eq. 16]},$$

where l_{old} and l_{new} are the means of the nucleoid Gaussians in relative cell coordinates (as in eq. 12) and l_{cell} is the cell length in µm. The nucleoid position was first estimated in relative cell coordinates from the old pole (-1) via the cell center (0) to the new pole (1), and then multiplied by half the cell length to convert to absolute cell length units. A_{old} and A_{new} are the amplitudes of the fitted nucleoid Gaussians (as in eq. 12) in arbitrary fluorescence units. The nucleoid position corresponds to the mid-point between the two Gaussian means (eq. 15) and is a positive number when the nucleoid is shifted toward the new pole and a negative number when it is positioned closer to the old pole (y-axis in Figure 3B).

The nucleoid compaction asymmetry was calculated as the relative nucleoid Gaussian amplitude (eq. 16). It had a positive value greater than 1 when the nucleoid concentration was higher toward the new pole and had a positive value smaller than 1 if the nucleoid was more concentrated toward the old pole (y-axis in Figure 3F).

To determine which polysome Gaussian statistics and related asymmetries may contribute to nucleoid compaction asymmetry (eq. 16), a linear mixed-effects model was used (*statsmodel* package in Python, *statsmodels.formula.api.mixedlm* function). The polysome Gaussian statistics were used as independent variables and the nucleoid compaction asymmetry as a dependent variable:

$$Nuc_{comp} = \beta_0 + \beta_1 l_{old} + \beta_2 l_{mid} + \beta_3 l_{new} + \beta_4 \sigma_{old} + \beta_5 \sigma_{mid} + \beta_6 \sigma_{new} + \beta_7 A_{old} + \beta_8 A_{mid} + \beta_9 A_{new} + \varepsilon \quad \text{[eq. 17]},$$

where β_0 is the constant (intercept), β_n *(n=1,2…,9)* are the coefficients for each of the polysome Gaussian statistics (same as in eq. 4 and plotted in Figure 3 – figure supplement 1E-F), and ε is the error. The entire dataset was treated as a single group. Before fitting the linear mixed-effects model, all data were normalized by subtracting the average and dividing the resulting value by their standard deviation (Figure 3 – figure supplement 1F). The relative cell length positions of the polysomes at the old pole (l_{old}) and in the middle of the nucleoid (l_{mid}) were found to significantly influence the asymmetric nucleoid compaction (Figure 3 – figure supplement 1G). We reasoned that the available spaces between the polysome positions (Figure 3 – figure supplement 1E) may influence the compaction of the nucleoid and devised a new statistic that compares the available polysome-free space toward the new pole to that of toward the old pole:

$$Poly_{space} = \frac{l_{new} - l_{mid}}{l_{mid} - l_{old}} \quad \text{[eq. 18]},$$

where l_{new}, l_{mid} and l_{old} are the polysome Gaussian means (as in eq. 11), which represent the positions of the polysomes at the new pole, mid-cell region, and old pole, respectively, expressed as relative cell coordinates from the old pole (-1) via the cell center (0) to the new pole (1). The fraction above (eq. 18) has a value greater than 1 when the polysome-free space is greater toward the new pole and a value smaller than 1 when the polysome-free space is greater toward the old pole (x-axis in Figure 3F).

Linear regressions

Two types of linear regressions were used in this work. In Figure 2B, a first-degree polynomial was fitted using the ordinary least squares method and the numpy library in Python (*numpy.polyfit*), always using the *x*-axis as the independent variable and the *y*-axis as the dependent variable. In Figures 1F and 3B, a principal component regression was fitted using the scikit-learn library in Python (*sklearn.decomposition.PCA*). A principal component analysis was first applied on the two-dimensional z-transformed data to find the linear regressor that explained most of the variance (the first principal component). This linear regressor was then rescaled to the original 2D plane. The principal component regression eliminates the dependent variable bias associated with a traditional univariate fit. This bias is introduced when calculating the prediction error (sum of squares) only along the dependent variable axis during the least squares optimization. The elimination of this univariate bias is particularly important for the

fitted regressions in Figures 1F and 3B since their parameters were used to estimate the rate of nucleoid splitting in the absence of polysome accumulation in the middle (y-intercept in Figure 1F), the position of the nucleoid with equal polysomes at the poles (y-intercept in Figure 3B), or the polar asymmetry required for a centered nucleoid (x-intercept in Figure 3B).

Kernel density estimations

One-dimensional (Figures 3A, E, and Figure 1- figure supplement 2C) or two-dimensional (Figures 1F, 1H, Figure 1 – figure supplement 3A-B, and Figure 3 – figure supplement 1F) Gaussian kernel density estimations were fitted using the *scipy.stats.gaussian_kde* method. The bandwidth was determined using Scott's rule (Scott, 1992).

Correlation coefficient calculations

All Spearman correlation coefficients (referred to as Spearman ρ) were estimated using the *scipy.stats* Python library and the *spearmanr* function. Only those Spearman correlation coefficients with a p-value below 0.05 are shown. Otherwise, the correlation is annotated as not-significant (NS) (as in Figure 1 – figure supplement 3B).

ADDITIONAL RESOURCES

This study did not generate any additional resources.

ACKNOWLEDGMENTS

We are grateful to Dr. A Janakiraman (City College of New York) for the pER12 (pBAD322A-gfp-μNS) plasmid, Dr K. Prather (Massachusetts Institute of Technology) for the MG1655 (DE3) strain, and the members of the Jacobs-Wagner laboratory for fruitful discussions and critical reading of the manuscript. This work was part of the research program Rubicon Science 2018-1 with project number 019.181EN.018, which was financed by the Netherlands Organization for Scientific Research (NWO). C.J.W. is an investigator of Howard Hughes Medical Institute.

AUTHOR CONTRIBUTIONS

Conceptualization, A.P. and C.J.-W.; methodology, A.P.; software, A.P. and Q.Y.; formal analysis, A.P.; investigation, A.P., Q.Y, and S.K.G.; resources, A.P., Q.Y., and W.-H.L.; data curation, A.P.; writing – original draft, A.P. and C.J.-W.; writing – review and editing, A.P., C.J.-W , N. W., Q.Y., S.K.G., and W.-H.L; visualization, A.P. and C.J.-W.; supervision, N.W. and C.J.-W.; project administration, C.J.-W.; funding acquisition, A.P., N.W. and C.J.-W.

DECLARATION OF INTERESTS

The authors declare no competing interests.

1407 **REFERENCES**

1408 Azam, T.A., Hiraga, S., Ishihama, A., 2000. Two types of localization of the DNA-binding proteins
1409 within the Escherichia coli nucleoid: Intracellular localization of E. coli DNA-binding
1410 proteins. Genes Cells 5, 613–626. https://doi.org/10.1046/j.1365-2443.2000.00350.x
1411 Bakshi, S., Choi, H., Mondal, J., Weisshaar, J.C., 2014. Time-dependent effects of transcription-
1412 and translation-halting drugs on the spatial distributions of the *E scherichia coli*
1413 chromosome and ribosomes: Time-dependent drug effects on *E. coli* chromosome
1414 spatial distribution. Mol. Microbiol. 94, 871–887. https://doi.org/10.1111/mmi.12805
1415 Bakshi, S., Choi, H., Weisshaar, J.C., 2015. The spatial biology of transcription and translation in
1416 rapidly growing Escherichia coli. Front. Microbiol. 6.
1417 https://doi.org/10.3389/fmicb.2015.00636
1418 Bakshi, S., Siryaporn, A., Goulian, M., Weisshaar, J.C., 2012. Superresolution imaging of
1419 ribosomes and RNA polymerase in live Escherichia coli cells: Superresolution imaging of
1420 ribosome and RNAP. Mol. Microbiol. 85, 21–38. https://doi.org/10.1111/j.1365-
1421 2958.2012.08081.x
1422 Balakrishnan, R., Mori, M., Segota, I., Zhang, Z., Aebersold, R., Ludwig, C., Hwa, T., 2022.
1423 Principles of gene regulation quantitatively connect DNA to RNA and proteins in
1424 bacteria. Science 378, eabk2066. https://doi.org/10.1126/science.abk2066
1425 Bartosik, A.A., Mierzejewska, J., Thomas, C.M., Jagura-Burdzy, G., 2009. ParB deficiency in
1426 Pseudomonas aeruginosa destabilizes the partner protein ParA and affects a variety of
1427 physiological parameters. Microbiology 155, 1080–1092.
1428 https://doi.org/10.1099/mic.0.024661-0
1429 Bates, D., Kleckner, N., 2005. Chromosome and Replisome Dynamics in E. coli: Loss of Sister
1430 Cohesion Triggers Global Chromosome Movement and Mediates Chromosome
1431 Segregation. Cell 121, 899–911. https://doi.org/10.1016/j.cell.2005.04.013
1432 Bean, G.J., Flickinger, S.T., Westler, W.M., McCully, M.E., Sept, D., Weibel, D.B., Amann, K.J.,
1433 2009. A22 Disrupts the Bacterial Actin Cytoskeleton by Directly Binding and Inducing a
1434 Low-Affinity State in MreB. Biochemistry 48, 4852–4857.
1435 https://doi.org/10.1021/bi900014d
1436 Belliveau, N.M., Chure, G., Hueschen, C.L., Garcia, H.G., Kondev, J., Fisher, D.S., Theriot, J.A.,
1437 Phillips, R., 2021. Fundamental limits on the rate of bacterial growth and their influence
1438 on proteomic composition. Cell Syst. 12, 924-944.e2.
1439 https://doi.org/10.1016/j.cels.2021.06.002
1440 Bernstein, J.A., Lin, P.-H., Cohen, S.N., Lin-Chao, S., 2004. Global analysis of *Escherichia coli* RNA
1441 degradosome function using DNA microarrays. Proc. Natl. Acad. Sci. 101, 2758–2763.
1442 https://doi.org/10.1073/pnas.0308747101
1443 Blundell, M.R., Wild, D.G., 1971. Altered ribosomes after inhibition of *Escherichia coli* by
1444 rifampicin. Biochem. J. 121, 391–398. https://doi.org/10.1042/bj1210391
1445 Brandt, F., Etchells, S.A., Ortiz, J.O., Elcock, A.H., Hartl, F.U., Baumeister, W., 2009. The Native
1446 3D Organization of Bacterial Polysomes. Cell 136, 261–271.
1447 https://doi.org/10.1016/j.cell.2008.11.016
1448 Broering, T.J., Arnold, M.M., Miller, C.L., Hurt, J.A., Joyce, P.L., Nibert, M.L., 2005. Carboxyl-
1449 Proximal Regions of Reovirus Nonstructural Protein µNS Necessary and Sufficient for

1450 Forming Factory-Like Inclusions. J. Virol. 79, 6194–6206.
1451 https://doi.org/10.1128/JVI.79.10.6194-6206.2005
1452 Broering, T.J., Parker, J.S.L., Joyce, P.L., Kim, J., Nibert, M.L., 2002. Mammalian Reovirus
1453 Nonstructural Protein μNS Forms Large Inclusions and Colocalizes with Reovirus
1454 Microtubule-Associated Protein μ2 in Transfected Cells. J. Virol. 76, 8285–8297.
1455 https://doi.org/10.1128/JVI.76.16.8285-8297.2002
1456 Bryksin, A.V., Matsumura, I., 2010. Overlap extension PCR cloning: a simple and reliable way to
1457 create recombinant plasmids. BioTechniques 48, 463–465.
1458 https://doi.org/10.2144/000113418
1459 Cahn, J.W., Hilliard, J.E., 1958. Free Energy of a Nonuniform System. I. Interfacial Free Energy. J.
1460 Chem. Phys. 28, 258–267. https://doi.org/10.1063/1.1744102
1461 Campbell, E.A., Korzheva, N., Mustaev, A., Murakami, K., Nair, S., Goldfarb, A., Darst, S.A., 2001.
1462 Structural Mechanism for Rifampicin Inhibition of Bacterial RNA Polymerase. Cell 104,
1463 901–912. https://doi.org/10.1016/S0092-8674(01)00286-0
1464 Campos, M., Govers, S.K., Irnov, I., Dobihal, G.S., Cornet, F., Jacobs-Wagner, C., 2018.
1465 Genomewide phenotypic analysis of growth, cell morphogenesis, and cell cycle events in
1466 *Escherichia coli*. Mol. Syst. Biol. 14, e7573. https://doi.org/10.15252/msb.20177573
1467 Campos, M., Surovtsev, I.V., Kato, S., Paintdakhi, A., Beltran, B., Ebmeier, S.E., Jacobs-Wagner,
1468 C., 2014. A constant size extension drives bacterial cell size homeostasis. Cell 159, 1433–
1469 1446. https://doi.org/10.1016/j.cell.2014.11.022
1470 Cass, J.A., Kuwada, N.J., Traxler, B., Wiggins, P.A., 2016. Escherichia coli Chromosomal Loci
1471 Segregate from Midcell with Universal Dynamics. Biophys. J. 110, 2597–2609.
1472 https://doi.org/10.1016/j.bpj.2016.04.046
1473 Castellana, M., Hsin-Jung Li, S., Wingreen, N.S., 2016. Spatial organization of bacterial
1474 transcription and translation. Proc. Natl. Acad. Sci. 113, 9286–9291.
1475 https://doi.org/10.1073/pnas.1604995113
1476 Chai, Q., Singh, B., Peisker, K., Metzendorf, N., Ge, X., Dasgupta, S., Sanyal, S., 2014.
1477 Organization of Ribosomes and Nucleoids in Escherichia coli Cells during Growth and in
1478 Quiescence. J. Biol. Chem. 289, 11342–11352.
1479 https://doi.org/10.1074/jbc.M114.557348
1480 Chao, L., Chen, C.K., Shi, C., Rang, C.U., 2023. Spatial and temporal distribution of ribosomes in
1481 single cells reveals aging differences between old and new daughters of *Escherichia coli*
1482 (preprint). Evolutionary Biology. https://doi.org/10.1101/2023.06.21.545935
1483 Charaka, V.K., Misra, H.S., 2012. Functional Characterization of the Role of the Chromosome I
1484 Partitioning System in Genome Segregation in Deinococcus radiodurans. J. Bacteriol.
1485 194, 5739–5748. https://doi.org/10.1128/JB.00610-12
1486 Cherepanov, P.P., Wackernagel, W., 1995. Gene disruption in Escherichia coli: TcR and KmR
1487 cassettes with the option of Flp-catalyzed excision of the antibiotic-resistance
1488 determinant. Gene 158, 9–14. https://doi.org/10.1016/0378-1119(95)00193-A
1489 Chure, G., Cremer, J., 2023. An optimal regulation of fluxes dictates microbial growth in and out
1490 of steady state. eLife 12, e84878. https://doi.org/10.7554/eLife.84878
1491 Cooper, S., Hsieh, M.L., 1988. The Rate and Topography of Cell Wall Synthesis during the
1492 Division Cycle of Escherichia coli Using N-Acetylglucosamine as a Peptidoglycan Label.
1493 Microbiology 134, 1717–1721. https://doi.org/10.1099/00221287-134-6-1717

1494 Coquel, A.-S., Jacob, J.-P., Primet, M., Demarez, A., Dimiccoli, M., Julou, T., Moisan, L., Lindner,
1495 A.B., Berry, H., 2013. Localization of Protein Aggregation in Escherichia coli Is Governed
1496 by Diffusion and Nucleoid Macromolecular Crowding Effect. PLoS Comput. Biol. 9,
1497 e1003038. https://doi.org/10.1371/journal.pcbi.1003038
1498 Cutler, K.J., Stringer, C., Lo, T.W., Rappez, L., Stroustrup, N., Brook Peterson, S., Wiggins, P.A.,
1499 Mougous, J.D., 2022. Omnipose: a high-precision morphology-independent solution for
1500 bacterial cell segmentation. Nat. Methods 19, 1438–1448.
1501 https://doi.org/10.1038/s41592-022-01639-4
1502 Dai, X., Zhu, M., Warren, M., Balakrishnan, R., Patsalo, V., Okano, H., Williamson, J.R., Fredrick,
1503 K., Wang, Y.-P., Hwa, T., 2017. Reduction of translating ribosomes enables Escherichia
1504 coli to maintain elongation rates during slow growth. Nat. Microbiol. 2, 16231.
1505 https://doi.org/10.1038/nmicrobiol.2016.231
1506 Danilova, O., Reyes-Lamothe, R., Pinskaya, M., Sherratt, D., Possoz, C., 2007. MukB colocalizes
1507 with the oriC region and is required for organization of the two Escherichia coli
1508 chromosome arms into separate cell halves. Mol. Microbiol. 65, 1485–1492.
1509 https://doi.org/10.1111/j.1365-2958.2007.05881.x
1510 Datsenko, K.A., Wanner, B.L., 2000. One-step inactivation of chromosomal genes in *Escherichia*
1511 *coli* K-12 using PCR products. Proc. Natl. Acad. Sci. 97, 6640–6645.
1512 https://doi.org/10.1073/pnas.120163297
1513 Davis, J.H., Rubin, A.J., Sauer, R.T., 2011. Design, construction and characterization of a set of
1514 insulated bacterial promoters. Nucleic Acids Res. 39, 1131–1141.
1515 https://doi.org/10.1093/nar/gkq810
1516 Donczew, M., Mackiewicz, P., Wróbel, A., Flärdh, K., Zakrzewska-Czerwińska, J., Jakimowicz, D.,
1517 2016. ParA and ParB coordinate chromosome segregation with cell elongation and
1518 division during *Streptomyces* sporulation. Open Biol. 6, 150263.
1519 https://doi.org/10.1098/rsob.150263
1520 Donovan, C., Schwaiger, A., Krämer, R., Bramkamp, M., 2010. Subcellular Localization and
1521 Characterization of the ParAB System from *Corynebacterium glutamicum*. J. Bacteriol.
1522 192, 3441–3451. https://doi.org/10.1128/JB.00214-10
1523 Dourado, H., Lercher, M.J., 2020. An analytical theory of balanced cellular growth. Nat.
1524 Commun. 11, 1226. https://doi.org/10.1038/s41467-020-14751-w
1525 Du, W.-L., Dubarry, N., Passot, F.M., Kamgoué, A., Murray, H., Lane, D., Pasta, F., 2016. Orderly
1526 Replication and Segregation of the Four Replicons of Burkholderia cenocepacia J2315.
1527 PLOS Genet. 12, e1006172. https://doi.org/10.1371/journal.pgen.1006172
1528 Dworkin, J., Losick, R., 2002. Does RNA polymerase help drive chromosome segregation in
1529 bacteria? Proc. Natl. Acad. Sci. 99, 14089–14094.
1530 https://doi.org/10.1073/pnas.182539899
1531 Dworsky, P., Schaechter, M., 1973. Effect of Rifampin on the Structure and Membrane
1532 Attachment of the Nucleoid of *Escherichia coli*. J. Bacteriol. 116, 1364–1374.
1533 https://doi.org/10.1128/jb.116.3.1364-1374.1973
1534 Figge, R.M., Easter, J., Gober, J.W., 2003. Productive interaction between the chromosome
1535 partitioning proteins, ParA and ParB, is required for the progression of the cell cycle in
1536 Caulobacter crescentus: Dominant-negative ParB alleles. Mol. Microbiol. 47, 1225–1237.
1537 https://doi.org/10.1046/j.1365-2958.2003.03367.x

1538 Fisher, J.K., Bourniquel, A., Witz, G., Weiner, B., Prentiss, M., Kleckner, N., 2013. Four-
1539 Dimensional Imaging of E. coli Nucleoid Organization and Dynamics in Living Cells. Cell
1540 153, 882–895. https://doi.org/10.1016/j.cell.2013.04.006
1541 Flory, P.J., 1942. Thermodynamics of High Polymer Solutions. J. Chem. Phys. 10, 51–61.
1542 https://doi.org/10.1063/1.1723621
1543 Forchhammer, J., Lindahl, L., 1971. Growth rate of polypeptide chains as a function of the cell
1544 growth rate in a mutant of Escherichia coli 15. J. Mol. Biol. 55, 563–568.
1545 https://doi.org/10.1016/0022-2836(71)90337-8
1546 Gibson, D.G., Young, L., Chuang, R.-Y., Venter, J.C., Hutchison, C.A., Smith, H.O., 2009.
1547 Enzymatic assembly of DNA molecules up to several hundred kilobases. Nat. Methods 6,
1548 343–345. https://doi.org/10.1038/nmeth.1318
1549 Gillies, Sean, van der Wel, Casper, Van den Bossche, Joris, Taves, Mike W., Arnott, Joshua,
1550 Ward, Brendan C., Others, 2023. Shapely. https://doi.org/10.5281/ZENODO.5597138
1551 Govers, S.K., Campos, M., Tyagi, B., Laloux, G., Jacobs-Wagner, C., 2024. Apparent simplicity and
1552 emergent robustness in the control of the Escherichia coli cell cycle. Cell Syst. 15, 19-
1553 36.e5. https://doi.org/10.1016/j.cels.2023.12.001
1554 Gray, A.N., Egan, A.J., Van'T Veer, I.L., Verheul, J., Colavin, A., Koumoutsi, A., Biboy, J., Altelaar,
1555 A.F.M., Damen, M.J., Huang, K.C., Simorre, J.-P., Breukink, E., Den Blaauwen, T., Typas,
1556 A., Gross, C.A., Vollmer, W., 2015. Coordination of peptidoglycan synthesis and outer
1557 membrane constriction during Escherichia coli cell division. eLife 4, e07118.
1558 https://doi.org/10.7554/eLife.07118
1559 Gray, W.T., Govers, S.K., Xiang, Y., Parry, B.R., Campos, M., Kim, S., Jacobs-Wagner, C., 2019.
1560 Nucleoid Size Scaling and Intracellular Organization of Translation across Bacteria. Cell
1561 177, 1632-1648.e20. https://doi.org/10.1016/j.cell.2019.05.017
1562 Guyer, M.S., Reed, R.R., Steitz, J.A., Low, K.B., 1981. Identification of a Sex-factor-affinity Site in
1563 E. coli as. Cold Spring Harb. Symp. Quant. Biol. 45, 135–140.
1564 https://doi.org/10.1101/SQB.1981.045.01.022
1565 Guzman, L.M., Belin, D., Carson, M.J., Beckwith, J., 1995. Tight regulation, modulation, and
1566 high-level expression by vectors containing the arabinose PBAD promoter. J. Bacteriol.
1567 177, 4121–4130. https://doi.org/10.1128/jb.177.14.4121-4130.1995
1568 Harju, J., Van Teeseling, M.C.F., Broedersz, C.P., 2024. Loop-extruders alter bacterial
1569 chromosome topology to direct entropic forces for segregation. Nat. Commun. 15, 4618.
1570 https://doi.org/10.1038/s41467-024-49039-w
1571 Harju, J., Van Teeseling, M.C.F., Broedersz, C.P., 2023. Loop-extruders alter bacterial
1572 chromosome topology to direct entropic forces for segregation (preprint). Biophysics.
1573 https://doi.org/10.1101/2023.06.30.547230
1574 Harris, C.R., Millman, K.J., Van Der Walt, S.J., Gommers, R., Virtanen, P., Cournapeau, D.,
1575 Wieser, E., Taylor, J., Berg, S., Smith, N.J., Kern, R., Picus, M., Hoyer, S., Van Kerkwijk,
1576 M.H., Brett, M., Haldane, A., Del Río, J.F., Wiebe, M., Peterson, P., Gérard-Marchant, P.,
1577 Sheppard, K., Reddy, T., Weckesser, W., Abbasi, H., Gohlke, C., Oliphant, T.E., 2020.
1578 Array programming with NumPy. Nature 585, 357–362.
1579 https://doi.org/10.1038/s41586-020-2649-2

1580 Hartmann, G., Honikel, K.O., Knüsel, F., Nüesch, J., 1967. The specific inhibition of the DNA-
1581 directed RNA synthesis by rifamycin. Biochim. Biophys. Acta BBA - Nucleic Acids Protein
1582 Synth. 145, 843–844. https://doi.org/10.1016/0005-2787(67)90147-5
1583 Hofmann, A., Mäkelä, J., Sherratt, D.J., Heermann, D., Murray, S.M., 2019. Self-organised
1584 segregation of bacterial chromosomal origins. eLife 8, e46564.
1585 https://doi.org/10.7554/eLife.46564
1586 Holmes, V.F., Cozzarelli, N.R., 2000. Closing the ring: Links between SMC proteins and
1587 chromosome partitioning, condensation, and supercoiling. Proc. Natl. Acad. Sci. 97,
1588 1322–1324. https://doi.org/10.1073/pnas.040576797
1589 Hsu, T.-M., Chang, Y.-R., 2019. High-Copy-Number Plasmid Segregation—Single-Molecule
1590 Dynamics in Single Cells. Biophys. J. 116, 772–780.
1591 https://doi.org/10.1016/j.bpj.2019.01.019
1592 Hu, X.-P., Dourado, H., Schubert, P., Lercher, M.J., 2020. The protein translation machinery is
1593 expressed for maximal efficiency in Escherichia coli. Nat. Commun. 11, 5260.
1594 https://doi.org/10.1038/s41467-020-18948-x
1595 Huggins, M.L., 1941. Solutions of Long Chain Compounds. J. Chem. Phys. 9, 440–440.
1596 https://doi.org/10.1063/1.1750930
1597 Hunter, J.D., 2007. Matplotlib: A 2D Graphics Environment. Comput. Sci. Eng. 9, 90–95.
1598 https://doi.org/10.1109/MCSE.2007.55
1599 Ireton, K., Gunther, N.W., Grossman, A.D., 1994. spo0J is required for normal chromosome
1600 segregation as well as the initiation of sporulation in Bacillus subtilis. J. Bacteriol. 176,
1601 5320–5329. https://doi.org/10.1128/jb.176.17.5320-5329.1994
1602 Iwai, N., Nagai, K., Wachi, M., 2002. Novel *S* -Benzylisothiourea Compound That Induces
1603 Spherical Cells in *Escherichia coli* Probably by Acting on a Rod-shape-determining
1604 Protein(s) Other Than Penicillin-binding Protein 2. Biosci. Biotechnol. Biochem. 66,
1605 2658–2662. https://doi.org/10.1271/bbb.66.2658
1606 Jacob, F., Brenner, S., Cuzin, F., 1963. On the Regulation of DNA Replication in Bacteria. Cold
1607 Spring Harb. Symp. Quant. Biol. 28, 329–348.
1608 https://doi.org/10.1101/SQB.1963.028.01.048
1609 Jakimowicz, D., Brzostek, A., Rumijowska-Galewicz, A., Żydek, P., Dołzbłasz, A., Smulczyk-
1610 Krawczyszyn, A., Zimniak, T., Wojtasz, Ł., Zawilak-Pawlik, A., Kois, A., Dziadek, J.,
1611 Zakrzewska-Czerwińska, J., 2007a. Characterization of the mycobacterial chromosome
1612 segregation protein ParB and identification of its target in Mycobacterium smegmatis.
1613 Microbiology 153, 4050–4060. https://doi.org/10.1099/mic.0.2007/011619-0
1614 Jakimowicz, D., Żydek, P., Kois, A., Zakrzewska-Czerwińska, J., Chater, K.F., 2007b. Alignment of
1615 multiple chromosomes along helical ParA scaffolding in sporulating *Streptomyces*
1616 hyphae. Mol. Microbiol. 65, 625–641. https://doi.org/10.1111/j.1365-
1617 2958.2007.05815.x
1618 Jalal, A.S.B., Le, T.B.K., 2020. Bacterial chromosome segregation by the ParABS system. Open
1619 Biol. 10, 200097. https://doi.org/10.1098/rsob.200097
1620 Jecz, P., Bartosik, A.A., Glabski, K., Jagura-Burdzy, G., 2015. A Single parS Sequence from the
1621 Cluster of Four Sites Closest to oriC Is Necessary and Sufficient for Proper Chromosome
1622 Segregation in Pseudomonas aeruginosa. PLOS ONE 10, e0120867.
1623 https://doi.org/10.1371/journal.pone.0120867

1624 Jensen, K.F., 1993. The Escherichia coli K-12 “wild types” W3110 and MG1655 have an rph
1625 frameshift mutation that leads to pyrimidine starvation due to low pyrE expression
1626 levels. J. Bacteriol. 175, 3401–3407. https://doi.org/10.1128/jb.175.11.3401-3407.1993
1627 Jun, S., Mulder, B., 2006. Entropy-driven spatial organization of highly confined polymers:
1628 Lessons for the bacterial chromosome. Proc. Natl. Acad. Sci. 103, 12388–12393.
1629 https://doi.org/10.1073/pnas.0605305103
1630 Jun, S., Wright, A., 2010. Entropy as the driver of chromosome segregation. Nat. Rev. Microbiol.
1631 8, 600–607. https://doi.org/10.1038/nrmicro2391
1632 Kadoya, R., Baek, J.H., Sarker, A., Chattoraj, D.K., 2011. Participation of Chromosome
1633 Segregation Protein ParAI of *Vibrio cholerae* in Chromosome Replication. J. Bacteriol.
1634 193, 1504–1514. https://doi.org/10.1128/JB.01067-10
1635 Kawalek, A., Wawrzyniak, P., Bartosik, A.A., Jagura-Burdzy, G., 2020. Rules and Exceptions: The
1636 Role of Chromosomal ParB in DNA Segregation and Other Cellular Processes.
1637 Microorganisms 8, 105. https://doi.org/10.3390/microorganisms8010105
1638 Kim, H.-J., Calcutt, M.J., Schmidt, F.J., Chater, K.F., 2000. Partitioning of the Linear Chromosome
1639 during Sporulation of *Streptomyces coelicolor* A3(2) Involves an *oriC* -Linked *parAB*
1640 Locus. J. Bacteriol. 182, 1313–1320. https://doi.org/10.1128/JB.182.5.1313-1320.2000
1641 Kjos, M., Veening, J.-W., 2014. Tracking of chromosome dynamics in live *S treptococcus*
1642 *pneumoniae* reveals that transcription promotes chromosome segregation:
1643 Transcription promotes chromosome segregation. Mol. Microbiol. 91, 1088–1105.
1644 https://doi.org/10.1111/mmi.12517
1645 Koch, A.L., Gross, G.H., 1979. Growth Conditions and Rifampin Susceptibility. Antimicrob.
1646 Agents Chemother. 15, 220–228. https://doi.org/10.1128/AAC.15.2.220
1647 Koleva, K.Z., Hellweger, F.L., 2015. From protein damage to cell aging to population fitness in E.
1648 coli: Insights from a multi-level agent-based model. Ecol. Model. 301, 62–71.
1649 https://doi.org/10.1016/j.ecolmodel.2015.01.024
1650 Kuwada, N.J., Cheveralls, K.C., Traxler, B., Wiggins, P.A., 2013. Mapping the driving forces of
1651 chromosome structure and segregation in Escherichia coli. Nucleic Acids Res. 41, 7370–
1652 7377. https://doi.org/10.1093/nar/gkt468
1653 Lagage, V., Boccard, F., Vallet-Gely, I., 2016. Regional Control of Chromosome Segregation in
1654 Pseudomonas aeruginosa. PLOS Genet. 12, e1006428.
1655 https://doi.org/10.1371/journal.pgen.1006428
1656 Łapińska, U., Glover, G., Capilla-Lasheras, P., Young, A.J., Pagliara, S., 2019. Bacterial ageing in
1657 the absence of external stressors. Philos. Trans. R. Soc. B Biol. Sci. 374, 20180442.
1658 https://doi.org/10.1098/rstb.2018.0442
1659 Lee, P.S., Grossman, A.D., 2006. The chromosome partitioning proteins Soj (ParA) and Spo0J
1660 (ParB) contribute to accurate chromosome partitioning, separation of replicated sister
1661 origins, and regulation of replication initiation in Bacillus subtilis. Mol. Microbiol. 60,
1662 853–869. https://doi.org/10.1111/j.1365-2958.2006.05140.x
1663 Lemon, K.P., Grossman, A.D., 2000. Movement of Replicating DNA through a Stationary
1664 Replisome. Mol. Cell 6, 1321–1330. https://doi.org/10.1016/S1097-2765(00)00130-1
1665 Lewis, P.J., Thaker, S.D., Errington, J., 2000. Compartmentalization of transcription and
1666 translation in Bacillus subtilis. EMBO J. 19, 710–718.
1667 https://doi.org/10.1093/emboj/19.4.710

1668 Lewis, R.A., Bignell, C.R., Zeng, W., Jones, A.C., Thomas, C.M., 2002. Chromosome loss from par
1669 mutants of Pseudomonas putida depends on growth medium and phase of growth.
1670 Microbiology 148, 537–548. https://doi.org/10.1099/00221287-148-2-537
1671 Li, H., 2019. Random Chromosome Partitioning in the Polyploid Bacterium *Thermus*
1672 *thermophilus* HB27. G3 GenesGenomesGenetics 9, 1249–1261.
1673 https://doi.org/10.1534/g3.119.400086
1674 Li, H., Angelov, A., Pham, V.T.T., Leis, B., Liebl, W., 2015. Characterization of chromosomal and
1675 megaplasmid partitioning loci in Thermus thermophilus HB27. BMC Genomics 16, 317.
1676 https://doi.org/10.1186/s12864-015-1523-3
1677 Lim, H.C., Surovtsev, I.V., Beltran, B.G., Huang, F., Bewersdorf, J., Jacobs-Wagner, C., 2014.
1678 Evidence for a DNA-relay mechanism in ParABS-mediated chromosome segregation.
1679 eLife 3, e02758. https://doi.org/10.7554/eLife.02758
1680 Lin, W.-H., Jacobs-Wagner, C., 2022. Connecting single-cell ATP dynamics to overflow
1681 metabolism, cell growth, and the cell cycle in Escherichia coli. Curr. Biol. 32, 3911-
1682 3924.e4. https://doi.org/10.1016/j.cub.2022.07.035
1683 Lindner, A.B., Madden, R., Demarez, A., Stewart, E.J., Taddei, F., 2008. Asymmetric segregation
1684 of protein aggregates is associated with cellular aging and rejuvenation. Proc. Natl.
1685 Acad. Sci. 105, 3076–3081. https://doi.org/10.1073/pnas.0708931105
1686 Livny, J., Yamaichi, Y., Waldor, M.K., 2007. Distribution of Centromere-Like *parS* Sites in
1687 Bacteria: Insights from Comparative Genomics. J. Bacteriol. 189, 8693–8703.
1688 https://doi.org/10.1128/JB.01239-07
1689 Mäkelä, J., Papagiannakis, A., Lin, W.-H., Lanz, M.C., Glenn, S., Swaffer, M., Marinov, G.K.,
1690 Skotheim, J.M., Jacobs-Wagner, C., 2024. Genome concentration limits cell growth and
1691 modulates proteome composition in *Escherichia coli*.
1692 https://doi.org/10.1101/2024.02.26.582181
1693 Mäkelä, J., Uphoff, S., Sherratt, D.J., 2021. Nonrandom segregation of sister chromosomes by
1694 *Escherichia coli* MukBEF. Proc. Natl. Acad. Sci. 118, e2022078118.
1695 https://doi.org/10.1073/pnas.2022078118
1696 Mao, S., Chakraverti-Wuerthwein, M.S., Gaudio, H., Košmrlj, A., 2020. Designing the
1697 Morphology of Separated Phases in Multicomponent Liquid Mixtures. Phys. Rev. Lett.
1698 125, 218003. https://doi.org/10.1103/PhysRevLett.125.218003
1699 Mao, S., Kuldinow, D., Haataja, M.P., Košmrlj, A., 2019. Phase behavior and morphology of
1700 multicomponent liquid mixtures. Soft Matter 15, 1297–1311.
1701 https://doi.org/10.1039/C8SM02045K
1702 McGuffee, S.R., Elcock, A.H., 2010. Diffusion, Crowding & Protein Stability in a Dynamic
1703 Molecular Model of the Bacterial Cytoplasm. PLoS Comput. Biol. 6, e1000694.
1704 https://doi.org/10.1371/journal.pcbi.1000694
1705 McKinney, W., 2010. Data Structures for Statistical Computing in Python. Presented at the
1706 Python in Science Conference, Austin, Texas, pp. 56–61.
1707 https://doi.org/10.25080/Majora-92bf1922-00a
1708 Miangolarra, A.M., Li, S.H.-J., Joanny, J.-F., Wingreen, N.S., Castellana, M., 2021. Steric
1709 interactions and out-of-equilibrium processes control the internal organization of
1710 bacteria. Proc. Natl. Acad. Sci. 118, e2106014118.
1711 https://doi.org/10.1073/pnas.2106014118

1712 Minnen, A., Attaiech, L., Thon, M., Gruber, S., Veening, J.-W., 2011. SMC is recruited to oriC by
1713 ParB and promotes chromosome segregation in Streptococcus pneumoniae:
1714 Chromosome segregation in S. pneumoniae. Mol. Microbiol. 81, 676–688.
1715 https://doi.org/10.1111/j.1365-2958.2011.07722.x
1716 Mohapatra, S., Weisshaar, J.C., 2018. Functional mapping of the *E. coli* translational machinery
1717 using single-molecule tracking. Mol. Microbiol. 110, 262–282.
1718 https://doi.org/10.1111/mmi.14103
1719 Mohl, D.A., Gober, J.W., 1997. Cell Cycle–Dependent Polar Localization of Chromosome
1720 Partitioning Proteins in Caulobacter crescentus. Cell 88, 675–684.
1721 https://doi.org/10.1016/S0092-8674(00)81910-8
1722 Molenaar, D., Van Berlo, R., De Ridder, D., Teusink, B., 2009. Shifts in growth strategies reflect
1723 tradeoffs in cellular economics. Mol. Syst. Biol. 5, 323.
1724 https://doi.org/10.1038/msb.2009.82
1725 Mondal, J., Bratton, B.P., Li, Y., Yethiraj, A., Weisshaar, J.C., 2011. Entropy-Based Mechanism of
1726 Ribosome-Nucleoid Segregation in E. coli Cells. Biophys. J. 100, 2605–2613.
1727 https://doi.org/10.1016/j.bpj.2011.04.030
1728 Navarro, P.P., Vettiger, A., Ananda, V.Y., Llopis, P.M., Allolio, C., Bernhardt, T.G., Chao, L.H.,
1729 2022. Cell wall synthesis and remodelling dynamics determine division site architecture
1730 and cell shape in Escherichia coli. Nat. Microbiol. 7, 1621–1634.
1731 https://doi.org/10.1038/s41564-022-01210-z
1732 Otsu, N., 1979. A Threshold Selection Method from Gray-Level Histograms. IEEE Trans. Syst.
1733 Man Cybern. 9, 62–66. https://doi.org/10.1109/TSMC.1979.4310076
1734 Paintdakhi, A., Parry, B., Campos, M., Irnov, I., Elf, J., Surovtsev, I., Jacobs-Wagner, C., 2016.
1735 Oufti: an integrated software package for high-accuracy, high-throughput quantitative
1736 microscopy analysis: Oufti: image analysis software. Mol. Microbiol. 99, 767–777.
1737 https://doi.org/10.1111/mmi.13264
1738 Pande, S., Mitra, D., Chatterji, A., 2023. Entropy mediated organization of E.coli chromosome in
1739 fast growth conditions. https://doi.org/10.48550/ARXIV.2304.02275
1740 Parry, B.R., Surovtsev, I.V., Cabeen, M.T., O'Hern, C.S., Dufresne, E.R., Jacobs-Wagner, C., 2014.
1741 The Bacterial Cytoplasm Has Glass-like Properties and Is Fluidized by Metabolic Activity.
1742 Cell 156, 183–194. https://doi.org/10.1016/j.cell.2013.11.028
1743 Paszke, A., Gross, S., Massa, F., Lerer, A., Bradbury, J., Chanan, G., Killeen, T., Lin, Z., Gimelshein,
1744 N., Antiga, L., Desmaison, A., Köpf, A., Yang, E., DeVito, Z., Raison, M., Tejani, A.,
1745 Chilamkurthy, S., Steiner, B., Fang, L., Bai, J., Chintala, S., 2019. PyTorch: An Imperative
1746 Style, High-Performance Deep Learning Library.
1747 https://doi.org/10.48550/ARXIV.1912.01703
1748 Pedregosa, F., Varoquaux, G., Gramfort, A., Michel, V., Thirion, B., Grisel, O., Blondel, M.,
1749 Müller, A., Nothman, J., Louppe, G., Prettenhofer, P., Weiss, R., Dubourg, V., Vanderplas,
1750 J., Passos, A., Cournapeau, D., Brucher, M., Perrot, M., Duchesnay, É., 2012. Scikit-learn:
1751 Machine Learning in Python. https://doi.org/10.48550/ARXIV.1201.0490
1752 Pelletier, J., Halvorsen, K., Ha, B.-Y., Paparcone, R., Sandler, S.J., Woldringh, C.L., Wong, W.P.,
1753 Jun, S., 2012. Physical manipulation of the *Escherichia coli* chromosome reveals its soft
1754 nature. Proc. Natl. Acad. Sci. 109. https://doi.org/10.1073/pnas.1208689109

1755 Pettijohn, D.E., Hecht, R., 1974. RNA Molecules Bound to the Folded Bacterial Genome Stabilize
1756 DNA Folds and Segregate Domains of Supercoiling. Cold Spring Harb. Symp. Quant. Biol.
1757 38, 31–41. https://doi.org/10.1101/SQB.1974.038.01.006
1758 Pountain, A.W., Jiang, P., Yao, T., Homaee, E., Guan, Y., Podkowik, M., Shopsin, B., Torres, V.J.,
1759 Golding, I., Yanai, I., 2022. Transcription-replication interactions reveal principles of
1760 bacterial genome regulation (preprint). Systems Biology.
1761 https://doi.org/10.1101/2022.10.22.513359
1762 Proenca, A.M., Rang, C.U., Qiu, A., Shi, C., Chao, L., 2019. Cell aging preserves cellular
1763 immortality in the presence of lethal levels of damage. PLOS Biol. 17, e3000266.
1764 https://doi.org/10.1371/journal.pbio.3000266
1765 Reyes-Lamothe, R., Tran, T., Meas, D., Lee, L., Li, A.M., Sherratt, D.J., Tolmasky, M.E., 2014.
1766 High-copy bacterial plasmids diffuse in the nucleoid-free space, replicate stochastically
1767 and are randomly partitioned at cell division. Nucleic Acids Res. 42, 1042–1051.
1768 https://doi.org/10.1093/nar/gkt918
1769 Robinow, C., Kellenberger, E., 1994. The bacterial nucleoid revisited. Microbiol. Rev. 58, 211–
1770 232. https://doi.org/10.1128/mr.58.2.211-232.1994
1771 Sadhir, I., Murray, S.M., 2023. Mid-cell migration of the chromosomal terminus is coupled to
1772 origin segregation in Escherichia coli. Nat. Commun. 14, 7489.
1773 https://doi.org/10.1038/s41467-023-43351-7
1774 Sanamrad, A., Persson, F., Lundius, E.G., Fange, D., Gynnå, A.H., Elf, J., 2014. Single-particle
1775 tracking reveals that free ribosomal subunits are not excluded from the *Escherichia coli*
1776 nucleoid. Proc. Natl. Acad. Sci. 111, 11413–11418.
1777 https://doi.org/10.1073/pnas.1411558111
1778 Santi, I., McKinney, J.D., 2015. Chromosome Organization and Replisome Dynamics in
1779 Mycobacterium smegmatis. mBio 6, e01999-14. https://doi.org/10.1128/mBio.01999-14
1780 Sawitzke, J.A., Austin, S., 2000. Suppression of chromosome segregation defects of *Escherichia*
1781 *coli muk* mutants by mutations in topoisomerase I. Proc. Natl. Acad. Sci. 97, 1671–1676.
1782 https://doi.org/10.1073/pnas.030528397
1783 Schaechter, M., MaalOe, O., Kjeldgaard, N.O., 1958. Dependency on Medium and Temperature
1784 of Cell Size and Chemical Composition during Balanced Growth of Salmonella
1785 typhimurium. J. Gen. Microbiol. 19, 592–606. https://doi.org/10.1099/00221287-19-3-
1786 592
1787 Scholz, S.A., Diao, R., Wolfe, M.B., Fivenson, E.M., Lin, X.N., Freddolino, P.L., 2019. High-
1788 Resolution Mapping of the Escherichia coli Chromosome Reveals Positions of High and
1789 Low Transcription. Cell Syst. 8, 212-225.e9. https://doi.org/10.1016/j.cels.2019.02.004
1790 Scott, D.W., 1992. Multivariate Density Estimation: Theory, Practice, and Visualization, 1st ed,
1791 Wiley Series in Probability and Statistics. Wiley.
1792 https://doi.org/10.1002/9780470316849
1793 Scott, M., Klumpp, S., Mateescu, E.M., Hwa, T., 2014. Emergence of robust growth laws from
1794 optimal regulation of ribosome synthesis. Mol. Syst. Biol. 10, 747.
1795 https://doi.org/10.15252/msb.20145379
1796 Seabold, S., Perktold, J., 2010. Statsmodels: Econometric and Statistical Modeling with Python.
1797 Presented at the Python in Science Conference, Austin, Texas, pp. 92–96.
1798 https://doi.org/10.25080/Majora-92bf1922-011

1799 Shis, D.L., Bennett, M.R., 2013. Library of synthetic transcriptional AND gates built with split T7
1800 RNA polymerase mutants. Proc. Natl. Acad. Sci. 110, 5028–5033.
1801 https://doi.org/10.1073/pnas.1220157110
1802 Si, F., Li, D., Cox, S.E., Sauls, J.T., Azizi, O., Sou, C., Schwartz, A.B., Erickstad, M.J., Jun, Y., Li, X.,
1803 Jun, S., 2017. Invariance of Initiation Mass and Predictability of Cell Size in Escherichia
1804 coli. Curr. Biol. 27, 1278–1287. https://doi.org/10.1016/j.cub.2017.03.022
1805 Slayter, H., Kiho, Y., Hall, C.E., Rich, A., 1968. AN ELECTRON MICROSCOPIC STUDY OF LARGE
1806 BACTERIAL POLYRIBOSOMES. J. Cell Biol. 37, 583–590.
1807 https://doi.org/10.1083/jcb.37.2.583
1808 Stylianidou, S., Brennan, C., Nissen, S.B., Kuwada, N.J., Wiggins, P.A., 2016. *SuperSegger* : robust
1809 image segmentation, analysis and lineage tracking of bacterial cells. Mol. Microbiol. 102,
1810 690–700. https://doi.org/10.1111/mmi.13486
1811 Subach, O.M., Cranfill, P.J., Davidson, M.W., Verkhusha, V.V., 2011. An Enhanced Monomeric
1812 Blue Fluorescent Protein with the High Chemical Stability of the Chromophore. PLoS
1813 ONE 6, e28674. https://doi.org/10.1371/journal.pone.0028674
1814 Subramanian, S., Murray, S.M., 2023. Subdiffusive movement of chromosomal loci in bacteria
1815 explained by DNA bridging. Phys. Rev. Res. 5, 023034.
1816 https://doi.org/10.1103/PhysRevResearch.5.023034
1817 Takacs, C.N., Wachter, J., Xiang, Y., Ren, Z., Karaboja, X., Scott, M., Stoner, M.R., Irnov, I.,
1818 Jannetty, N., Rosa, P.A., Wang, X., Jacobs-Wagner, C., 2022. Polyploidy, regular
1819 patterning of genome copies, and unusual control of DNA partitioning in the Lyme
1820 disease spirochete. Nat. Commun. 13, 7173. https://doi.org/10.1038/s41467-022-
1821 34876-4
1822 Thappeta, Y., Cañas-Duarte, S.J., Kallem, T., Fragasso, A., Xiang, Y., Gray, W., Lee, C., Cegelski, L.,
1823 Jacobs-Wagner, C., 2024. Glycogen phase separation drives macromolecular
1824 rearrangement and asymmetric division in *E. coli*.
1825 https://doi.org/10.1101/2024.04.19.590186
1826 Tiruvadi-Krishnan, S., Männik, Jaana, Kar, P., Lin, J., Amir, A., Männik, Jaan, 2022. Coupling
1827 between DNA replication, segregation, and the onset of constriction in Escherichia coli.
1828 Cell Rep. 38, 110539. https://doi.org/10.1016/j.celrep.2022.110539
1829 Tseng, H.-C., Harwell, C.L., Martin, C.H., Prather, K.L., 2010a. Biosynthesis of chiral 3-
1830 hydroxyvalerate from single propionate-unrelated carbon sources in metabolically
1831 engineered E. coli. Microb. Cell Factories 9, 96. https://doi.org/10.1186/1475-2859-9-96
1832 Tseng, H.-C., Harwell, C.L., Martin, C.H., Prather, K.L., 2010b. Biosynthesis of chiral 3-
1833 hydroxyvalerate from single propionate-unrelated carbon sources in metabolically
1834 engineered E. coli. Microb. Cell Factories 9, 96. https://doi.org/10.1186/1475-2859-9-96
1835 Van Der Walt, S., Schönberger, J.L., Nunez-Iglesias, J., Boulogne, F., Warner, J.D., Yager, N.,
1836 Gouillart, E., Yu, T., 2014. scikit-image: image processing in Python. PeerJ 2, e453.
1837 https://doi.org/10.7717/peerj.453
1838 Varricchio, F., Monier, R., 1971. Ribosome Patterns in *Escherichia coli* Growing at Various Rates.
1839 J. Bacteriol. 108, 105–110. https://doi.org/10.1128/jb.108.1.105-110.1971
1840 Virtanen, P., Gommers, R., Oliphant, T.E., Haberland, M., Reddy, T., Cournapeau, D., Burovski,
1841 E., Peterson, P., Weckesser, W., Bright, J., Van Der Walt, S.J., Brett, M., Wilson, J.,
1842 Millman, K.J., Mayorov, N., Nelson, A.R.J., Jones, E., Kern, R., Larson, E., Carey, C.J.,

1843 Polat, İ., Feng, Y., Moore, E.W., VanderPlas, J., Laxalde, D., Perktold, J., Cimrman, R.,
1844 Henriksen, I., Quintero, E.A., Harris, C.R., Archibald, A.M., Ribeiro, A.H., Pedregosa, F.,
1845 Van Mulbregt, P., SciPy 1.0 Contributors, Vijaykumar, A., Bardelli, A.P., Rothberg, A.,
1846 Hilboll, A., Kloeckner, A., Scopatz, A., Lee, A., Rokem, A., Woods, C.N., Fulton, C.,
1847 Masson, C., Häggström, C., Fitzgerald, C., Nicholson, D.A., Hagen, D.R., Pasechnik, D.V.,
1848 Olivetti, E., Martin, E., Wieser, E., Silva, F., Lenders, F., Wilhelm, F., Young, G., Price, G.A.,
1849 Ingold, G.-L., Allen, G.E., Lee, G.R., Audren, H., Probst, I., Dietrich, J.P., Silterra, J.,
1850 Webber, J.T., Slavič, J., Nothman, J., Buchner, J., Kulick, J., Schönberger, J.L., De Miranda
1851 Cardoso, J.V., Reimer, J., Harrington, J., Rodríguez, J.L.C., Nunez-Iglesias, J., Kuczynski, J.,
1852 Tritz, K., Thoma, M., Newville, M., Kümmerer, M., Bolingbroke, M., Tartre, M., Pak, M.,
1853 Smith, N.J., Nowaczyk, N., Shebanov, N., Pavlyk, O., Brodtkorb, P.A., Lee, P., McGibbon,
1854 R.T., Feldbauer, R., Lewis, S., Tygier, S., Sievert, S., Vigna, S., Peterson, S., More, S.,
1855 Pudlik, T., Oshima, T., Pingel, T.J., Robitaille, T.P., Spura, T., Jones, T.R., Cera, T., Leslie,
1856 T., Zito, T., Krauss, T., Upadhyay, U., Halchenko, Y.O., Vázquez-Baeza, Y., 2020. SciPy 1.0:
1857 fundamental algorithms for scientific computing in Python. Nat. Methods 17, 261–272.
1858 https://doi.org/10.1038/s41592-019-0686-2
1859 Wang, P., Robert, L., Pelletier, J., Dang, W.L., Taddei, F., Wright, A., Jun, S., 2010. Robust Growth
1860 of Escherichia coli. Curr. Biol. 20, 1099–1103. https://doi.org/10.1016/j.cub.2010.04.045
1861 Wang, X., Liu, X., Possoz, C., Sherratt, D.J., 2006. The two *Escherichia coli* chromosome arms
1862 locate to separate cell halves. Genes Dev. 20, 1727–1731.
1863 https://doi.org/10.1101/gad.388406
1864 Waskom, M., 2021. seaborn: statistical data visualization. J. Open Source Softw. 6, 3021.
1865 https://doi.org/10.21105/joss.03021
1866 Weitao, T., Nordstrom, K., Dasgupta, S., 1999. Mutual suppression of mukB and seqA
1867 phenotypes might arise from their opposing influences on the Escherichia coli nucleoid
1868 structure. Mol. Microbiol. 34, 157–168. https://doi.org/10.1046/j.1365-
1869 2958.1999.01589.x
1870 Wientjes, F.B., Nanninga, N., 1989. Rate and topography of peptidoglycan synthesis during cell
1871 division in Escherichia coli: concept of a leading edge. J. Bacteriol. 171, 3412–3419.
1872 https://doi.org/10.1128/jb.171.6.3412-3419.1989
1873 Wiktor, J., Gynnå, A.H., Leroy, P., Larsson, J., Coceano, G., Testa, I., Elf, J., 2021. RecA finds
1874 homologous DNA by reduced dimensionality search. Nature 597, 426–429.
1875 https://doi.org/10.1038/s41586-021-03877-6
1876 Woldringh, C.L., Huls, P., Pas, E., Brakenhoff, G.J., Nanninga, N., 1987. Topography of
1877 Peptidoglycan Synthesis during Elongation and Polar Cap Formation in a Cell Division
1878 Mutant of Escherichia coli MC4100. Microbiology 133, 575–586.
1879 https://doi.org/10.1099/00221287-133-3-575
1880 Wu, F., Japaridze, A., Zheng, X., Wiktor, J., Kerssemakers, J.W.J., Dekker, C., 2019a. Direct
1881 imaging of the circular chromosome in a live bacterium. Nat. Commun. 10, 2194.
1882 https://doi.org/10.1038/s41467-019-10221-0
1883 Wu, F., Swain, P., Kuijpers, L., Zheng, X., Felter, K., Guurink, M., Solari, J., Jun, S., Shimizu, T.S.,
1884 Chaudhuri, D., Mulder, B., Dekker, C., 2019b. Cell Boundary Confinement Sets the Size
1885 and Position of the E. coli Chromosome. Curr. Biol. 29, 2131-2144.e4.
1886 https://doi.org/10.1016/j.cub.2019.05.015

1887 Xiang, Y., Surovtsev, I.V., Chang, Y., Govers, S.K., Parry, B.R., Liu, J., Jacobs-Wagner, C., 2021.
1888 Interconnecting solvent quality, transcription, and chromosome folding in Escherichia
1889 coli. Cell 184, 3626-3642.e14. https://doi.org/10.1016/j.cell.2021.05.037
1890 Yamaichi, Y., Fogel, M.A., McLeod, S.M., Hui, M.P., Waldor, M.K., 2007. Distinct Centromere-
1891 Like *parS* Sites on the Two Chromosomes of *Vibrio* spp. J. Bacteriol. 189, 5314–5324.
1892 https://doi.org/10.1128/JB.00416-07
1893 Yang, D., Männik, Jaana, Retterer, S.T., Männik, Jaan, 2020. The effects of polydisperse
1894 crowders on the compaction of the *Escherichia coli* nucleoid. Mol. Microbiol. 113, 1022–
1895 1037. https://doi.org/10.1111/mmi.14467
1896 Yao, S., Helinski, D.R., Toukdarian, A., 2007. Localization of the Naturally Occurring Plasmid
1897 ColE1 at the Cell Pole. J. Bacteriol. 189, 1946–1953. https://doi.org/10.1128/JB.01451-
1898 06
1899 Yu, W., Herbert, S., Graumann, P.L., Götz, F., 2010. Contribution of SMC (Structural
1900 Maintenance of Chromosomes) and SpoIIIE to Chromosome Segregation in
1901 Staphylococci. J. Bacteriol. 192, 4067–4073. https://doi.org/10.1128/JB.00010-10
1902 Zhang, C., Shao, P.G., Van Kan, J.A., Van Der Maarel, J.R.C., 2009. Macromolecular crowding
1903 induced elongation and compaction of single DNA molecules confined in a nanochannel.
1904 Proc. Natl. Acad. Sci. 106, 16651–16656. https://doi.org/10.1073/pnas.0904741106
1905 Zhou, Z., Siddiquee, M.M.R., Tajbakhsh, N., Liang, J., 2020. UNet++: Redesigning Skip
1906 Connections to Exploit Multiscale Features in Image Segmentation. IEEE Trans. Med.
1907 Imaging 39, 1856–1867. https://doi.org/10.1109/TMI.2019.2959609
1908 Zimmerman, S.B., Trach, S.O., 1991. Estimation of macromolecule concentrations and excluded
1909 volume effects for the cytoplasm of Escherichia coli. J. Mol. Biol. 222, 599–620.
1910 https://doi.org/10.1016/0022-2836(91)90499-V
1911
1912
1913 **FIGURE LEGENDS**
1914 **Figure 1: Correlations between polysome and nucleoid dynamics at the single-cell level.** CJW7323
1915 cells were grown in in M9gluCAAT in a microfluidic device**. A.** Schematic illustrating observable nucleoid
1916 segregation events. **B.** Fluorescence images of RplA-GFP and HupA-mCherry for a representative cell
1917 (CJW7323) from birth to division. **C.** Ensemble kymographs of the average RplA-GFP and HupA-mCherry
1918 fluorescence during the cell division cycle (>300,000 segmented cell instances from 4122 complete cell
1919 division cycles). **D.** Two-dimensional projections of the average RplA-GFP and HupA-mCherry
1920 fluorescence signals in predivisional cells (4564 cells with two nucleoid objects, from 1907 cell division
1921 cycles, 95-100% into the cell division cycle) and their intensity profiles. White arrows indicate RplA-GFP
1922 enrichments at the quarter cell positions, while the black arrow indicates the site of cell constriction. **E.** Plot
1923 showing the dynamics of RplA-GFP accumulation and HupA-mCherry depletion at mid-nucleoid (median ±
1924 IQR) during the nucleoid cycle (see Figure 1 – Figure supplement 2D). Data from 3240 nucleoid segregation
1925 cycles are shown (40 nucleoid cycle bins, 2512-4823 segmented nucleoids per bin). **F.** Correlation
1926 (Spearman ρ = -0.52, p-value < 10^{-10}) between the rate of RplA-GFP accumulation in the middle of the
1927 nucleoid ($\frac{\Delta RplA_{mid-nuc}\ conc.}{\Delta T}$) and the rate of HupA-mCherry depletion in the same region ($\frac{\Delta HupA_{mid-nuc}\ conc.}{\Delta T}$)

between the initiation of nucleoid splitting and just before the end of nucleoid splitting (3214 complete nucleoid cycles). The colormap indicates the Gaussian kernel density estimation (KDE). Solid black line indicates the linear-regression fit to the data. **G.** Percentage of cells that continue to accumulate polysomes in the middle of the cell ($\frac{\Delta RplA_{mid-cell}\ conc.}{\Delta T}$) during four relative time bins (1335 to 1957 cell division cycles per bin) covering the period from the end of nucleoid splitting until cell division. **H.** Correlation (Spearman $\rho = 0.47$, p-value $< 10^{-10}$) between the rate of RplA-GFP accumulation at mid-cell ($\frac{\Delta RplA_{mid-cell}\ conc.}{\Delta T}$) and the rate of distance increase between the sister nucleoids ($\frac{\Delta Distance_{nuc}}{\Delta T}$) during the first quartile (0-25%) of the period between the end of nucleoid splitting and cell division (1376 cell division cycles). The black markers correspond to nine bins (mean ± SEM, 75 to 177 cell division cycles per bin) within the 5th-95th percentiles of *x*-axis range. Also shown is the distribution of the cell elongation rates ($\frac{\Delta Length_{cell}}{\Delta T}$) during the same time interval, with the mean and SD shown by the solid and dashed lines, respectively. **I.** Plot showing the coefficients of a linear mixed-effects model (see eq. 3 in Methods and Figure 1 – figure supplement 3B) for four interval bins between the completion of nucleoid splitting and cell division. The coefficients quantify the relative contribution of polysome accumulation at mid-cell ($\frac{\Delta RplA_{mid-cell}\ conc.}{\Delta T}$) and cell elongation ($\frac{\Delta Length_{cell}}{\Delta T}$) to the rate of sister nucleoid migration ($\frac{\Delta Distance_{nuc}}{\Delta T}$). All coefficients are significant (Prob(<|Z|) $< 10^{-9}$), except for the one marked with an asterisk that is marginally significant (Prob(<|Z|) = 0.02).

Figure 2: Correlation of the extent and relative timing of polysome accumulation with nucleoid segregation at the population and single-cell levels. A. RplA-mEos2 and DAPI (scaled by the whole cell average) demographs constructed from snapshots of DAPI-stained CJW6768 cells (815 to 2771 cells per demograph) expressing RplA-mEos2 and growing in different nutrient conditions (see Table S1 for abbreviations). The demographs were arranged from smallest (M9mann, top) to biggest average cell area (M9malaCAAT, bottom). Additional demographs for different ribosomal reporters and nutrient conditions are shown in Figure 2 – figure supplement 1. **B.** Correlation between average polysome accumulation and average nucleoid depletion at mid-cell for all tested strains (Spearman $\rho_{all} = -0.85$, p-value $< 10^{-10}$) with different ribosomal and nucleoid reporters, and within each strain ($-0.75 <$ Spearman $\rho_{strain} < -0.95$, p-values $< 10^{-3}$) across nutrient conditions. A linear regression was fitted to all the data. **D.** Plot showing the variability in growth rate (GR) across cell division cycles for cells growing in microfluidics in M9gluCAAT (4114 cell division cycles, 9 growth rate bins with 93 to 860 cell division cycles each). **E.** Ensemble kymographs of the RplA-GFP and HupA-mCherry concentration normalized by the average fluorescence for the slowest, intermediate and fastest growing population bins shown in panel D. **F.** Plot showing the correlation between the average RplA-GFP accumulation and HupA-mCherry depletion at mid-cell across the growth rate bins (mean ± SD, 93 to 860 cell division cycles per bin) shown in panel D.

1962 **Figure 3: Correlations between polysome and nucleoid asymmetries. A.** Distributions of RplA-GFP
1963 concentration in the new (grey) and the old (black) pole regions of newborn cells (0-2.5% of the cell division
1964 cycle, n = 912 cell division cycles). The histograms were smoothed using Gaussian kernel density
1965 estimations. **B.** Correlation (Spearman ρ = -0.41, p-value < 10^{-10}) between the polar polysome asymmetry
1966 and the position of the nucleoid centroid around the cell center of cells at the beginning of the division cycle
1967 (0-10%, n = 1179 cell division cycles). The contour plot consists of 9 levels with a lower data density
1968 threshold of 25%. The polar polysome profile for cells with correlations indicated by the numbers 1 and 2
1969 are schematically illustrated in the next panel. A linear regression (solid grey line) was fitted to the data. **C.**
1970 Schematic illustrating the effects of the relative polysome abundance between the poles on the position of
1971 the nucleoid. **D.** Average 2D projections of the RplA-GFP and HupA-mCherry concentration (conc.) at
1972 different cell division cycle intervals (~9440 to 47240 cell images per cell division cycle interval from 4122
1973 cell division cycles). The dotted line indicates the boundary between two cell division cycles. **E.** Density plot
1974 comparing the distribution of the HupA-mCherry maximum concentration toward the new pole (gray) to that
1975 toward the old pole (black) in newborn cells (0-2.5% of the division cycle, n = 912 cell division cycles). The
1976 histograms were smoothed using Gaussian kernel density estimations. **F.** Correlation (Spearman ρ = 0.52,
1977 p-value<10^{-10}) between the nucleoid density asymmetry and the relative availability of polysome-free space
1978 between the two cell halves early in the cell division cycle (0-10% of the division cycle, n = 2150 cell division
1979 cycles). The contour plot consists of 9 levels with a lower data density threshold of 25%. Values above 1
1980 on the *x*-axis indicate more polysome-free space toward the new pole, and values below 1 correspond to
1981 cells with more polysome-free space toward the old pole. On the *y*-axis, values above 1 indicate higher
1982 DNA density toward the new pole and values below 1 indicate higher DNA density toward the old pole. **G.**
1983 Average 2D projections of newborn cells (0-10% into the cell division cycle) from the lower-left quartile in
1984 panel C (region 2, n = 223 cell division cycles) and the upper right quartile in panel C (region 1, n = 557 cell
1985 division cycles) and their 1D intensity profiles.
1986
1987 **Figure 4: Simulation results of the reaction-diffusion model for different growth rates or nucleoid**
1988 **diffusion rates, and comparison of the nonequilibrium polysome accumulation with freely diffusing**
1989 **particles. A.** 1D simulation of polysome (blue) and nucleoid (red) dynamics during slow growth (growth
1990 rate = 0.25 h^{-1}, D_n = 0.001 $\mu m^2/s$, cell length at birth = 1.84 μm) at different relative cell division cycle
1991 timepoints. The simulation was initialized from the equilibrium polysome and nucleoid distribution (at 0%).
1992 **B.** Schematic summarizing how polysomes accumulate in the middle of the elongating nucleoid, causing
1993 nucleoid splitting. **C.** Correlation between the relative timing of nucleoid splitting and the growth rate as
1994 captured by our reaction-diffusion model (D_n = 0.001 μm^2/sec) across six growth rate bins. The cell and
1995 nucleoid lengths for each growth rate bin matched previously published data shown in Figure 4 – figure
1996 supplement 1A. **D.** Deviation between the steady state after infinite relaxation time (dashed curves) and the
1997 polysome or nucleoid profiles in newborn cells after one simulation round (solid curves) for increasing
1998 nucleoid diffusion constants during fast growth (1 h^{-1}). **E.** Phase contrast and fluorescence (fluor.) images

1999 of two representative single cells (CJW7651). The red circles indicate the position of the mCherry-μNS
2000 particle in each cell. **F.** Two-dimensional average cell projections of the DAPI concentration (conc.) and the
2001 RplA-msfGFP concentration, and 2D histogram of the mCherry-μNS particle density for four cell length bins
2002 of CJW7651 cells (~2580 cells per bin) grown in M9gluCAAT and spotted on an agarose pad containing
2003 the same medium. Since the cell pole identity cannot be inferred from snapshot images, pole assignment
2004 was random. **G.** Average 1D profiles of the scaled DAPI and RplA-msfGFP concentrations and the
2005 mCherry-μNS probability density.
2006
2007 **Figure 5: Effects of rifampicin treatment and polysome depletion on nucleoid segregation and**
2008 **compaction. A.** Plot showing the average instantaneous growth rate (mean ± SD shown by the solid black
2009 curve and grey shaded region, respectively) of a cell population (n = 2629 cell division cycles) undergoing
2010 two rounds of rifampicin treatment in a microfluidic device supplemented with M9gluCAAT. The distribution
2011 of the average cell cycle growth rate of unperturbed populations is also shown on the right (n = 4122 cell
2012 division cycles from a different microfluidics experiment). The solid horizontal line indicates the average
2013 growth rate. **B.** Plot showing the average distance between nucleoid peaks for a population of cells
2014 (squares, 114 cell division cycles) that were born (-112 to -102 min) and divided before the addition of
2015 rifampicin, and for a population of cells (circles, 112 cell division cycles) that were born just before (-22 to -
2016 12 min) and divided after the addition of rifampicin. A third-degree polynomial was fitted to the data from
2017 the unperturbed population (solid blue curve) and juxtaposed (dashed blue curve) with the data from the
2018 interrupted population. **C.** Average 1D profile and 2D projections of the scaled (divided by the whole cell
2019 average concentration) RplA-GFP and HupA-mCherry signals for cells before and after rifampicin addition
2020 (n = 112 cell division cycles). The red dashed horizontal lines in the 1D intensity profiles and the white
2021 crosses in the 2D profiles mark the nucleoid peaks. **D.** Plot showing the RplA-GFP accumulation relative to
2022 the HupA-mCherry depletion at mid-cell from 0 to 24 min after birth (colormap) for cells that completed their
2023 division cycle before the addition of rifampicin (n = 114 cell division cycles) and for cells that were subjected
2024 to rifampicin 12 min (n = 112 cell division cycles) or 3 min (n = 99 cell division cycles) after birth. **E.** Average
2025 1D and 2D scaled RplA-GFP and HupA-mCherry intensity profiles for newborn cells (0 to 10 min after birth)
2026 before (left, n = 726 cell division cycles), just after (middle, n = 367 cell division cycles), and much after
2027 (right, n = 235 cell division cycles) rifampicin addition.
2028
2029 **Figure 6: Effects of ectopic polysome accumulation on nucleoid dynamics. A.** Schematic
2030 summarizing the experiment. **B.** Representative phase contrast and mTagBFP2 fluorescence images at
2031 different times after induction with IPTG (100 μM) are shown, next to a plot showing the mTagBFP2
2032 fluorescence of the entire population (mean ± SD, n = 3624 cell trajectories) over time. **C.** Plot showing how
2033 instantaneous growth rate (mean ±SD, n = 3624 mTagBFP2 induction trajectories) decreases following
2034 induction of mTagBFP2 synthesis. **D-F.** Representative kymographs and images of the normalized (divided
2035 by the whole cell average) RplA-msfGFP and HupA-mCherry fluorescence signals in cells (CJW7749) born

2036 during mTagBFP2 over-expression. **F.** Phase contrast images are shown to illustrate the formation of
2037 inclusion bodies (see also Figure 6 – figure supplement 1). Additional cell examples are shown in Movie
2038 S5.
2039
2040 **Figure 7: Effects of cell width increase on polysome and nucleoid dynamics. A.** Comparison of the
2041 cell width increase during cell growth between CJW7323 cells treated with cephalexin (mean ± SD, 360 cell
2042 growth trajectories, 418 to 1511 segmented cells per bin) and cells treated with both cephalexin (50 µg/mL)
2043 and A22 (4 µg/mL) (grey, mean ± SD, 309 cell growth trajectories, 51 to 1684 segmented cells per bin).
2044 The same cell area bins are compared between the two populations. **B.** Phase contrast and fluorescence
2045 images of a representative cephalexin-treated cell expressing RplA-GFP and HupA-mCherry. **C.** Same as
2046 B but for a short cell growing in the presence of A22 and cephalexin. **D.** Same as C but for a longer cell.
2047 The white arrowheads indicate the polysome bridges that connect polysome accumulations between two
2048 DNA-free regions. Additional examples are shown in Movie S6 **E.** Representative fluorescence images of
2049 RplA-GFP and HupA-mCherry in a cell treated with A22 and cephalexin. The dotted lines indicate the
2050 representative cross-like polysome accumulation, which forms during the fusion of the polysome
2051 accumulation towards the center (see also Movie S6). **F.** Comparison of the segmented polysome
2052 accumulations and nucleoid objects between A22+cephalexin (150 sampled segmented cells from 47
2053 growth trajectories) and cephalexin-treated (150 sampled segmented cells from 100 growth trajectories)
2054 cells. The polysome and nucleoid areas per cell were normalized by the population-average statistic from
2055 cephalexin-treated cells. All differences between the two populations are statistically significant (Mann-
2056 Whitney p-value < 10^{-10}).
2057
2058
2059 **Figure 1 – figure supplement 1: Reproducibility analysis of the dynamic ribosome and nucleoid**
2060 **distributions between microfluidic experiments.** While phase-contrast images were acquired every
2061 minute in all microfluidics experiments, two different intervals (1 min and 3 min) were used for fluorescence
2062 image acquisition. **A.** Kymographs showing the RplA-GFP and HupA-mCherry concentration in CJW7323
2063 cells growing in microfluidic channels in M9gluCAAT. Cell and nucleoid contours are shown in each channel
2064 using a different color for each cell lineage (from dark purple to bright orange). **B-E.** Two biological replicate
2065 experiments were performed for this strain and nutrient condition using different intervals of fluorescence
2066 image acquisition (1 or 3 min). **B.** Plots showing that the instantaneous and average division cycle growth
2067 rates were nearly identical between the two experiments. **C.** Plots showing the distributions of the indicated
2068 fluorescence signals for the 1-min acquisition interval (black) compared to the 3-min frame rate interval
2069 (orange) before and after correction. The difference in the excitation power between the two experiments
2070 was 50% (240 %ms vs. 360 %ms), which was also reflected in the ratio of their average fluorescence values
2071 (1.4 for RplA-GFP and 1.6 for HupA-mCherry). The fluorescence values from the 1-min interval experiment
2072 were corrected by multiplying by these ratios, resulting in a near-perfect overlap between fluorescence

2073 distributions after correction. **D.** Plots showing that the scaled (z-score) RplA-GFP and HupA-mCherry
2074 intensity profiles from birth to division were almost identical between the two experiments. The intensity
2075 profiles are shown for 10 cell division cycle intervals (1489 and 2633 cell division cycles for the 1-min and
2076 3-min interval experiments, respectively). The z-score was calculated for each segmented cell by
2077 subtracting the whole cell average fluorescence and then dividing the difference by the standard deviation.
2078 Each intensity profile corresponds to the average z-score of all segmented cell instances within the
2079 corresponding cell cycle interval. **E.** Plot showing that the average RplA-GFP concentration from birth to
2080 division (averages ± SD across 20 cell division cycle bins) remained constant and was virtually identical
2081 between the two experiments. **F.** Representative image of RplA-GFP fluorescence in cells (CJW7323)
2082 treated with rifampicin (100 µg/mL). The cells were treated for 45 min, washed, and spotted on an
2083 M9gluCAAT agarose pad without antibiotic. The presented snapshot corresponds to the first time point
2084 immediately after cell spotting showing diffuse distribution of RplA-GFP signal.
2085
2086 **Figure 1 – figure supplement 2: Tracking nucleoid segregation cycles.** Since the timing of nucleoid
2087 segregation varied between cell division cycles, the nucleoid segregation cycles were tracked
2088 independently of the cell division cycles for each cell lineage to measure the relative timing of RplA-GFP
2089 accumulation and HupA-mCherry depletion in the middle of the nucleoid (as shown in Figure 1E). **A.** Plots
2090 showing the frequency of cells with one, two, three, or four detected nucleoid objects across 10 cell division
2091 cycle bins from birth (top) to division (bottom). Data from 4122 cell division cycles are shown. **B.** The polarity
2092 of the cells (+/-) and the relative position of the nucleoid mask (toward the new or old pole) was used to
2093 track the nucleoid segregation cycle. This strategy was used to identify four groups of nucleoid segregation
2094 cycles (group -2, -1, 1 and 2). Group -2 includes nucleoids that were "born" toward the old cell pole in a
2095 mother cell with negative (-) polarity and were inherited at the center of a daughter cell with a negative
2096 polarity. Group -1 includes nucleoids that were "born" toward the new cell pole in a mother cell with negative
2097 (-) polarity and were inherited at the center of a daughter cell with a positive (+) polarity. Group 1 includes
2098 nucleoids that were "born" toward the new cell pole in a mother cell with positive (+) polarity and were
2099 inherited at the center of a daughter cell with negative (-) polarity. Group 2 includes nucleoids that were
2100 "born" toward the old cell pole in a mother cell with positive (+) polarity and were inherited at the center of
2101 a daughter cell with positive (+) polarity. **C.** Plots showing the distributions of nucleoid positions around the
2102 cell center for 10 nucleoid segregation cycle bins, from the time a nucleoid was "born" (top) until it split
2103 (bottom). These plots show the inheritance of the nucleoids from the quarter cell positions of the mother
2104 cells to the middle of their daughters for the four groups of nucleoid segregation cycles. The solid gray line
2105 represents the average density of the nucleoid positions for all four groups. Data from 2286 complete
2106 nucleoid cycles are shown. **D.** Schematic that explains the definition of a nucleoid cycle. The nucleoid cycle
2107 ranges from the end of a nucleoid splitting event, until the next splitting of the sister nucleoids. It usually
2108 extends beyond cell division, into the next cell division cycle.
2109

2110 **Figure 1 – figure supplement 3: Correlations used to calculate the relative contribution of polysome**
2111 **accumulation and cell elongation to nucleoid migration. A.** Correlation (Spearman ρ = 0.47, p-value <
2112 10^{-10}) between the rate of RplA-GFP accumulation at mid-cell ($\frac{\Delta RplA_{mid-cell}\ conc.}{\Delta T}$) and the rate of distance
2113 increase between the sister nucleoids minus the rate of cell elongation ($\frac{\Delta Distance_{nuc}}{\Delta T} - \frac{\Delta Length_{cell}}{\Delta T}$) across
2114 cells. The colormap corresponds to a Gaussian kernel density estimation. Binned data are also shown
2115 (mean ± SEM, 75 to 177 cell division cycles per bin, 9 bins in total) within the 5th-95th percentiles of the *x*-
2116 axis range. **B.** Scaled correlations (z-scores) between $\frac{\Delta RplA_{mid-cell}\ conc.}{\Delta T}$ (blue) or $\frac{\Delta Length_{cell}}{\Delta T}$ (grey) and
2117 $\frac{\Delta Distance_{nuc}}{\Delta T}$ (y-axis) during four relative time bins (1335 to 1957 cell division cycles per bin) covering the
2118 period from the end of nucleoid splitting until cell division. Shown are the Spearman correlations (ρ), all with
2119 a p-value below 10^{-6}, except for the one marked with an asterisk (p-value = 0.02).
2120
2121 **Figure 1 – figure supplement 4: Examination of the relative timing of the initiation of nucleoid**
2122 **constriction and the accumulation of polysomes at mid-nucleoid. A.** RplA-GFP and HupA-mCherry
2123 concentration (fluorescence arbitrary units) images of four representative single cells (CJW7323) growing
2124 in M9glyT and their fluorescence intensity profiles along the cell length. **B.** Demographs of the scaled RplA-
2125 GFP and HupA-mCherry concentration from 13554 *E. coli* cells grown in M9glyT. **C.** Average 1D intensity
2126 profiles of the scaled (divided by the whole cell average) RplA-GFP and HupA-mCherry concentration for
2127 12 bins of cells lengths (>1100 cells per intensity profile). **D.** Plot showing the scaled RplA-GFP and HupA-
2128 mCherry concentration in the middle of the cells for increasing cell length (~370 cells per bin, 25 bins). Cells
2129 longer than 3 μm were excluded to avoid the effects of cell constriction. The arrow and vertical dashed line
2130 indicate the minimum cell length bin with an apparent HupA-mCherry depletion at mid-cell, marking the
2131 initiation of nucleoid splitting. The error bars indicate mean ± standard error of the mean (SEM).
2132
2133 **Figure 2 – figure supplement 1: Demographs of scaled ribosome and nucleoid fluorescence for**
2134 **strains with different ribosome markers and under various nutrient conditions.** Demographs are
2135 ordered according to increasing average cell area, which scales with growth rate (Schaechter et al., 1958),
2136 from left to right and top to bottom. These demographs were constructed from snapshots of the following
2137 strains: **A.** CJW6768 (RplA-mEos2 ribosomal marker, 747 to 2446 cells per condition), **B.** CJW6769 (RpsB-
2138 mEos2 ribosomal marker, 690 to 3169 cells per condition), **C.** CJW7020 (RplA-msfGFP ribosomal marker,
2139 657 to 2432 cells per condition) and **D.** CJW7021 (RpsB-msfGFP ribosomal marker, 788 to 1950 cells per
2140 condition), using the cell length as a proxy for the cell division cycle, with the signal intensity profile sorted
2141 from the shortest newborn cells to the longest predivisional cells. Note that the demographs for the
2142 CJW6768 strain (panel A) in the nutrient conditions M9mann, M9mala, M9malt, M9mannCAAT,
2143 M9glyCAAT and M9malaCAAT are not shown here, as they are presented in Figure 2A. The nutrient
2144 abbreviations and compositions are explained in Table S1.
2145

2146

2147 **Figure 2 – figure supplement 2: Calculation of RplA-msfGFP concentration after cell curvature**
2148 **correction. A.** Average 2D RplA-msfGFP projections for short (2.5 to 3 µm – left), unconstricted cells and
2149 long (3.5 and 5.5 µm - right) constricted cells. The average RplA-msfGFP signal from 1000 sampled cells
2150 (CJW7651) is shown for each population. **B.** The 2D cell areas were divided in cylindrical sectors with a
2151 height (h) of a single pixel. The number of cylindrical sectors corresponds to the average cell length in pixels
2152 (40 and 60 sectors for the unconstricted and constricted cells, respectively). The radius (r) of each
2153 cylindrical segment corresponds to half the cell diameter for that specific cell length position. The cylindrical
2154 segments at the poles or constriction site have a smaller radius due to the curvature of the cell boundaries.
2155 The division of the cell area into cylindrical segments allowed us to calculate the volume for each segment
2156 ($V_{cylinder} = \pi\, r^2\, h$). The sum of the fluorescence per segment was corrected for the 3D curvature of the cell
2157 boundaries by dividing by the volume of the cylinder, either considering the entire cell width or different
2158 depths of view narrower than the maximal cell width. **C.** 1D profiles of the cylinder diameter are also
2159 indicative of the cell curvature at the poles and constriction site. **D.** Comparisons of the 1D average RplA-
2160 msfGFP projection between the poles before (dashed lines) or after correcting for the cell curvature (solid
2161 lines) for different depths of view (colormap). The uncorrected signal (dashed lines) corresponds to the
2162 average fluorescence along each cylindrical segment (mean of pixel intensities). The 1D profiles were
2163 normalized by dividing by the maximal RplA-msfGFP concentration at mid-cell. This correction shows that
2164 the pronounced decrease of the RplA-msfGFP fluorescence at the poles is the result of the curvature of the
2165 cell boundaries. The observed over-correction at the cell poles for larger depths of view (> 8 pixels or px)
2166 is likely due to the over-estimation of the cell segmentation mask that was determined based on the phase
2167 contrast snapshot images of cells on agarose pads.
2168
2169

2170 **Figure 3 – figure supplement 1: Analysis of the polysome and nucleoid asymmetries using fitted**
2171 **Gaussian functions. A.** Example images of RplA-GFP and HupA-mCherry fluorescence signals in a single
2172 newborn cell instance. **B.** Plots showing the Gaussian-function fitting on RplA-GFP and HupA-mCherry
2173 intensity profiles from the single cell snapshot shown in panel A. Three Gaussian functions were fitted to
2174 the RplA-GFP fluorescence in newborn cells (eq. 11 in Methods), capturing the accumulation of polysomes
2175 at mid-cell and the poles. Two Gaussian functions were fitted to the HupA-mCherry fluorescence (eq. 12 in
2176 methods) capturing the two lobes of the segregating sister nucleoids. The parameters of the fitted Gaussian
2177 functions provided information about the position (µ: mean) and the concentration (A: amplitude) of each
2178 fluorescence statistic, as well as the cell length range occupied by it (σ: standard deviation). The Gaussian
2179 area (eq. 13 in Methods) corresponds to the abundance of each macromolecule. The RplA-GFP Gaussians
2180 were fitted above the cellular background, which presumably corresponds to the uniform fluorescence of
2181 free ribosomes or ribosomal subunits. For the HupA-mCherry Gaussian fittings, the cellular background
2182 corresponds to the DNA-free cell regions. The Gaussian parameters were also used to describe the

2183 polysome asymmetries between the poles (eq. 14 in Methods) as well as the position of the nucleoid around
2184 the cell center (eq. 15 in Methods). These statistics were used in Figure 3B. **C.** Gaussian functions were
2185 also fitted to the ensemble average RplA-GFP and HupA-mCherry fluorescence (right) calculated from all
2186 the cell segmentation instances of a single cell division cycle, 0-10% from birth to division (left). **D.** The
2187 Gaussian fitting to the ensemble RplA-GFP and HupA-mCherry intensity profiles (concentration in arbitrary
2188 fluorescence units) early in the cell division cycle for the 2D projection shown in panel C (right). **E.** Plots
2189 showing the nucleoid and polysome density axial asymmetry determined using the parameters of the fitted
2190 Gaussians on the HupA-mCherry and RplA-GFP fluorescence (eq. 16 and eq. 18 in Methods). **F.** Plots
2191 showing the scaled correlations between the polysome Gaussian parameters (μ, A, and σ for each
2192 polysome accumulation) and the nucleoid density asymmetry (eq. 16 in Method; 2103 cell division cycles).
2193 Each marker corresponds to the data for a single cell division cycle (0-10% into the cell division cycle) as
2194 in panel C (right). A Gaussian kernel density estimation (KDE) was used to illustrate the density of the
2195 scatter plots (see Methods). **G.** Bar graph showing the coefficients of a linear mixed-effects model (see eq.
2196 17 in Methods) used to identify the polysome statistics that contribute to the nucleoid density asymmetry.
2197 The highly contributing polysome statistics were combined to a compound polysome statistic (eq. 18 in
2198 Methods) that describes the available DNA space between polysome accumulations. This compound
2199 statistic correlates with the nucleoid density asymmetry (eq. 16 in Methods) as shown in Figure 3F. The
2200 stars indicate the polysome statistics that most significantly correlate with the nucleoid density asymmetry
2201 (absolute coefficient above 0.3).
2202
2203 **Figure 4 – figure supplement 1: Statistics of polysome accumulation and nucleoid depletion during**
2204 **simulated cell growth.** Polysome and nucleoid dynamics were simulated for six different growth rates.
2205 The predivisional polysome and nucleoid profiles of simulated trajectories initialized from the steady state
2206 (infinite relaxation time) were used as initial conditions (D_n = 10^{-3} $\mu m^2/s$). **A.** Plot showing cell length at birth
2207 increasing with growth rate according to published measurements (Govers et al., 2024). **B.** Plot showing
2208 the dynamics of polysome accumulation (top) and nucleoid depletion (bottom) at mid-cell from birth to
2209 division for six simulated growth rates (colormap). A nucleoid depletion threshold of 0.1 arbitrary units (a.u.,
2210 dashed horizontal line) was used to determine the relative time of nucleoid splitting that is presented in
2211 Figure 4C.
2212
2213 **Figure 5 – figure supplement 1: Phenotypic effects of transcription inhibition.** Plots showing cellular
2214 parameters (instantaneous growth rate, cell area, nucleoid area, and the ratio between nucleoid area and
2215 cell area, or NC ratio) affected by the rifampicin treatment. The instantaneous growth rate was estimated
2216 using the log-transformed cell area, using a rolling window of 10 min. The black line corresponds to the
2217 averages from 1859 cell division cycles and the gray-shaded area indicates the range of one standard
2218 deviation around the mean. The two cycles of rifampicin treatment (as shown in Figure 5A) were overlaid
2219 for this plot, using the time of rifampicin addition as t = 0 min.

2220

2221 **Figure 6 – figure supplement 1: Phenotypic effects of prolonged protein over-expression from**
2222 **plasmids.** Representative phase contrast and fluorescence images of cells (CJW7798) after prolonged
2223 induction (100 μM IPTG, for 9 h and 15 min) of mTagBFP2 expression from aT7 promoter on a multi-copy
2224 plasmid.

2225

2226 **Figure 7 – figure supplement 1: Phenotypic of effects of cell growth under A22 and cephalexin**
2227 **treatment.** Representative phase contrast and fluorescence images of cells (CJW7323) treated with A22
2228 (4 μg/mL) alone or with both A22 (4 μg/mL) and cephalexin (50 μg/mL) for 130 min.

2229

2230

2231 **Movie legends**

2232 **Movie S1: Example time-lapse sequence showing ribosome and nucleoid dynamics during cell**
2233 **growth under steady state condition in a microfluidic channel.** Shown are corresponding inverted
2234 phase contrast signal, RplA-GFP signal, HupA-mCherry signal, cell contours (based on phase contrast
2235 signals) and nucleoid contours (based on nucleoid signal segmentation) of *E. coli* cells (CJW7323) grown
2236 in a microfluidic channel supplemented with M9gluCAAT. The white circles indicate the centroid of the cell
2237 segmentation masks and the extending lines indicate the tracked cell traces.

2238

2239 **Movie S2: Video showing the average subcellular distribution of ribosome and nucleoid signals**
2240 **from birth to division.** Shown are 2D average RplA-GFP (top) and HupA-mCherry (bottom) projections
2241 from birth to division, with corresponding average intensity profiles (right). The cell projections are oriented
2242 from the old pole on the left to the new pole on the right. The average cell contour is also drawn. Ensemble
2243 data from 4122 division cycles of CJW7323 cells growing in M9gluCAAT are shown.

2244

2245 **Movie S3: Video showing simulated 1D profiles of polysome and nucleoid concentration during**
2246 **slow and fast cell growth.** Simulations during slow (left) and fast (right) growth are shown. The simulations
2247 were initialized from the equilibrium configuration, with a compact symmetric nucleoid ($D_n = 10^{-3}$ μm^2/sec)
2248 at the cell center.

2249

2250 **Movie S4: Video showing the effects of rifampicin addition on cell growth, ribosome signal**
2251 **heterogeneity, nucleoid segregation, and nucleoid compaction.** Examples of five microfluidic channels
2252 showing the corresponding inverted phase contrast, RplA-GFP and HupA-mCherry signals (from left to
2253 right) of cells (CJW7323) growing within microfluidic channels. Rifampicin was added at 120 and 720 min.
2254 Each antibiotic treatment lasted 120 min.

2255

2256 **Movie S5: Video showing the effects of ectopic polysome formation on nucleoid dynamics over**
2257 **time.** The RplA-GFP and HupA-mCherry fluorescence normalized (norm.) by the average cell fluorescence
2258 are shown, together with their corresponding phase contrast image, for multiple cells (CJW7798) in
2259 succession following induction of mTagBFP2 expression from a T7 promoter on a multi-copy plasmid. The
2260 scale bar indicates 1 μm, and the time since cell birth is shown in minutes. The cell contours indicate the
2261 boundaries of the cell masks obtained by cell segmentation of the corresponding phase contrast images.
2262
2263 **Movie S6 Video showing how the loss of cell width confinement due to cephalexin and A22**
2264 **treatment affects ribosome and nucleoid distributions over time.** Fluorescence images of RplA-GFP
2265 and HupA-mCherry fluorescence (fluor.) normalized by the average cellular fluorescence images, together
2266 with their corresponding phase contrast images, are shown for cells (CJW7323) following treatment with
2267 A22 (4 μg/mL) and cephalexin (50 μm/mL). The scale bar indicates 1 μm. The time since drug addition is
2268 shown in minutes.
2269
2270
2271 **Supplementary tables**
2272 **Table S1. Growth medium abbreviation and composition.**

Abbreviation	Composition
M9acet	1x M9 salts, 0.2% acetate (sodium salt)
M9acetCAAT	1x M9 salts, 0.2% acetate, 0.1% casamino acids, 1μg/mL thiamine
M9fuc	1x M9 salts, 0.2% fucose
M9fucCAAT	1x M9 salts, 0.2% fucose, 0.1% casamino acids, 1μg/mL thiamine
M9fum	1x M9 salts, 0.2% fumarate (disodium salt)
M9fumCAAT	1x M9 salts, 0.2% fumarate, 0.1% casamino acids, 1μg/mL thiamine
M9GlcNac	1x M9 salts, 0.2% N-acetylglucosamine
M9GlcNacCAAT	1x M9 salts, 0.2% N-acetylglucosamine, 0.1% casamino acids, 1μg/mL thiamine
M9glu	1x M9 salts, 0.2% glucose
M9gluCAAT	1x M9 salts, 0.2% glucose, 0.1% casamino acids, 1μg/mL thiamine
M9gly	1x M9 salts, 0.2% glycerol
M9glyCAAT	1x M9 salts, 0.2% glycerol, 0.1% casamino acids, 1μg/mL thiamine
M9Lala	1x M9 salts, 0.2% L-alanine
M9LalaCAAT	1x M9 salts, 0.2% L-alanine, 0.1% casamino acids, 1μg/mL thiamine
M9Lara	1x M9 salts, 0.2% L-arabinose
M9LaraCAAT	1x M9 salts, 0.2% L-arabinose, 0.1% casamino acids, 1μg/mL thiamine
M9mala	1x M9 salts, 0.2% malate (sodium salt)
M9malaCAAT	1x M9 salts, 0.2% malate, 0.1% casamino acids, 1μg/mL thiamine
M9malt	1x M9 salts, 0.2% maltose
M9maltCAAT	1x M9 salts, 0.2% maltose, 0.1% casamino acids, 1μg/mL thiamine
M9mann	1x M9 salts, 0.2% mannose
M9mannCAAT	1x M9 salts, 0.2% mannose, 0,1% casamino acids, 1μg/mL thiamine
M9pyr	1x M9 salts, 0.2% pyruvate (sodium salt)
M9pyrCAAT	1x M9 salts, 0.2% pyruvate, 0,1% casamino acids, 1μg/mL thiamine
M9sorb	1x M9 salts, 0.2% sorbitol
M9sorbCAAT	1x M9 salts, 0.2% sorbitol, 0,1% casamino acids, 1μg/mL thiamine
M9succ	1x M9 salts, 0.2% succinate (disodium salt)
M9succCAAT	1x M9 salts, 0.2% succinate, 0,1% casamino acids, 1μg/mL thiamine
M9treh	1x M9 salts, 0.2% trehalose
M9trehCAAT	1x M9 salts, 0.2% trehalose, 0,1% casamino acids, 1μg/mL thiamine
M9xyl	1x M9 salts, 0.2% xylose
M9xylCAAT	1x M9 salts, 0.2% xylose, 0,1% casamino acids, 1μg/mL thiamine

2273
2274

2275 **Table S2: *Escherichia coli* strains used in this study.**

Strain	Genotype	Source
MG1655	*E. coli* MG1655 (F-lambda- *ilvG- rfb-50 rph-1*)	(Guyer et al., 1981; Jensen, 1993)
MG1655 (DE3)	*E. coli* MG1655 (DE3)	Kind gift from Dr K. Prather (Massachusetts Institute of Technology), (Tseng et al., 2010b)
CJW5158	*E. coli* BW25113 *hupA*::*hupA-mcherry-frt-kanR-frt*	(Gray et al., 2019)
CJW6723	*E. coli* MG1655 Δ*lacZYA*::P_{lac}*-egfp-μNS hupA*:*hupA-mcherry*	(Gray et al., 2019)
CJW6768	*E. coli* MG1655 *rplA*::*rplA-meos2*	(Sanamrad et al., 2014)
CJW6769	*E. coli* MG1655 *rspB*::*rpsB-meos2*	(Sanamrad et al., 2014)
CJW7019	*E. coli* MG1655 *rplA*::*rplA-msfgfp-frt-kanR-frt*	(Gray et al., 2019)
CJW7020	*E. coli* MG1655 *rplA*::*rplA-msfgfp*	(Gray et al., 2019)
CJW7021	*E. coli* MG1655 *rpsB*::*rpsB-msfgfp*	(Gray et al., 2019)
CJW7144	*E. coli* MG1655 Δ*lacZYA*::P_{lac}*-mcherry-μNS-frt-kanR-frt*	This study
CJW7145	*E. coli* MG1655 Δ*lacZYA*::P_{lac}*-mcherry-μNS-frt-kanR-frt rplA*::*rplA-msfgfp*	This study
CJW7323	*E. coli* MG1655 *rplA*::*rplA-msfgfp hupA*::*hupA-mcherry*	(Xiang et al., 2021)
CJW7466	*E. coli* MG1655 (DE3) *hupA*:*hupA-mcherry*	This study
CJW7651	*E. coli* MG1655 Δ*lacZYA*::P_{lac}*-mcherry-μNS rplA*::*rplA-msfgfp*	This study
CJW7766	*E. coli* MG1655 (DE3) *hupA*:*hupA-mcherry rplA*::*rplA-msfgfp-frt-kanR-frt*	This study
CJW7798	*E. coli* MG1655 (DE3) *hupA*:*hupA-mcherry rplA*::*rplA-msfgfp-frt-kanR-frt* | *pET28:mTagBFP2-CmR*	This study

2276

2277 **Table S3: Plasmids used in this study.**

Plasmid name	Relevant genetic elements	Source
pKD13	*frt-kanR-frt-R6Kori-ampR*	(Datsenko and Wanner, 2000)
pKD46	*araC-bet-exo-A101(Ts)ori-ampR*	(Datsenko and Wanner, 2000)
pCP20	*cmR-A101(Ts)ori-ampR-flp-λ-repressor(Ts)*	(Datsenko and Wanner, 2000)
pER12	*pBAD322A-gfp-μNS*	Kind gift from Dr A. Janakiraman (City College of New York), (Broering et al., 2005)
pER12-mcherry	*pBAD322A-mcherry-μNS*	This study
pAPG1	*attB-pBAD322A-mcherry-μNS-attB-kanR-ColE1ori*	This study
pSB3C5-proA-B0032-E0051	*PproA-lacZα-GFP-p15Aori-cmR*	(Davis et al., 2011)
pET28:GFP	*PT7-lacO-GFP-kanR-pMB1ori-lacI*	(Shis and Bennett, 2013)
pBAD:TagBFP2	*araC-ParaBAD-mTagBFP2-ampR-pBAD322ori*	(Subach et al., 2011)
pET28:mTagBFP2	*PT7-lacO-mTagBFP2-kanR-pMB1ori-lacI*	This study
pET28:mTagBFP2-CmR	*PT7-lacO-mTagBFP2-cmR-pMB1ori-lacI*	This study

2278

2279

2280 **Table S4: DNA oligonucleotides used in this study.**

Oligo name	Sequence	Source
ER12-MCR-fwd	5' CTCCATACCCGTTTTTTTGGGCTAGCAGGAGGAATTCATGGTGAGCAAGGGCG AGGAG 3'	This study
ER12-MCR-rev2	5' CACTGGAGGAGCCTGCTTTTTTGTACAAACTTGTTGACTTGTACAGCTCGTCCA TG 3'	This study
μNSmCherry fwd	5' CACAGGTTGCTCCGGGCTATGAAATAGAAAAATGAATCCGTTGAAGCCTGATC GATGCATAATGTGCC 3'	This study
μNSmCherry rev	5' AGCTCCAGCCTACACAGAGTTTGTAGAAACGCAAAAAG 3'	This study
FRT_KanR fwd	5' GTTTCTACAAACTCTGTGTAGGCTGGAGCTGC 3'	This study
FRT_KanR Rev	5' TTAAAGGTATTAAAAACAACTTTTTGTCTTTTTACCTTCCCGTTTCGCTC CTGTCAAACATGAGAATTAATTCC 3'	This study
ColE1 fwd	5' GAGCGAAACGGGAAGGTAAAAAGACAAAAAGTTGTTTTTAATACCTTTAA CGTTCCACTGAGCGTC 3'	This study
ColE1 rev	5' CAGGCTTCAACGGATTCATTTTTCTATTTCATAGCCCGGAGCAACCTGTG GGTTATCCACAGAATCAGG 3'	This study
pAPG1 seq1	5' GATCAAGCAGAGGCTGAAG 3'	This study

pAPG1 seq2	5' CCAGGCATCAAATTAAGC 3'	This study
pAPG1 seq3	5' TCTACGTGTTCCGCTTCC 3'	This study
pAPG1 seq4	5' TTGAAGCCTGATCGATGC 3'	This study
pAPG1 seq5	5' AAGATTAGCGGATCCTACC 3'	This study
lacZYA_redμNS fwd	5' TATGTTGTGTGGAATTGTGAGCGGATAACAATTTCACACAGGAAACAGCT ATGGTGAGCAAGGGCGA 3'	This study
lacZYA_redμNS rev	5' CAATTTTTATAATTTAAACTGACGATTCAACTTTATAATCTTTGAAATAA GGATCCGTCGACCTGCAG 3'	This study
LacI fwd	5' GGCCGATTCATTAATGCAGCTGGC 3'	This study
CynX rev	5' GGCCTGATAAGCGCAGCGTATC 3'	This study
mCherry rev	5' GGTGCTTCACGTAGGCCTTGG 3'	This study
KanR fwd	5' CGGAGAACCTGCGTGCAATCC 3'	This study
mTagBFP2 fwd	5' CGGAGCTCGAATTCGGATCCTTAATTAAGCTTGTGCCCCAGTTTG 3'	This study
mTagBFP2 fwd	5' CTTTAAGAAGGAGATATACCATGAGCGAGCTGATTAAGGAGAAC 3'	This study
pET28_one fwd	5' TCCTTAATCAGCTCGCTCATGGTATATCTCCTTCTTAAAGTTAAAC 3'	This study
pET28_one rev	5' GGATAACCGTATTACCGCCTTTGAGTGAGCTGATACCG 3'	This study
pET28_two fwd	5' AGCGGTATCAGCTCACTCAAAGGCGGTAATACGGTTATCC 3'	This study
pET28_two rev	5' TGGGGCACAAGCTTAATTAAGGATCCGAATTCGAGCTCC 3'	This study
pET28mTagBFP2 fwd	5' CTTAGTGACTCGAATTCGCGCGCCAATCCGGATATAGTTCC 3'	This study
pET28mTagBFP2 rev	5' ACTTTCTGGCTGGATGATGGACGTGAGTTTTCGTTCCACTG 3'	This study
cmR fwd	5' AGTGGAACGAAAACTCACGTCCATCATCCAGCCAGAAAGTG 3'	This study
cmR rev	5' GAACTATATCCGGATTGGCGCGCGAATTCGAGTCACTAAGG 3'	This study

Table S5: Chemicals used in this study.

Chemical	Source	Catalog number
Agarose	AmericanBio	Cat#AB00972-00500
4',6-diamidine-2′-phenylindole (DAPI), dihydrochloride fluorescent dye	Thermo Fisher Scientific	Cat#D1306
Isopropyl β-D-1-thiogalactopyranoside (IPTG)	Sigma Aldrich	Cat#I5502
Rifampicin	Sigma Aldrich	Cat#R3501
Cephalexin	Sigma Aldrich	Cat#C4895
A22	Sigma Aldrich	Cat#SML0471
4',6-Diamidine-2-phenylindole dihydrochloride (DAPI)	Thermo Fisher Scientific	Cat#D1306

Table S6: Software used in this study.

Program / library / script	Package	Source
Oufti	www.oufti.org	(Paintdakhi et al., 2016)
MATLAB	www.mathworks.com	Mathworks
Python	www.python.org	Python Software Foundation
Numpy	www.numpy.org	(Harris et al., 2020)
Scipy	www.scipy.org	(Virtanen et al., 2020)
Pytorch	www.pytorch.org	(Paszke et al., 2019)
Scikit-image	www.scikit-image.org	(Van Der Walt et al., 2014)
Scikit-learn	www.scikit-learn.org/stable/	(Pedregosa et al., 2012)
Statsmodels	www.statsmodels.org/stable/index.html	(Seabold and Perktold, 2010)
Shapely	www.pypi.org/project/shapely/	(Gillies, Sean et al., 2023)
Matplotlib	www.matplotlib.org	(Hunter, 2007)
Seaborn	www.seaborn.pydata.org	(Waskom, 2021)
Pandas	www.pandas.pydata.org	(McKinney, 2010)
Python	Omnipose neural network	(Cutler et al., 2022)
MATLAB	SuperSegger	(Stylianidou et al., 2016)
Python	Unet neural network	(Wiktor et al., 2021; Zhou et al., 2020)

snapshots_analysis_UNET_ghv.py	Snapshot image analysis (from UNET masks) – custom Python class	This study (www.github.com/JacobsWagnerLab/published/tree/master/Papagiannakis_2024)
snapshots_analysis_OUFTI_GrayGovers_ghv.py	Snapshot image analysis (from Oufti masks) – custom Python class	This study (www.github.com/JacobsWagnerLab/published/tree/master/Papagiannakis_2024)
snapshots_analysis_functions.py	Extraction of fluorescence and morphology statistics from cell snapshots – custom Python functions	This study (www.github.com/JacobsWagnerLab/published/tree/master/Papagiannakis_2024)
microfluidics_segmentation_ghv.py	Cell segmentation and tracking from time-lapse images in microfluidics – custom Python class	This study (www.github.com/JacobsWagnerLab/published/tree/master/Papagiannakis_2024)
microfluidics_analysis_functions_ghv.py	Extraction of fluorescence and morphology statistics from time-lapse images in microfluidics – custom Python functions	This study (www.github.com/JacobsWagnerLab/published/tree/master/Papagiannakis_2024)
Omnipose_to_python_ghv.py	Extraction of segmentation masks and tracked lineages from Omnipose/SuperSegger to Python for further analysis	This study (www.github.com/JacobsWagnerLab/published/tree/master/Papagiannakis_2024)
Otsu_phase_segmentation_ghv.py	Cell segmentation and tracking using Otsu thresholding (Otsu, 1979)	This study (www.github.com/JacobsWagnerLab/published/tree/master/Papagiannakis_2024)
Biviriate_medial_axis_estimation.py	Function that draws the medial axis in randomly oriented cells on agarose pads	This study (www.github.com/JacobsWagnerLab/published/tree/master/Papagiannakis_2024)
LoG_adaptive_image_filter.py	Image filter that applies relative and local thresholding to segment fluorescence objects and particles	This study (www.github.com/JacobsWagnerLab/published/tree/master/Papagiannakis_2024)
Microfluidics_segmentation_and_tracking_example.pdf	Example for cell segmentation and tracking in microfluidics	This study (www.github.com/JacobsWagnerLab/published/tree/master/Papagiannakis_2024)
Analysis_of_cell_morphology_and_fluorescence_in_microfluidics.pdf	Example for the extraction of fluorescence and morphology statistics from time-lapse images in microfluidics	This study (www.github.com/JacobsWagnerLab/published/tree/master/Papagiannakis_2024)
Analysis_of_cell_morphology_and_fluorescence_in_agarose_pads.pdf	Example for the extraction of fluorescence and morphology statistics from cell snapshots	This study (www.github.com/JacobsWagnerLab/published/tree/master/Papagiannakis_2024)
Example_of_using_Otsu_based_segmentation_ghv.pdf	Example for the segmentation of antibiotic-treated cells using the Otsu threshold	This study (www.github.com/JacobsWagnerLab/published/tree/master/Papagiannakis_2024)
tune_diffusion.ipynb	Simulations of the minimal reaction-diffusion model that describes nucleoid segregation in *E. coli*.	This study (https://github.com/qiweiyuu/polysome)

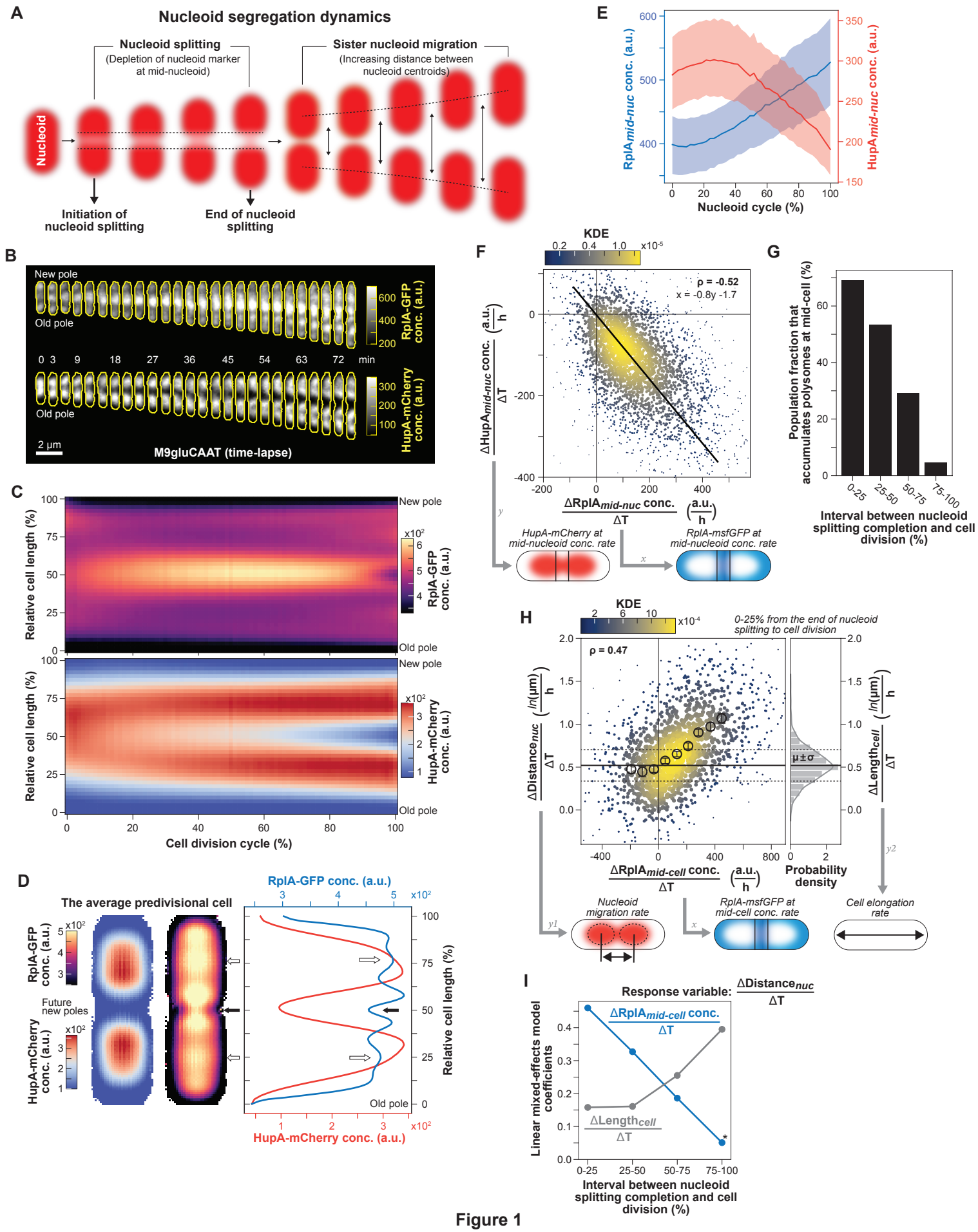
A
Nucleoid segregation dynamics
Nucleoid splitting
(Depletion of nucleoid marker at mid-nucleoid)
Sister nucleoid migration
(Increasing distance between nucleoid centroids)
Nucleoid
Initiation of nucleoid splitting
End of nucleoid splitting
B
New pole
Old pole
RplA-GFP conc. (a.u.)
0 3 9 18 27 36 45 54 63 72 min
HupA-mCherry conc. (a.u.)
2 µm
M9gluCAAT (time-lapse)
C
Relative cell length (%)
New pole
Old pole
RplA-GFP conc. (a.u.)
HupA-mCherry conc. (a.u.)
Cell division cycle (%)
D
The average predivisional cell
RplA-GFP conc. (a.u.)
HupA-mCherry conc. (a.u.)
Future new poles
Relative cell length (%)
Old pole
E
RplAmid-nuc conc. (a.u.)
HupAmid-nuc conc. (a.u.)
Nucleoid cycle (%)
F
KDE
ρ = -0.52
x = -0.8y -1.7
ΔHupAmid-nuc conc. / ΔT (a.u./h)
ΔRplAmid-nuc conc. / ΔT (a.u./h)
HupA-mCherry at mid-nucleoid conc. rate
RplA-msfGFP at mid-nucleoid conc. rate
G
Population fraction that accumulates polysomes at mid-cell (%)
0-25
25-50
50-75
75-100
Interval between nucleoid splitting completion and cell division (%)
H
KDE
0-25% from the end of nucleoid splitting to cell division
ρ = 0.47
ΔDistancenuc / ΔT (ln(µm)/h)
ΔLengthcell / ΔT (ln(µm)/h)
ΔRplAmid-cell conc. / ΔT (a.u./h)
Probability density
Nucleoid migration rate
RplA-msfGFP at mid-cell conc. rate
Cell elongation rate
I
Response variable: ΔDistancenuc / ΔT
ΔRplAmid-cell conc. / ΔT
ΔLengthcell / ΔT
Linear mixed-effects model coefficients
Interval between nucleoid splitting completion and cell division (%)

Figure 1

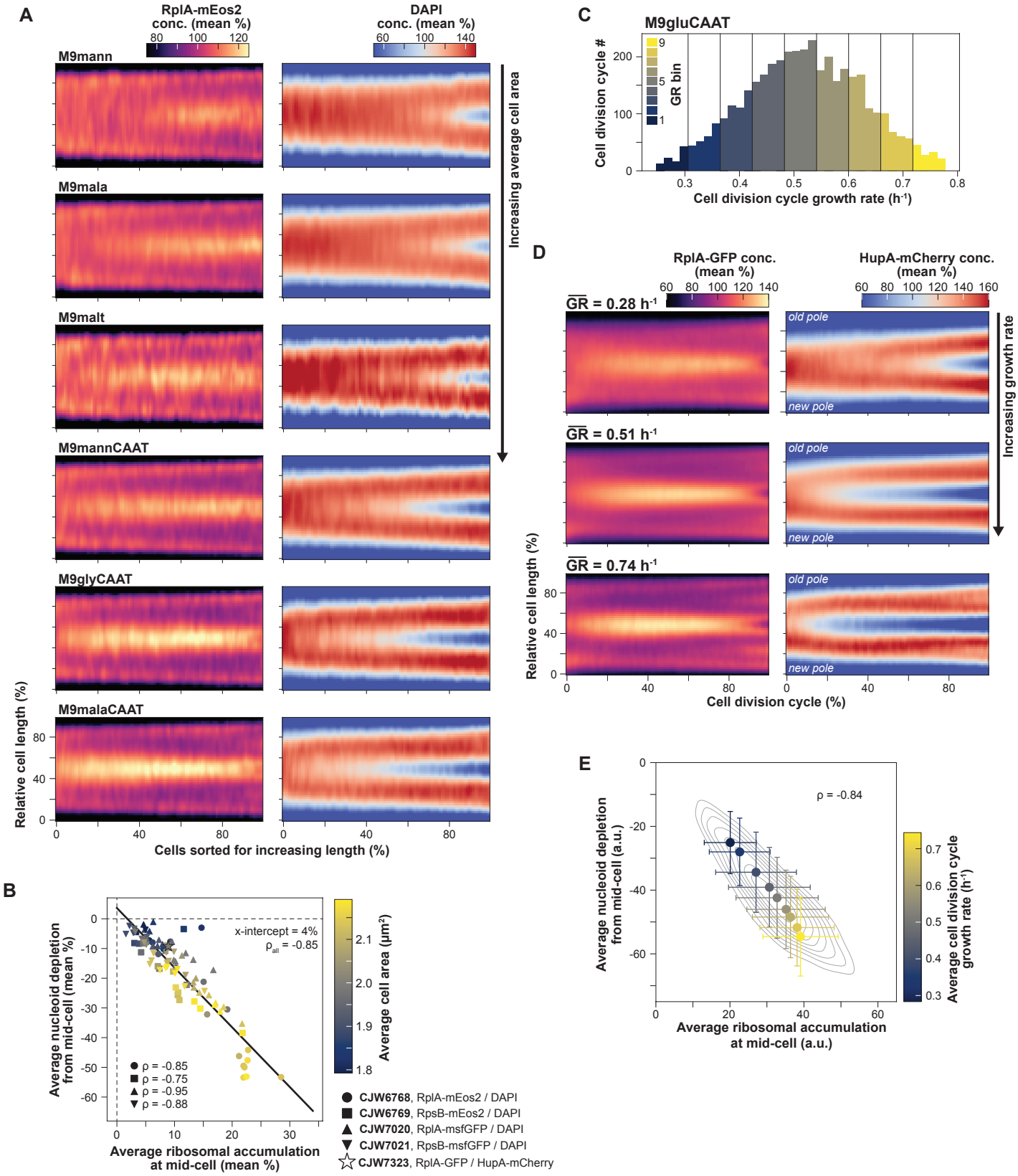
A
RplA-mEos2 conc. (mean %)
80 100 120
DAPI conc. (mean %)
60 100 140
M9mann
M9mala
M9malt
M9mannCAAT
M9glyCAAT
M9malaCAAT
Increasing average cell area
Relative cell length (%)
Cells sorted for increasing length (%)
B
Average nucleoid depletion from mid-cell (mean %)
Average ribosomal accumulation at mid-cell (mean %)
x-intercept = 4%
ρall = -0.85
ρ = -0.85
ρ = -0.75
ρ = -0.95
ρ = -0.88
Average cell area (μm²)
CJW6768, RplA-mEos2 / DAPI
CJW6769, RpsB-mEos2 / DAPI
CJW7020, RplA-msfGFP / DAPI
CJW7021, RpsB-msfGFP / DAPI
CJW7323, RplA-GFP / HupA-mCherry
C
M9gluCAAT
Cell division cycle #
GR bin
Cell division cycle growth rate (h⁻¹)
D
RplA-GFP conc. (mean %)
HupA-mCherry conc. (mean %)
GR = 0.28 h⁻¹
GR = 0.51 h⁻¹
GR = 0.74 h⁻¹
old pole
new pole
Increasing growth rate
Relative cell length (%)
Cell division cycle (%)
E
ρ = -0.84
Average nucleoid depletion from mid-cell (a.u.)
Average ribosomal accumulation at mid-cell (a.u.)
Average cell division cycle growth rate (h⁻¹)

Figure 2

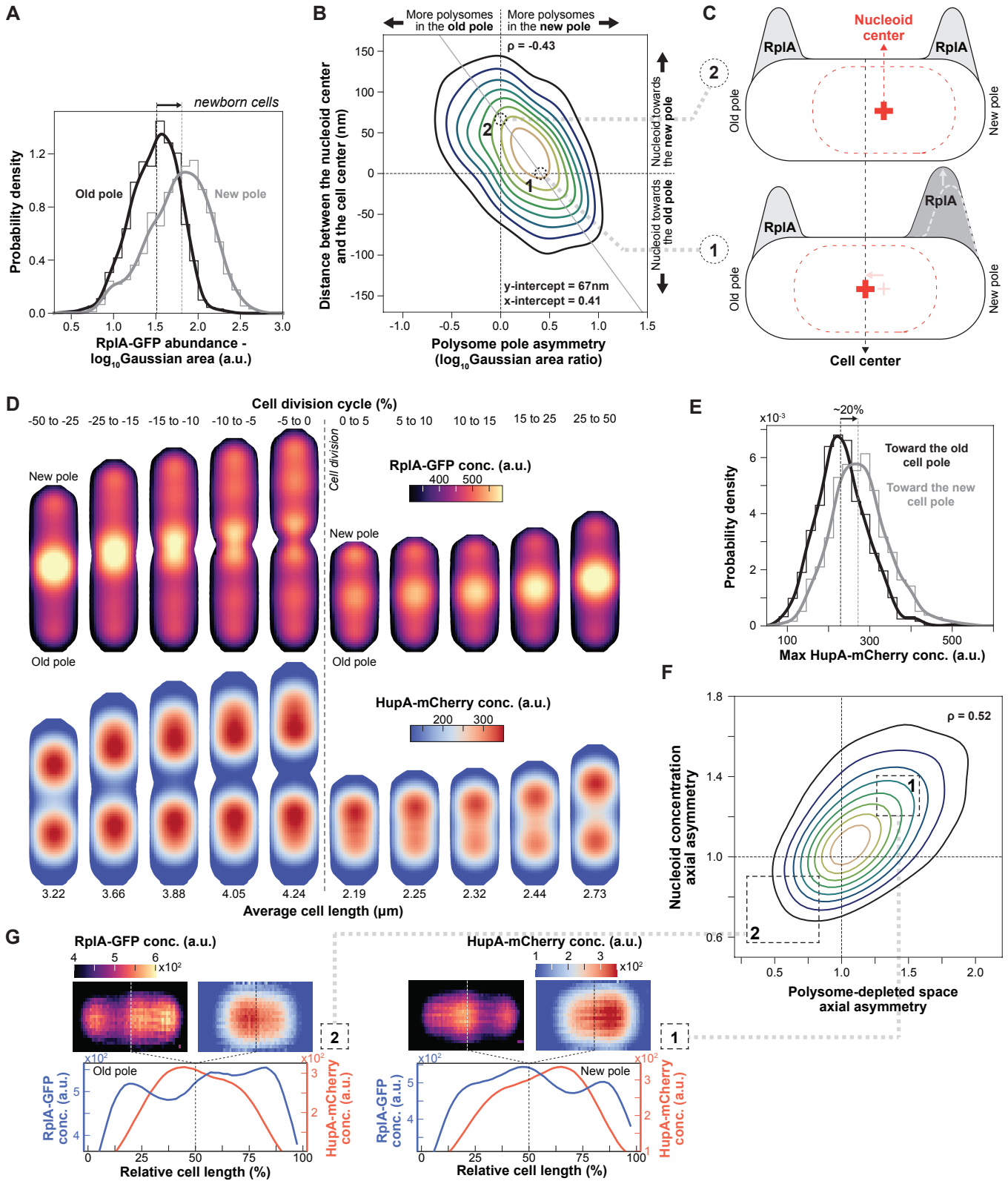
A
newborn cells
Old pole
New pole
Probability density
RplA-GFP abundance - log10Gaussian area (a.u.)
B
More polysomes in the old pole
More polysomes in the new pole
ρ = -0.43
Distance between the nucleoid center and the cell center (nm)
Nucleoid towards the new pole
Nucleoid towards the old pole
y-intercept = 67nm
x-intercept = 0.41
Polysome pole asymmetry (log10Gaussian area ratio)
C
Nucleoid center
RplA
Old pole
New pole
Cell center
D
Cell division cycle (%)
-50 to -25
-25 to -15
-15 to -10
-10 to -5
-5 to 0
0 to 5
5 to 10
10 to 15
15 to 25
25 to 50
Cell division
RplA-GFP conc. (a.u.)
HupA-mCherry conc. (a.u.)
Average cell length (µm)
E
~20%
Toward the old cell pole
Toward the new cell pole
Probability density
Max HupA-mCherry conc. (a.u.)
F
ρ = 0.52
Nucleoid concentration axial asymmetry
Polysome-depleted space axial asymmetry
G
RplA-GFP conc. (a.u.)
HupA-mCherry conc. (a.u.)
Old pole
New pole
Relative cell length (%)

Figure 3

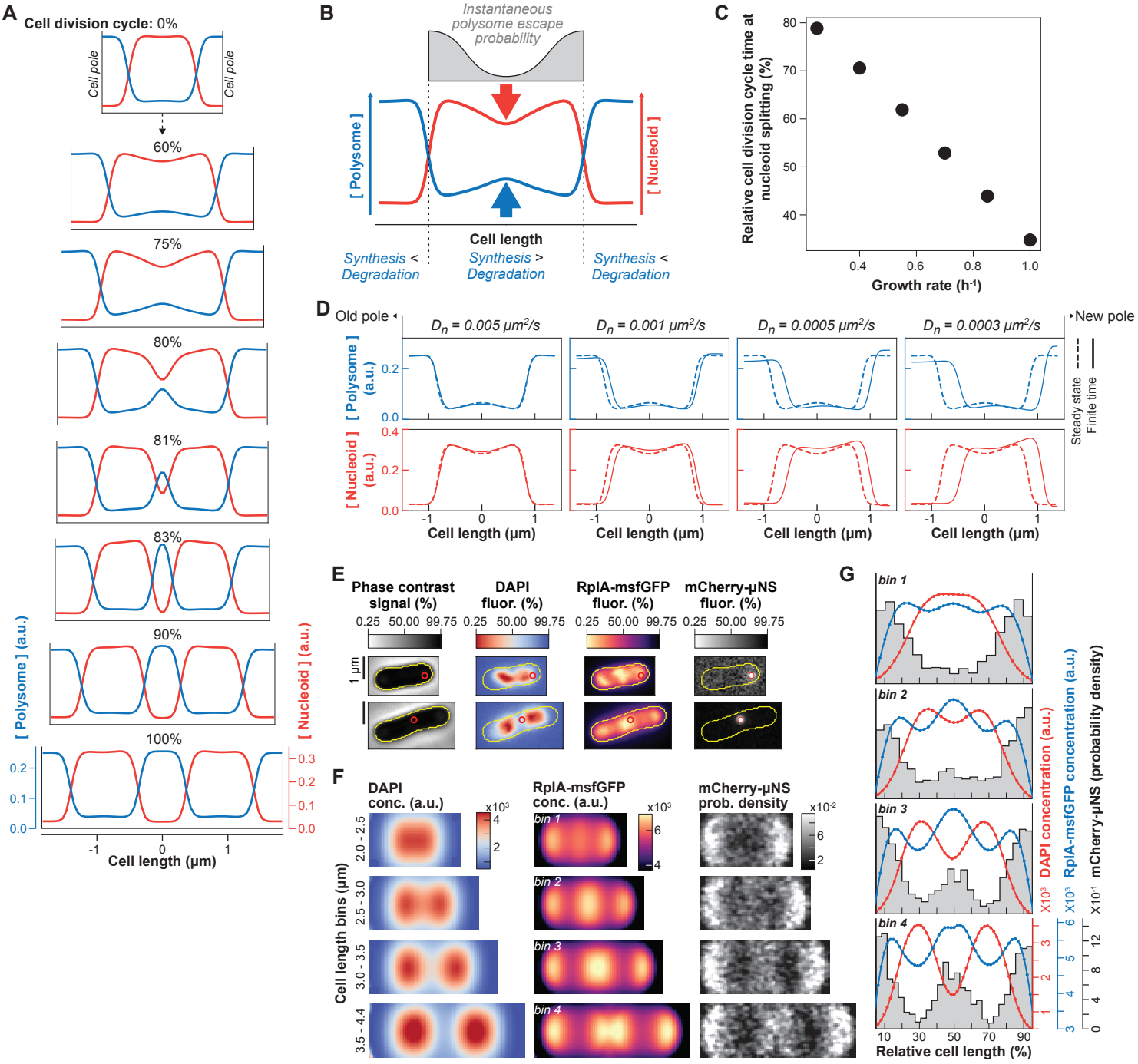
A
Cell division cycle: 0%
Cell pole
Cell pole
60%
75%
80%
81%
83%
90%
100%
[Polysome] (a.u.)
[Nucleoid] (a.u.)
Cell length (µm)
B
Instantaneous polysome escape probability
[Polysome]
[Nucleoid]
Cell length
Synthesis < Degradation
Synthesis > Degradation
Synthesis < Degradation
C
Relative cell division cycle time at nucleoid splitting (%)
Growth rate (h-1)
D
Old pole
New pole
Dn = 0.005 µm2/s
Dn = 0.001 µm2/s
Dn = 0.0005 µm2/s
Dn = 0.0003 µm2/s
[Polysome] (a.u.)
[Nucleoid] (a.u.)
Steady state
Finite time
Cell length (µm)
E
Phase contrast signal (%)
DAPI fluor. (%)
RplA-msfGFP fluor. (%)
mCherry-µNS fluor. (%)
0.25 50.00 99.75
1 µm
F
DAPI conc. (a.u.)
RplA-msfGFP conc. (a.u.)
mCherry-µNS prob. density
Cell length bins (µm)
2.0 - 2.5
2.5 - 3.0
3.0 - 3.5
3.5 - 4.4
bin 1
bin 2
bin 3
bin 4
G
bin 1
bin 2
bin 3
bin 4
DAPI concentration (a.u.)
RplA-msfGFP concentration (a.u.)
mCherry-µNS (probability density)
Relative cell length (%)

Figure 4

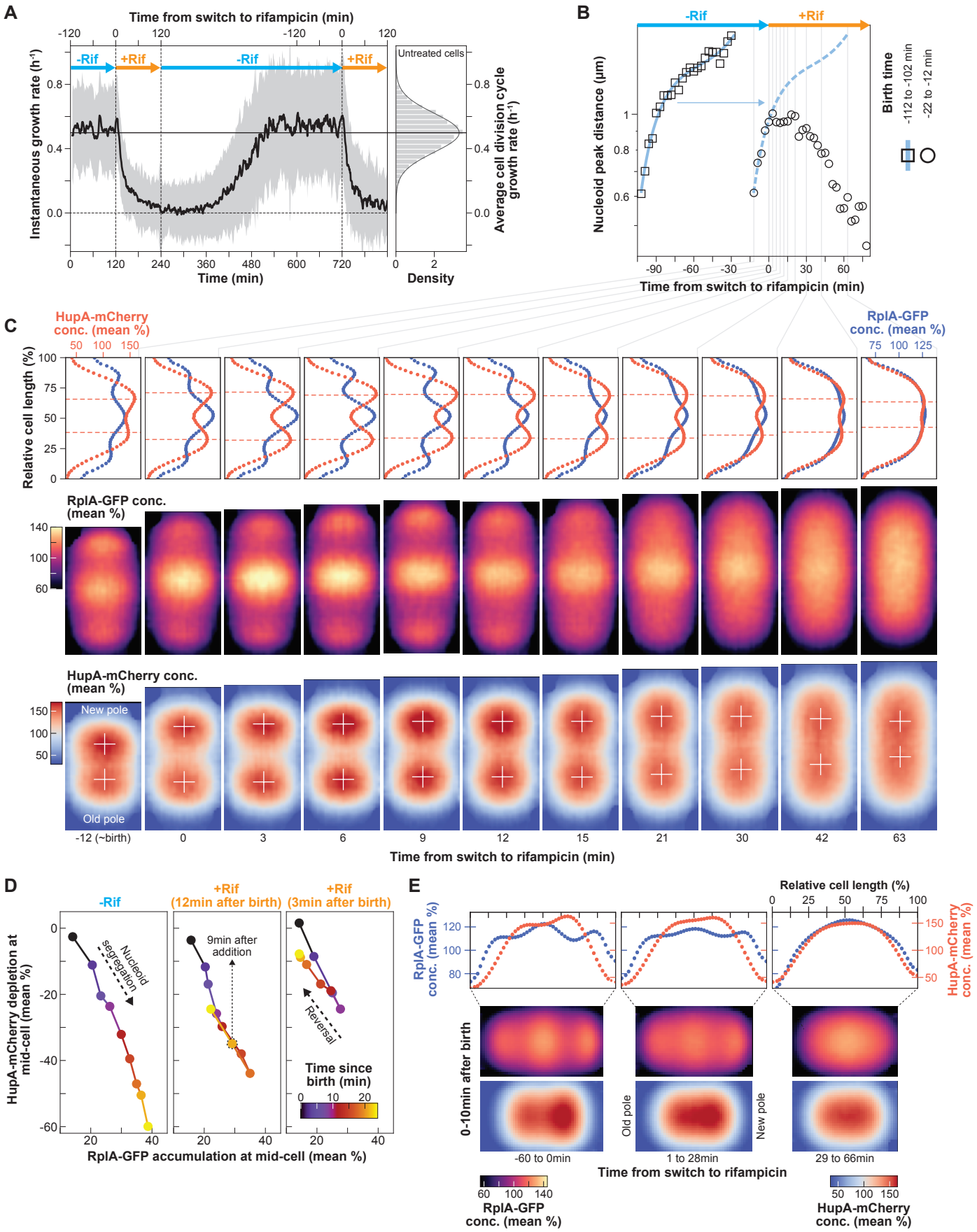
A
Time from switch to rifampicin (min)
-Rif
+Rif
Instantaneous growth rate (h-1)
Time (min)
Untreated cells
Density
Average cell division cycle growth rate (h-1)
B
Nucleoid peak distance (µm)
Time from switch to rifampicin (min)
Birth time
-112 to -102 min
-22 to -12 min
C
HupA-mCherry conc. (mean %)
RplA-GFP conc. (mean %)
Relative cell length (%)
RplA-GFP conc. (mean %)
HupA-mCherry conc. (mean %)
New pole
Old pole
-12 (~birth)
Time from switch to rifampicin (min)
D
-Rif
+Rif (12min after birth)
+Rif (3min after birth)
HupA-mCherry depletion at mid-cell (mean %)
Nucleoid segregation
9min after addition
Reversal
Time since birth (min)
RplA-GFP accumulation at mid-cell (mean %)
E
Relative cell length (%)
RplA-GFP conc. (mean %)
HupA-mCherry conc. (mean %)
0-10min after birth
Old pole
New pole
-60 to 0min
1 to 28min
29 to 66min
Time from switch to rifampicin
RplA-GFP conc. (mean %)
HupA-mCherry conc. (mean %)

Figure 5

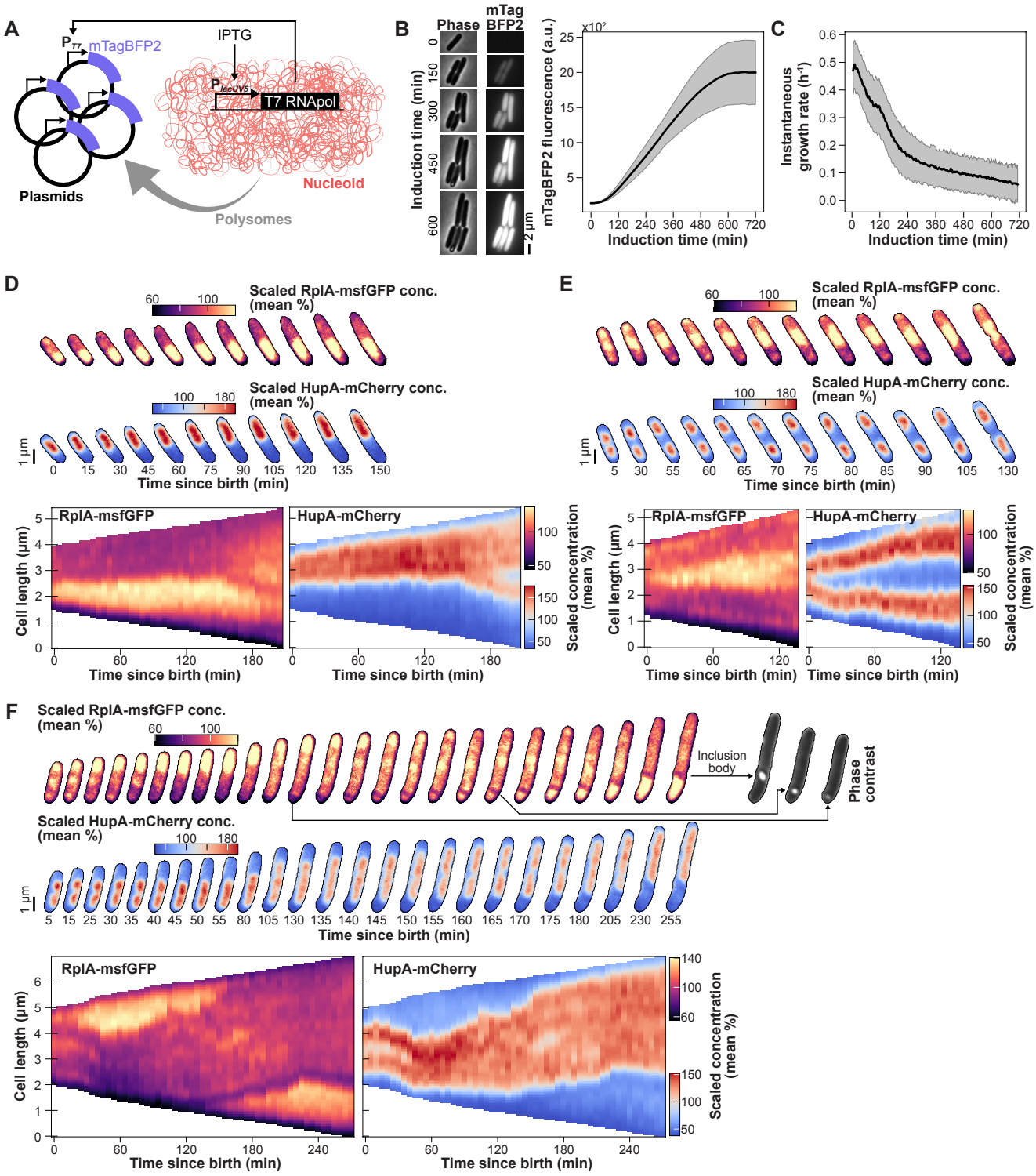
A
IPTG
mTagBFP2
T7 RNApol
Plasmids
Nucleoid
Polysomes
B
Phase
mTag BFP2
Induction time (min)
mTagBFP2 fluorescence (a.u.)
Induction time (min)
C
Instantaneous growth rate (h⁻¹)
Induction time (min)
D
Scaled RplA-msfGFP conc. (mean %)
Scaled HupA-mCherry conc. (mean %)
Time since birth (min)
RplA-msfGFP
HupA-mCherry
Cell length (µm)
Scaled concentration (mean %)
E
F
Inclusion body
Phase contrast

Figure 6

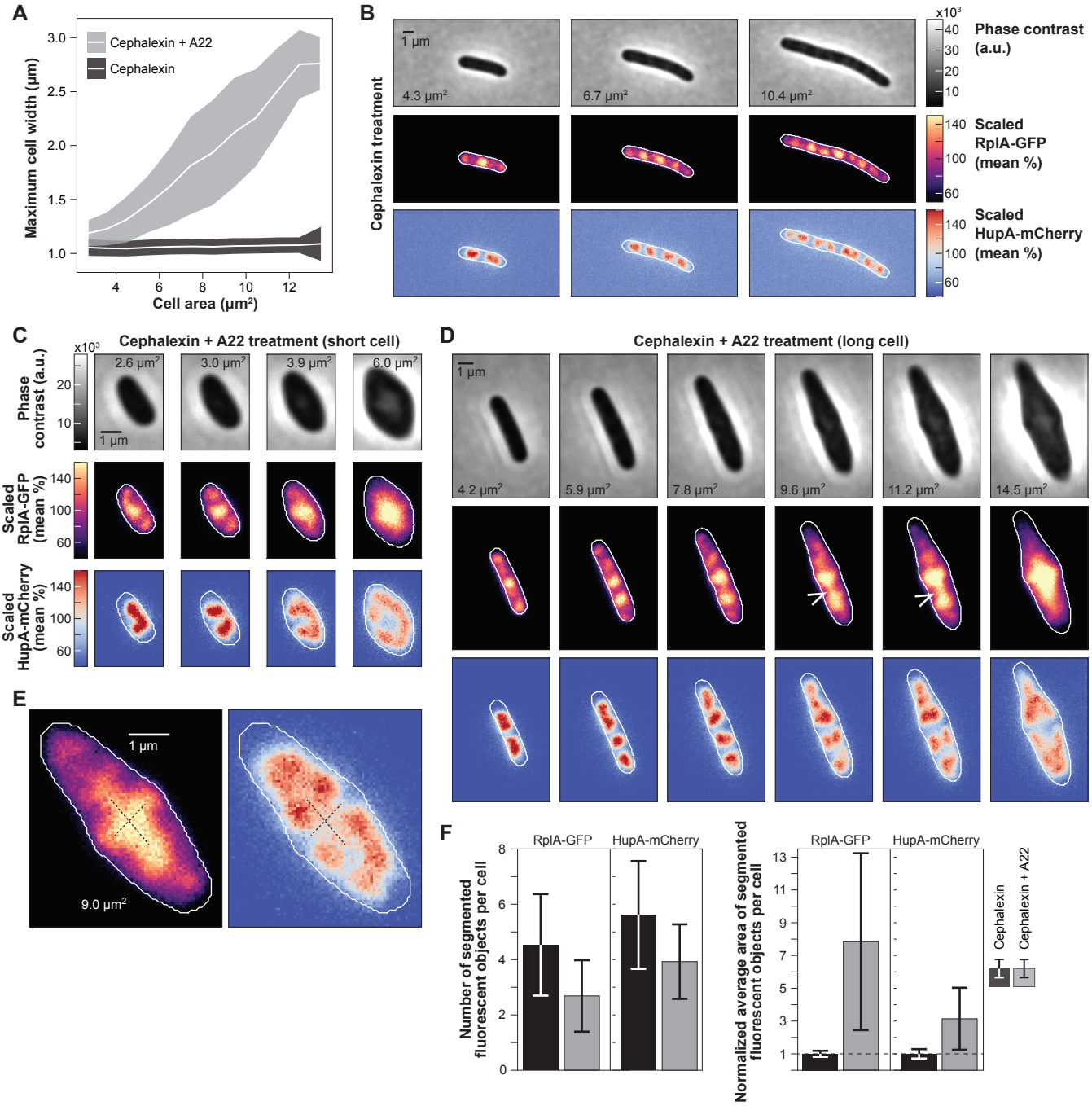
A
Cephalexin + A22
Cephalexin
Maximum cell width (µm)
Cell area (µm²)
B
Cephalexin treatment
1 µm
4.3 µm²
6.7 µm²
10.4 µm²
x10³
Phase contrast (a.u.)
Scaled RplA-GFP (mean %)
Scaled HupA-mCherry (mean %)
C
Cephalexin + A22 treatment (short cell)
2.6 µm²
3.0 µm²
3.9 µm²
6.0 µm²
D
Cephalexin + A22 treatment (long cell)
4.2 µm²
5.9 µm²
7.8 µm²
9.6 µm²
11.2 µm²
14.5 µm²
E
9.0 µm²
F
RplA-GFP
HupA-mCherry
Number of segmented fluorescent objects per cell
Normalized average area of segmented fluorescent objects per cell
Cephalexin
Cephalexin + A22

Figure 7

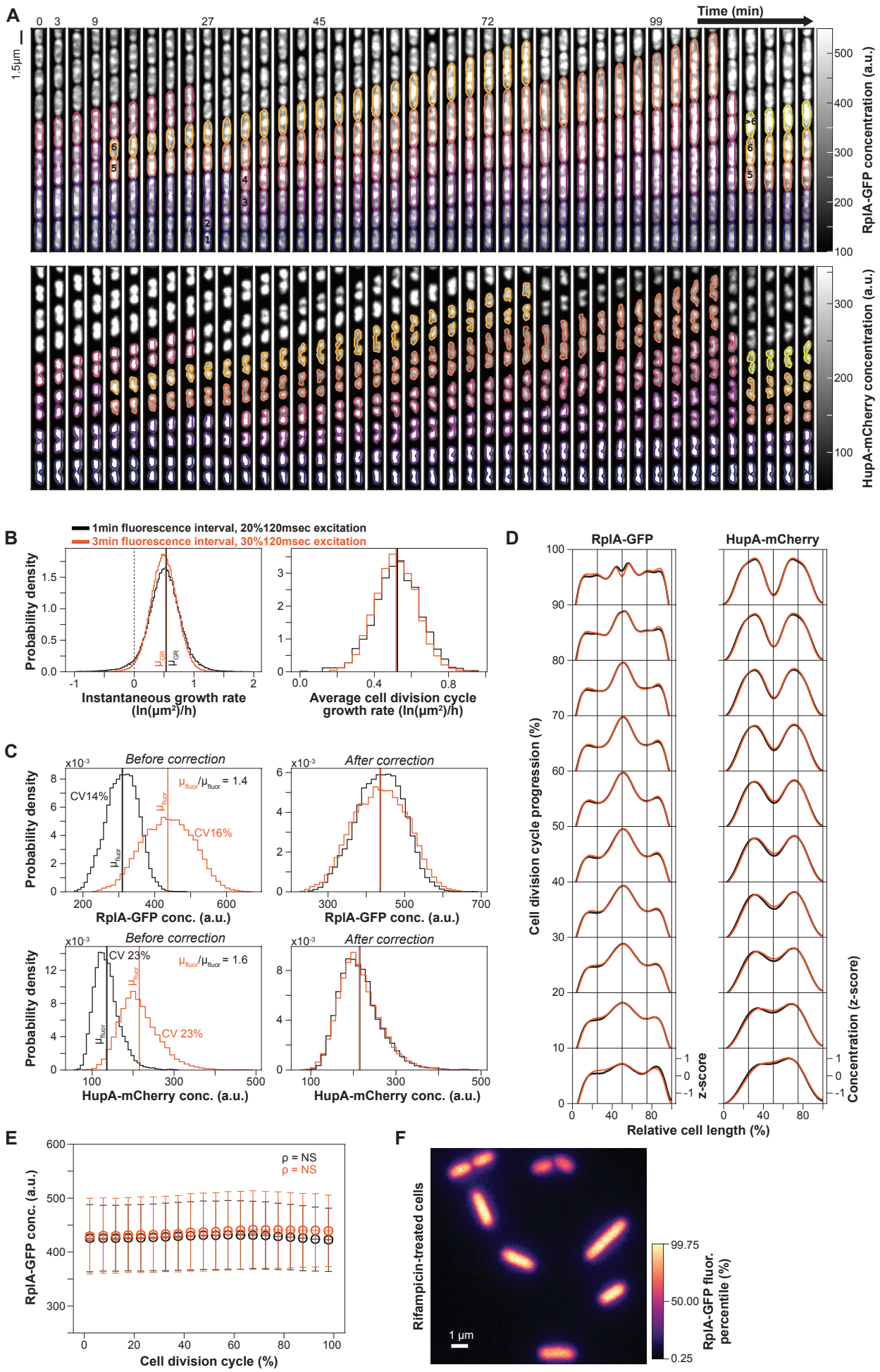

Figure 1 - figure supplement 1

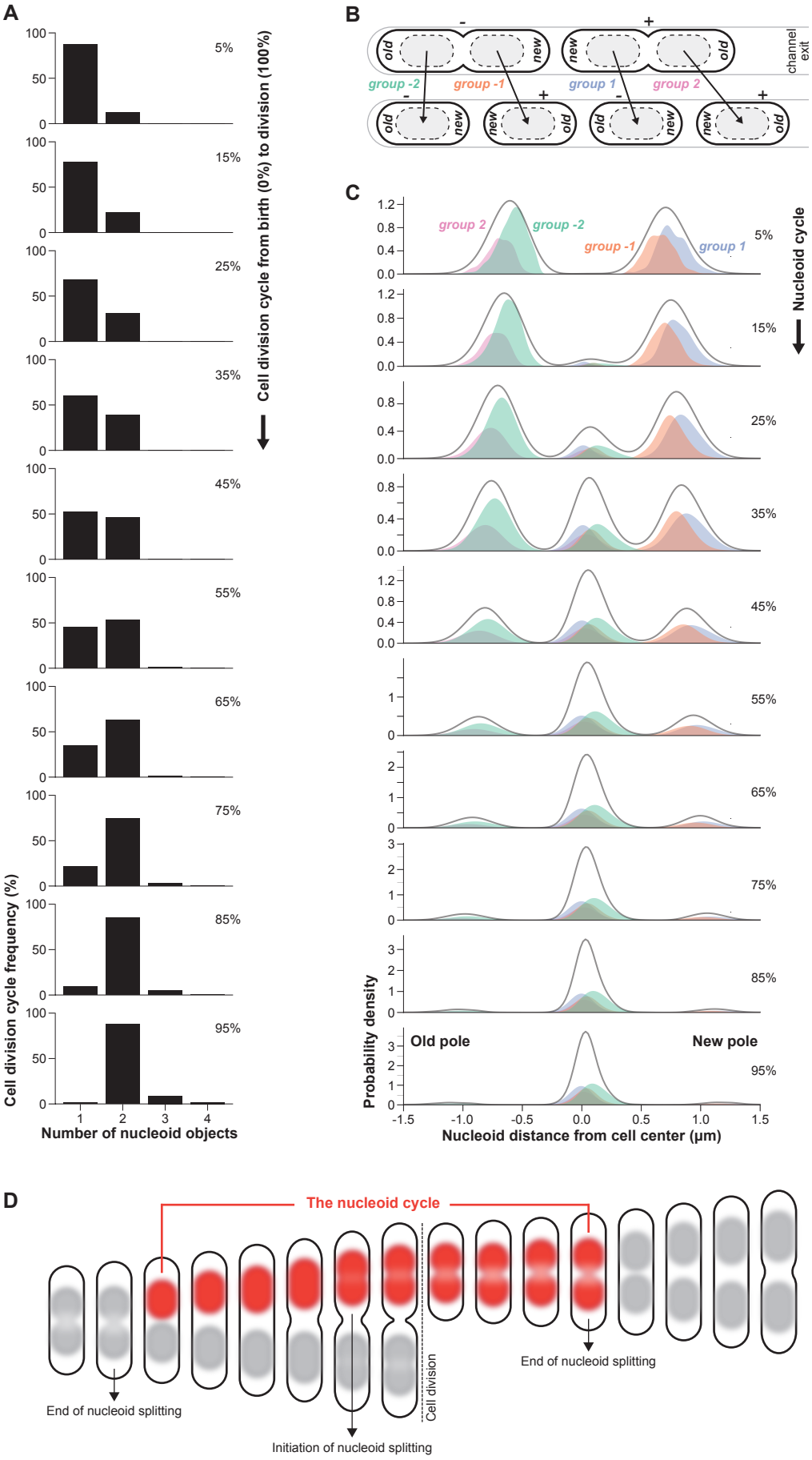

Figure 1 - figure supplement 2

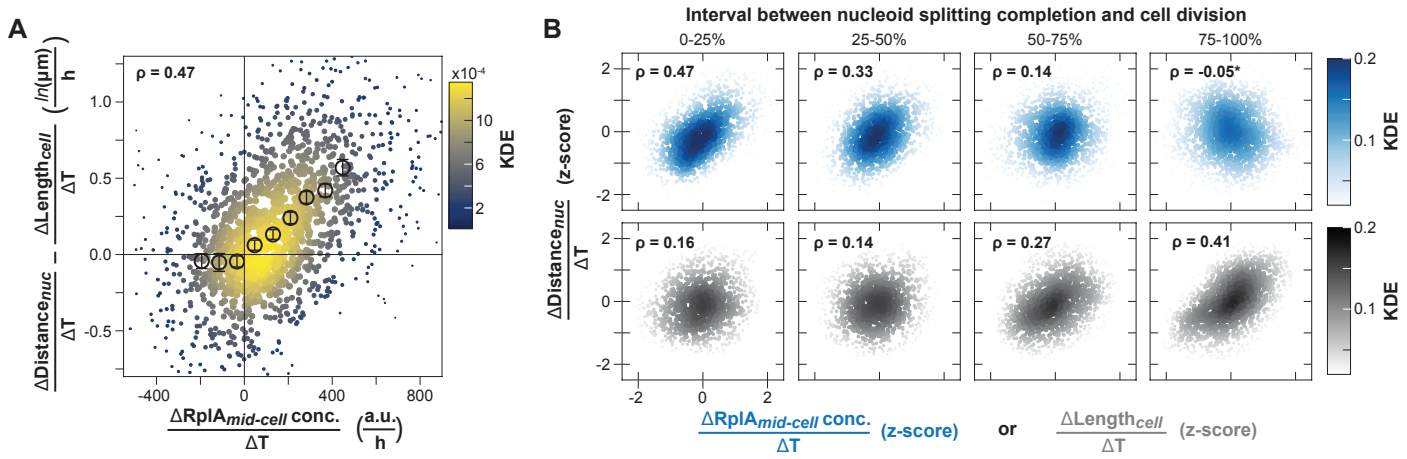

Figure 1 - figure supplement 3

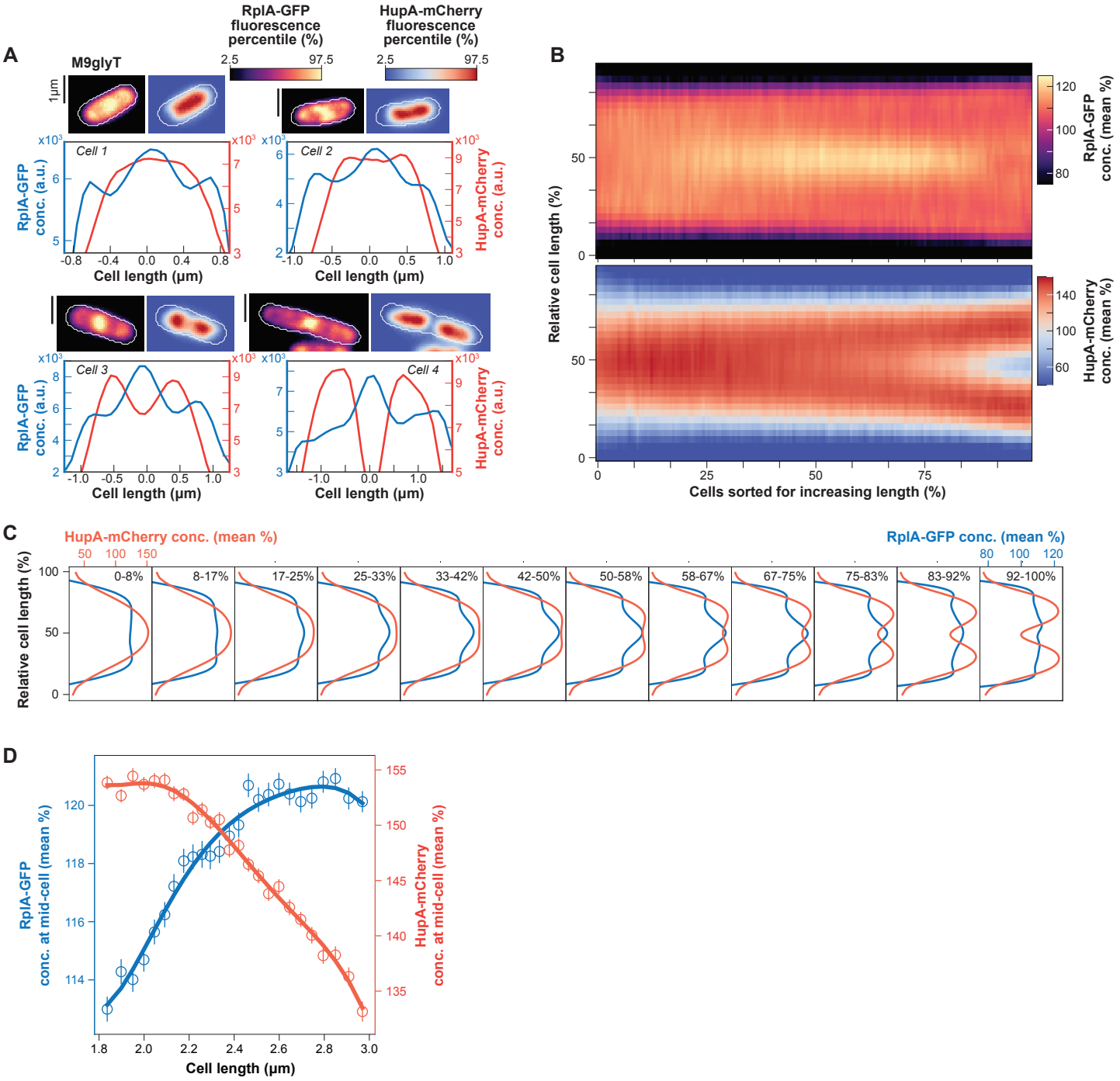

Figure 1 - figure supplement 4

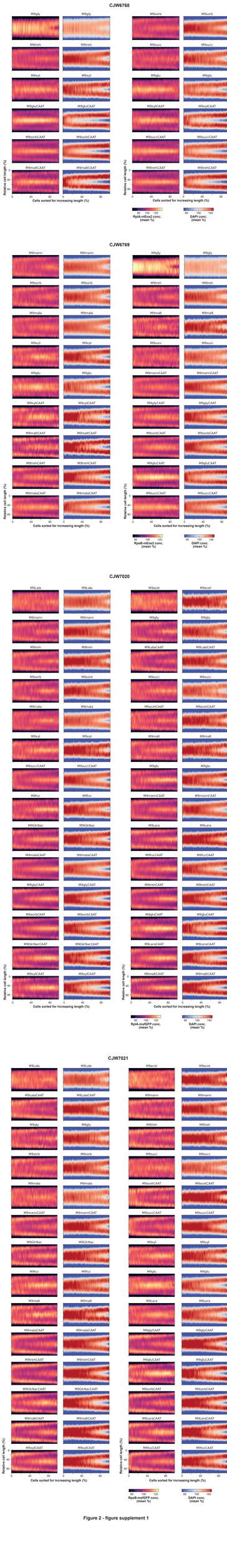

Figure 2 - figure supplement 1

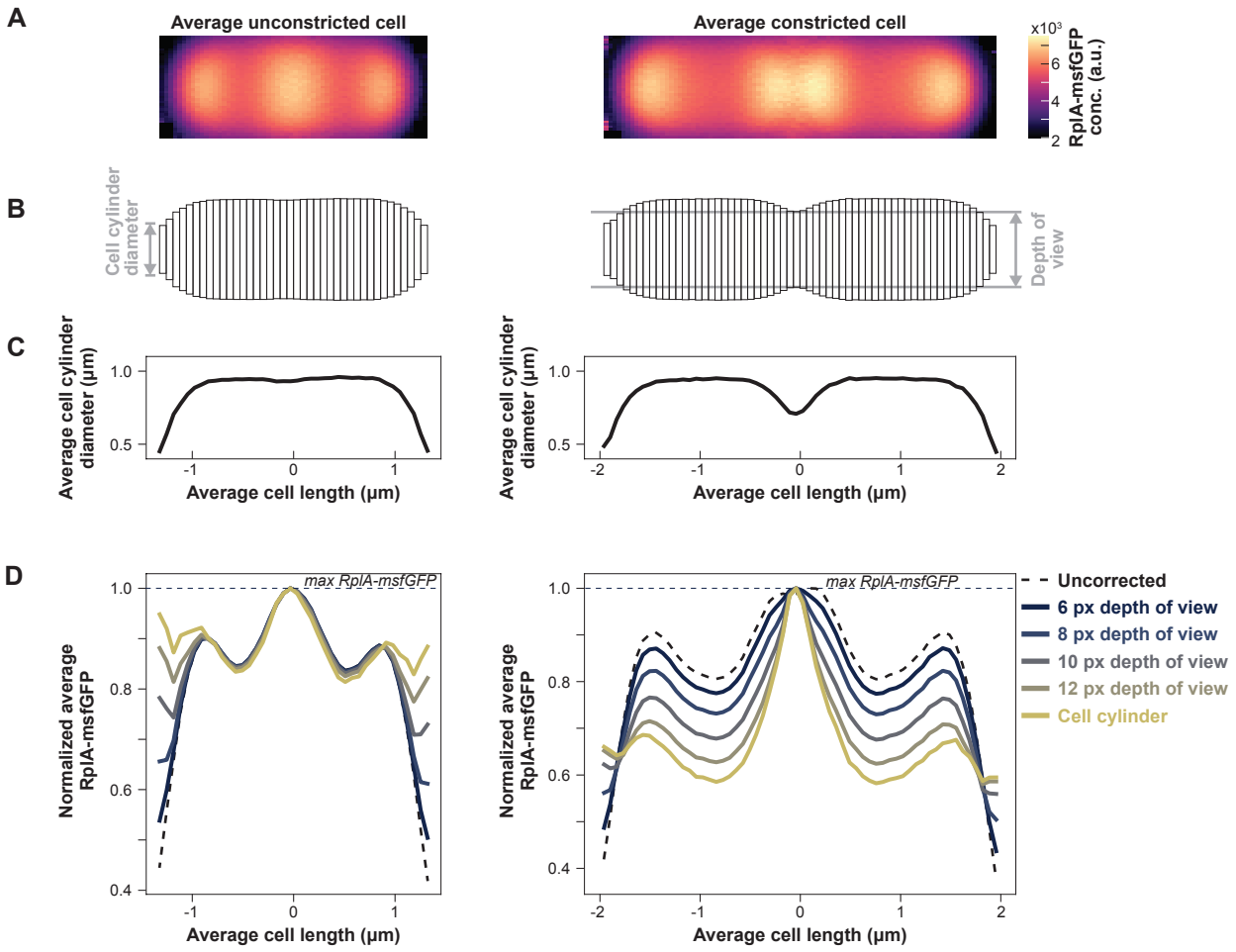

Figure 2 - figure supplement 2

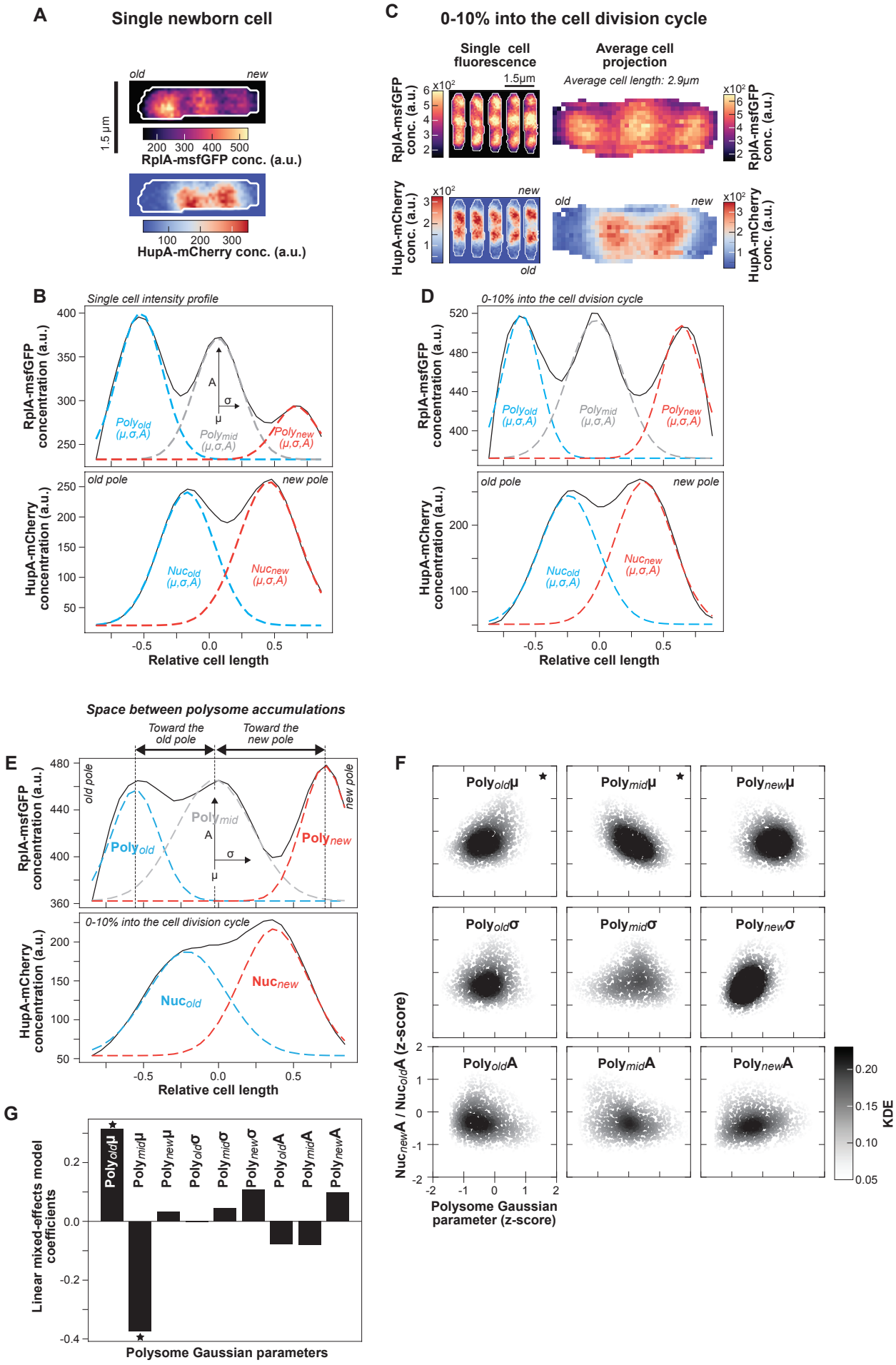

Figure 3 - figure supplement 1

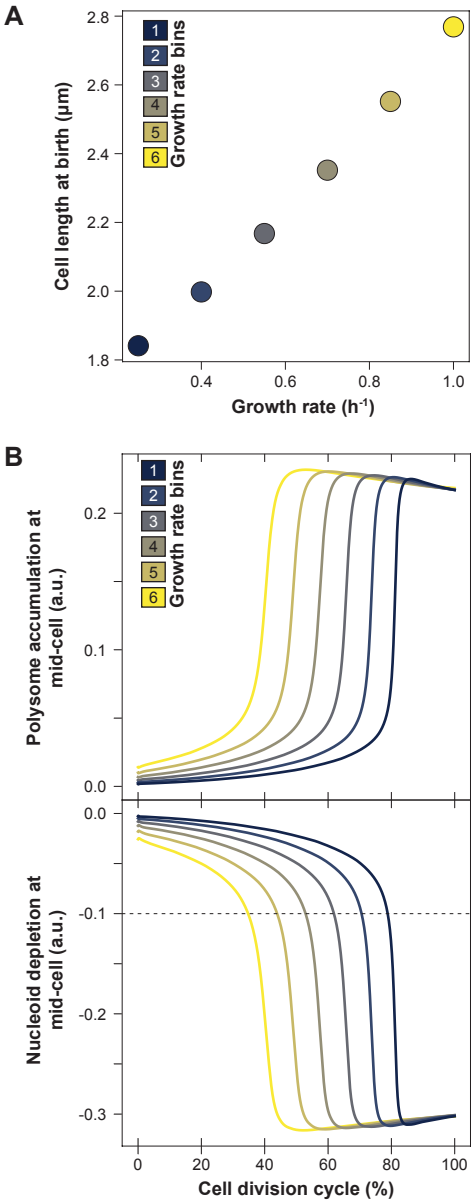

Figure 4 - figure supplement 1

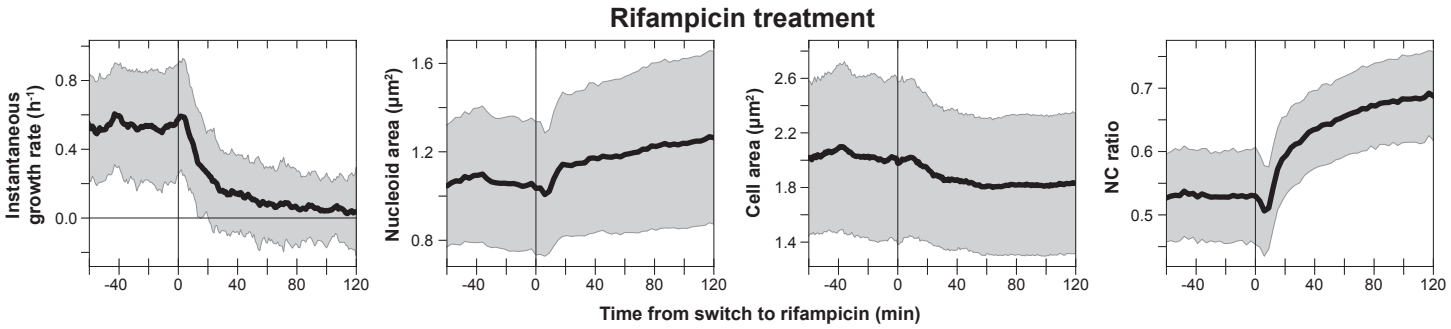

Figure 5 - figure supplement 1

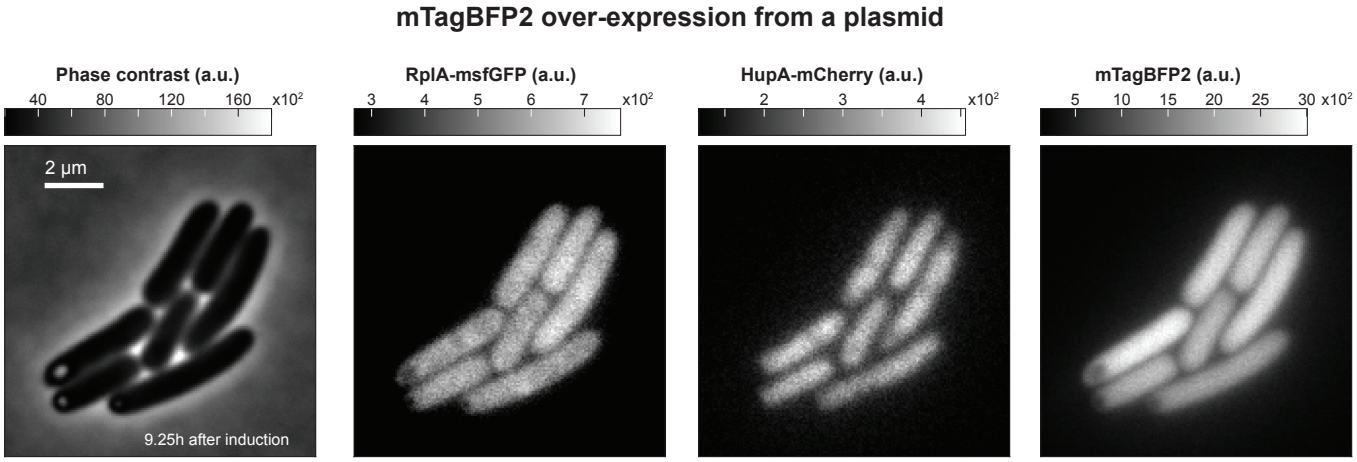

Figure 6 - figure supplement 1

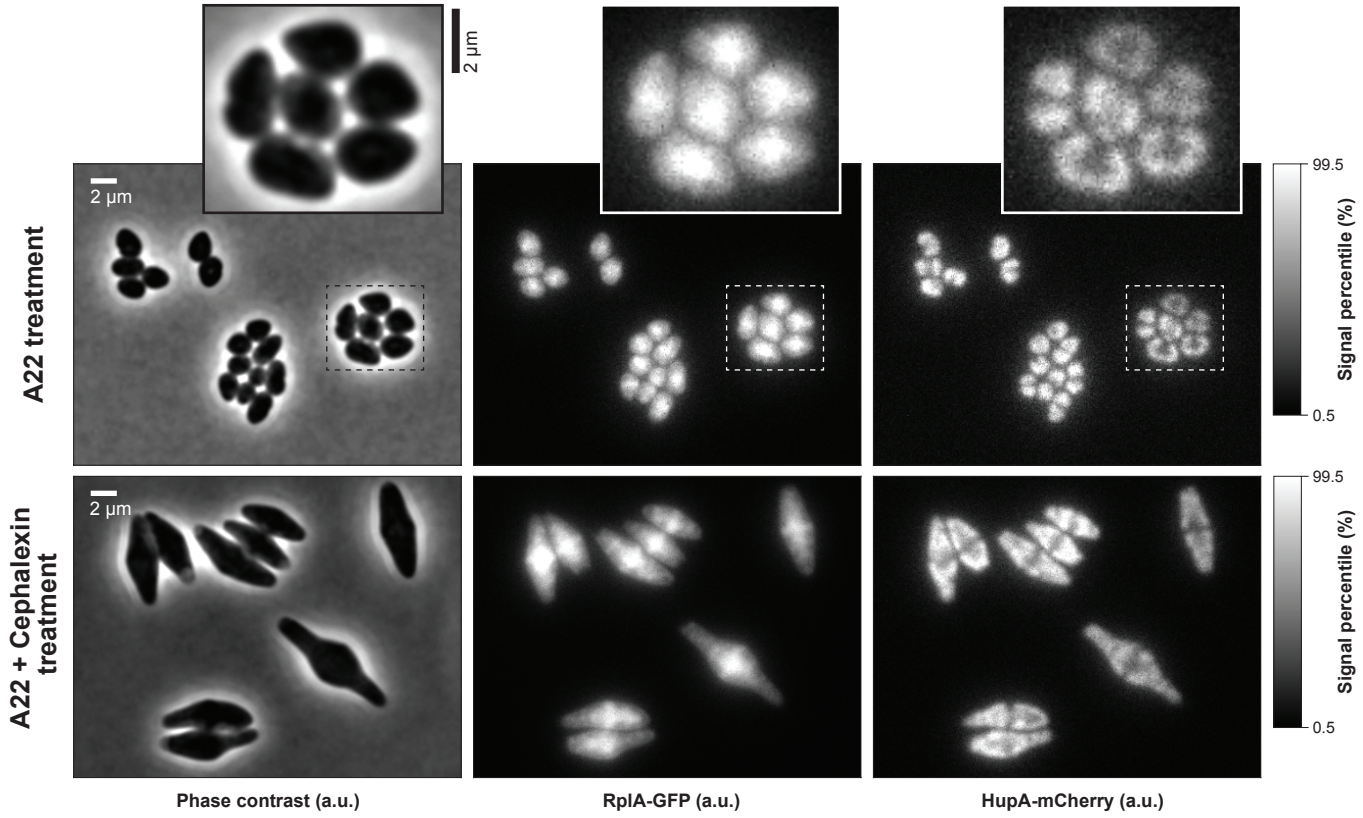

Figure 7 - figure supplement 1